arXiv:2606.27615v1 [physics.flu-dyn] 26 Jun 2026

INTERFACE TRACKING WITH MICROSCALE TOPOLOGICAL SURGERY FOR TWO-DIMENSIONAL FILAMENT BREAKUP

RAAGHAV RAMANI

Abstract. We design and implement a *Microscale Topological Surgery* (MTS) algorithm to detect and enforce topological transitions in two-dimensional tracked interfaces. The method combines classical Lagrangian tracking with an intermittent topological processor that: (*i*) constructs Eulerian snapshots from which an interface family with microscale-resolved topology is extracted, (*ii*) infers adjacency topology between dual Lagrangian and Eulerian interface families, and (*iii*) performs interface surgery to stitch the two families together across microscale defect regions. A novel long-time nonlinear alternating-shear flow is introduced, in which repeated stretching and folding generate rich multiscale interface dynamics with filamentation at microscales. Using the MTS algorithm and *a posteriori* geometric and material diagnostics, we compute and visualize microscale filament-breakup dynamics. Error analysis and scaling studies demonstrate second-order geometric convergence and optimal computational scaling of the MTS algorithm, with topology-processing costs comparable to those of the underlying Lagrangian evolution. Ensemble simulations generated by pseudo-random perturbations of the flow further reveal coherent droplet size distributions and statistically robust filament-breakup dynamics.

Contents

1. Introduction

We consider the evolution of a collection of two-dimensional *interfaces* $\Gamma_\alpha(t)$ under the flow of a given smooth velocity field $u(x,t)$. Our primary interest is in multiscale interface dynamics characterized by large-scale deformations at length scale $L>0$ together with fine-scale structure at length scale $h>0$, satisfying

$$0<\frac{h}{L}\ll 1. \tag{1.1}$$

Such scale separation commonly arises through *filamentation*, whereby stretching and folding of the interface generate progressively thinner interfacial structures while simultaneously maintaining large-scale geometric features. In the specific case that

$$\frac{h}{L}=\mathcal{O}(10^{-3}),$$

we refer to h as a *microscale-resolving* length scale. Numerical approaches for computing the interfacial evolution can be broadly categorized into interface *capturing* and interface *tracking* methods.

Eulerian interface-capturing methods represent the evolving interface implicitly through one or more auxiliary fields defined on a fixed computational mesh. Prominent examples include level-set (LS) methods [38, 40, 37, 12], volume-of-fluid (VOF) methods [29, 46], and moment-of-fluid (MOF) methods [15, 59, 1, 30,

25, 26]. In these approaches, topological transitions are accommodated through a finite-scale *geometric regularization* associated with the implicit interface representation. An alternative class of methods replaces the sharp interface by a diffuse transition layer governed by an auxiliary order parameter, thereby introducing a *physical regularization* of topological singularities through interfacial mixing and diffusion [33, 34]. Both approaches naturally accommodate topological transitions without requiring specialized reconstruction procedures, and their robustness and flexibility have made them standard tools in multiphase-flow simulations. The tradeoff is that the interface is transported indirectly through advection on the background computational mesh, causing numerical errors to accumulate over time. As a result, resolving fine-scale filamentary structures typically requires substantial volumetric mesh refinement, thereby increasing the number of spatial degrees of freedom and imposing more restrictive CFL stability constraints, both of which contribute to the overall computational cost.

Lagrangian interface-tracking methods, by contrast, represent the interface explicitly by parametrized codimension–1 hypersurfaces moving with the flow [8, 56, 43], thereby providing sharp interface descriptions and direct access to geometric quantities such as normals, curvature, and surface differential operators. Moreover, adaptive refinement may be concentrated directly on the interface, making Lagrangian approaches particularly efficient for problems involving highly localized interfacial structure and large scale separations. For example, in the rotating-vortex benchmark considered below, we show that Lagrangian tracking is approximately 1000 times more accurate than a baseline Eulerian capturing method, while running 100 times faster (Figure 7). The principal limitation of Lagrangian tracking methods is the topological rigidity of the underlying interface representation. Because interface connectivity is built directly into the underlying curve or mesh data structures, the classical Lagrangian evolution alone cannot alter the topology of the interface. Consequently, topological transitions such as pinch-off, breakup, and coalescence require specialized detection and reconstruction procedures.

1.1. **The core MTS methodology.** The contrasting characteristics of Lagrangian interface-tracking and Eulerian interface-capturing naturally motivate hybrid approaches that seek to combine the geometric accuracy and computational efficiency of the former with the topological flexibility of the latter. Motivated by the sharp-interface continuation perspective advocated by Lowengrub and Truskinovsky [33][1], we propose a hybrid Eulerian–Lagrangian *Microscale Topological Surgery* (MTS) algorithm. In our numerical framework, the sharp interface model is realized by classical Lagrangian tracking, while transitions through topology changes are handled by intermittent MTS processing. The basic computational pipeline is:

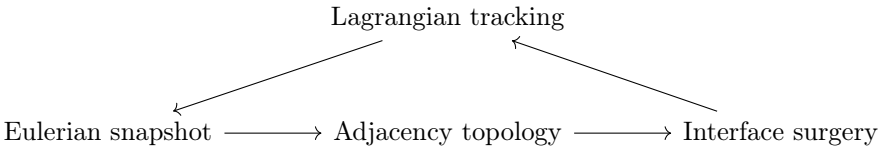

(MTS)

The lower row of the diagram represents the core MTS procedure. Throughout the paper, we will use the terminology MTS interchangeably for both this core procedure and the complete hybrid tracking algorithm obtained by coupling with the underlying Lagrangian evolution.

An overview of the MTS algorithm is provided in the flowchart in Figure 1 and summarized in the following. The proposed method evolves the interface family $\{\Gamma_\alpha(t)\}$ over the time interval $[0, t_{\mathsf{max}}]$, discretized uniformly with time-step Δt,

$$t_k = k\Delta t, \qquad k = 0, \dots, K, \qquad K\Delta t = t_{\mathsf{max}}. \tag{1.2a}$$

We prescribe a sequence of MTS times

$$\{T_m\}_{m=1}^{M} \subset \{t_k\}_{k=0}^{K}, \qquad 0 < T_1 < T_2 < \cdots < T_M \le t_{\mathsf{max}}, \tag{1.2b}$$

and evolve the interfaces by a classical Lagrangian tracking method for $t \in (T_m, T_{m+1})$. Meanwhile, at each time $t = T_m$, we process the interface family by the MTS algorithm to detect and enforce topological changes. The MTS algorithm evolves the interface geometry consistently down to the prescribed fine scale h, while permitting topological transitions below this threshold. In particular, filamentary structures with thickness comparable to or smaller than h are regarded as topologically unresolved and are subsequently

[1] Lowengrub and Truskinovsky [33] argued that *"...it is natural to conclude that the ideal numerical approach should be based on the sharp interface model and then use 'jump conditions' to transit the sharp interface through a topology change."*

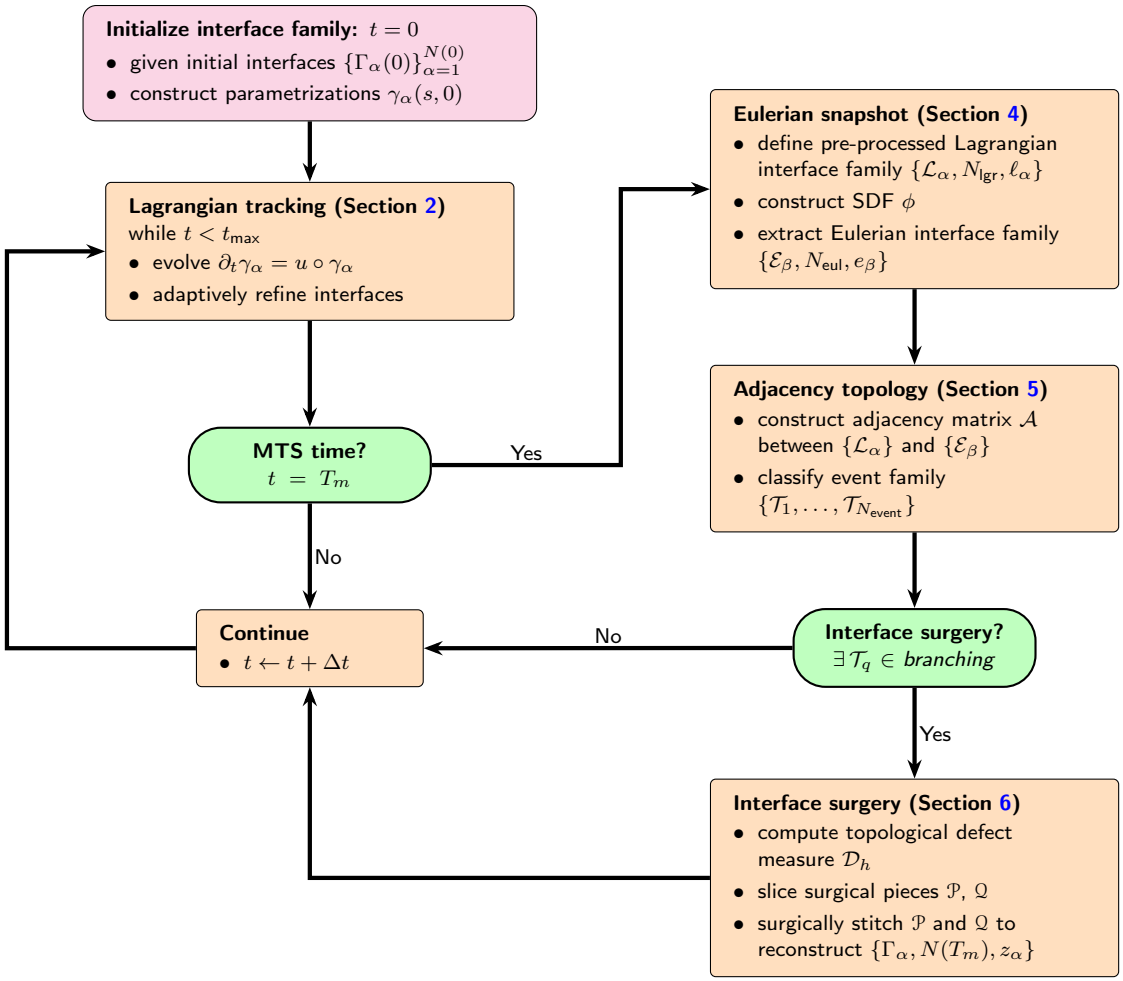

FIGURE 1. Flowchart of the Lagrangian tracking algorithm with Microscale Topological Surgery (MTS).

TABLE 1. Summary of principal notation, terminology, and parameters.

Category	Symbol	Description
Temporal parameters	$t_{\max}$, Δt, $\{t_k\}$	final time, time-step size, and computational times (1.2a)
	$\{T_m\}$	MTS times (1.2b)
Spatial parameters	h_0, h	coarse and fine mesh spacings (4.4)
	L, h/L	large-scale deformation length and scale-separation ratio (1.1)
Fidelity & smoothing parameters	$d_{\text{ref}} = \frac{h}{2}$, $d_{\text{crs}} = \frac{h}{10}$	default refinement and coarsening thresholds
	$N_{\min} = 3$, $L_{\min} = \frac{h}{10}$, $A_{\min} = \frac{h^2}{10}$	default sub-microscale filtering thresholds
	$w_{\text{fit}} = 10^{-5}$, $w_{\text{sm}} = h^2$, $w_{\tan} = 1$	default interface surgery smoothing parameters
Lagrangian tracking	$\Gamma_\alpha(t)$, $N(t)$	evolving interfaces and interface count
	$\gamma_\alpha(s,t)$	interface parametrization
	$\tau_\alpha(s,t)$, $\nu_\alpha(s,t)$, $\kappa_\alpha(s,t)$	tangent, normal, and curvature
	$\xi_\alpha(s,t)$, $\lambda_\alpha^{\tan}(s,t)$, $\sigma_\alpha^{\tan}(s,t)$	(unnormalized) tangent field, stretch factor, and FTLE
	$\mathcal{W}_j(t)$, $c_j(t)$, $w_j(t)$	Lagrangian observation window, center, and half-width
	$\Gamma_{\alpha,h}(t)$, $S_{\alpha,j}$, N_α	polygonal approximation, segment, and node count
MTS variables	$\mathcal{L}_\alpha$, N_{lgr}, ℓ_α	pre-processed Lagrangian interface family
	$\mathcal{E}_\beta$, N_{eul}, e_β	extracted Eulerian interface family
	ϕ	signed-distance function
	$\mathcal{A}$, $\{\mathcal{T}_q\}$, N_{event}	adjacency matrix, local events, and number of events
	(μ, η), $\mathcal{D}_h$	topological defect densities and regularized defect measure
	$\mathcal{S}$, $\{\mathcal{P}, \mathcal{Q}\}$	surgical region and surgical pieces

reconstructed by the MTS algorithm. Because this topological reconstruction is decoupled from the underlying Lagrangian geometric representation, MTS continues to track sub-microscale filamentary geometry even after the topology has been modified at scale h.

Several existing methods combine Eulerian and Lagrangian information in hybrid interface representations. Marker-particle level-set and VOF methods, for example, augment Eulerian interface-capturing schemes with Lagrangian information to improve accuracy [16, 2]. The MTS methodology instead begins from an explicitly tracked *pre-processed* Lagrangian interface family $\{\mathcal{L}_\alpha\}$ and uses *Eulerian snapshots* to supply topological information. Within the Eulerian-snapshot framework, a common strategy is to detect topological changes through intersections between the tracked Lagrangian interface and an underlying Eulerian grid [19, 14, 5, 50].[2] Rather than relying on grid-intersection tests, MTS constructs an auxiliary Eulerian field whose extracted zero level set serves as a topological "oracle", providing the topological source of truth used to identify and enforce interface transitions.

Specifically, our MTS algorithm constructs a signed-distance function (SDF) ϕ from the pre-processed Lagrangian interface family using an efficient bounding-box accelerated closest-point algorithm together with a ray-casting procedure for sign determination. The zero-level set of ϕ defines the topological oracle, from which a topologically corrected Eulerian interface family $\{\mathcal{E}_\beta\}$ is extracted using a standard marching-squares procedure [32]. In this sense, MTS may be viewed as a realization of the basic sharp-interface continuation philosophy advocated by Lowengrub and Truskinovsky [33]; an essential distinction is that topological transitions are resolved here through a purely *geometric* construction, rather than through the *diffuse-interface* dynamics described in [33]. For related approaches based on reconstructed Eulerian interfaces we refer the reader to [48, 6, 52, 49, 58, 35, 7, 18].

Using the interface families $\{\mathcal{L}_\alpha\}$ and $\{\mathcal{E}_\beta\}$ as input, the second stage of the MTS algorithm infers the *adjacency topology* between the two families from their local geometric configuration. The adjacency topology provides a parent–child correspondence structure between the two interface families, with topological transitions manifested through departures from one-to-one correspondence. Such correspondence structures underlie existing topological reconstruction algorithms [19, 14, 5, 18]; in MTS, they are made explicit through a graph-theoretic construction. Specifically, we represent the adjacency topology by a bipartite graph and use its connected components to decompose the topology into independent local topological events, which are subsequently classified according to their parent–child connectivity as *trivial*, *vanishing*, or *branching*.

The first two event types may be resolved directly, whereas *branching* events require *interface surgery*, performed in the third stage of the MTS pipeline. Existing approaches have either employed direct-replacement strategies, in which the Lagrangian interfaces are globally replaced by topologically corrected Eulerian interfaces [48, 52, 35, 50, 39, 18], or surgical reconstructions based on grid-intersection tests [19, 14, 58, 5, 23]. In the MTS methodology, we employ a surgical framework based on the construction of localized surgical regions identified through a collection of topological *defect densities* and associated *defect measures*. Topologically inconsistent portions of the dual interface families are identified through degeneracies in their closest-point correspondences, and the resulting defect densities (μ, η) provide a localization of the underlying topological inconsistencies. A related approach is employed in the "kink-detection" algorithm proposed in [24] for level-set reinitialization specialized to filamentary flows. See also the recently proposed signature method underlying the "manifold-death" algorithm of [9], which likewise targets filamentation.

An h-scale regularized defect measure $\mathcal{D}_h$ is then constructed from the defect densities, thereby providing an Eulerian representation of the microscale defect regions. The associated surgical regions $\mathcal{S}$ are subsequently used to decompose the Lagrangian and Eulerian interface families into compatible surgical pieces $\{\mathcal{P}, \mathcal{Q}\}$, which are stitched together through a graph-theoretic cycle-tracing procedure to produce the post-transition interface family.

The principal application considered in this work is multiscale interface evolution driven by filamentation. To assess the performance of the MTS methodology in this setting, three numerical examples of increasing complexity are considered. The first is the classical rotating-vortex flow [46], which serves as a standard benchmark for interface-capturing and interface-tracking methods. Using the MTS algorithm, we simulate the formation and subsequent disappearance of satellite interfaces generated during the filamentation process. This behavior is consistent with the qualitative dynamics observed in interface-capturing simulations. The second example is the $\mathcal{S}$-flow benchmark, developed in the context of filament-aware MOF methods

[2] Topological transitions may also be handled without constructing an Eulerian snapshot [36, 19, 55, 45]. Such approaches operate directly on the Lagrangian representation and do not employ an independent Eulerian topology oracle.

[1, 30, 25, 26]. Compared with the rotating-vortex flow, this second benchmark exhibits a moderately more intricate multiscale structure. The corresponding MTS solutions qualitatively reproduce the resulting filament-breakup dynamics.

The third numerical example is a new filamentation benchmark based on a continuous-in-time embedding of a nonlinear alternating-shear map. The repeated stretching-and-folding of the interface produces substantially richer multiscale structure than either of the two previous benchmarks, along with a sustained sequence of topological transitions. To analyze these dynamics, we employ a tangent modification [54] of the classical finite-time Lyapunov exponent (FTLE) [22, 47, 21], which provides a quantitative diagnostic of filament formation along the evolving interface. We then use the tangent FTLE as an *a posteriori* diagnostic tool to visualize complex filament-breakup processes at microscale resolution. Using the analytical structure of the proposed benchmarks, we perform a quantitative analysis demonstrating $\mathcal{O}(h^2)$ convergence of geometric errors competitive with existing filament-aware MOF schemes [30, 25]. Moreover, we show that the computational cost of the MTS pipeline remains commensurate with the baseline cost of Lagrangian tracking, so that the combined algorithm exhibits optimal $\mathcal{O}(h^{-2})$ computational scaling. Finally, we exploit the computational efficiency of the MTS framework to construct ensembles of microscale-resolving simulations, revealing a competition between filament-breakup dynamics and statistical coarse-graining: most breakup events are absorbed into a diffuse-interface description, while the breakup in the strongest filamenting region survives coarse-graining and is statistically persistent.

Outline of the paper. The remainder of the paper is organized as follows. In Section 2, we review the classical Lagrangian interface-tracking framework and introduce the tangent-FTLE diagnostic used in the subsequent numerical examples. In Section 3, we introduce two of the benchmark problems and establish baseline results using the classical Lagrangian tracking algorithm. The three core stages of the MTS methodology are then developed in Sections 4 to 6, where we introduce the Eulerian snapshot construction, the adjacency topology framework, and the interface surgery algorithm. Numerical results are presented in Section 7, followed by concluding remarks in Section 8. Detailed descriptions of the supporting algorithms for the MTS processor are provided in Section A.

2. Classical Lagrangian interface tracking

This section reviews the classical Lagrangian interface-tracking formulation adopted in the present work. The goal is to establish notation, define the governing evolution equations, and provide a reference implementation for the subsequent MTS reconstruction framework. In addition, we introduce a tangential finite-time Lyapunov exponent (FTLE) diagnostic for characterizing the formation and development of filamentary structures along evolving interfaces.

2.1. Lagrangian formulation of the interface evolution problem.

A schematic of the interface tracking problem is shown in Figure 2. We consider the evolution of a family of bounded, simply connected domains

$$\Omega_\alpha(t) \subset \mathbb{R}^2, \qquad t \in [0, t_{\mathsf{max}}], \tag{2.1a}$$

where the subscript α indexes the family. The boundary of each domain is denoted by

$$\Gamma_\alpha(t) \coloneqq \partial\Omega_\alpha(t), \tag{2.1b}$$

and is referred to as an *interface*. Each interface is assumed to be a smooth, simple, closed, oriented curve, and we assume that the interfaces remain mutually non-intersecting throughout the evolution so that $\Gamma_\alpha(t) \cap \Gamma_\beta(t) = \varnothing$ for $\alpha \neq \beta$.

As outlined in the flowchart in Figure 1, the collection $\{\Gamma_\alpha(t)\}$ is evolved primarily using a classical Lagrangian interface-tracking method, with topological changes enforced by the MTS algorithm at the prescribed set of MTS times (1.2b). The Lagrangian representation consists of an explicit time-dependent parametrization of each interface

$$\gamma_\alpha(s,t) = \left(\gamma_\alpha^1(s,t), \gamma_\alpha^2(s,t)\right), \qquad (s,t) \in \mathbb{T} \times [0, t_{\mathsf{max}}], \tag{2.2a}$$

where s denotes the parameter along the interface and $\mathbb{T} = \mathbb{R}/2\pi\mathbb{Z}$ denotes the one-dimensional periodic torus, identified with the interval $[0, 2\pi]$ equipped with periodic boundary conditions. Each interface is therefore represented by

$$\Gamma_\alpha(t) = \{\gamma_\alpha(s,t) : s \in \mathbb{T}\}. \tag{2.2b}$$

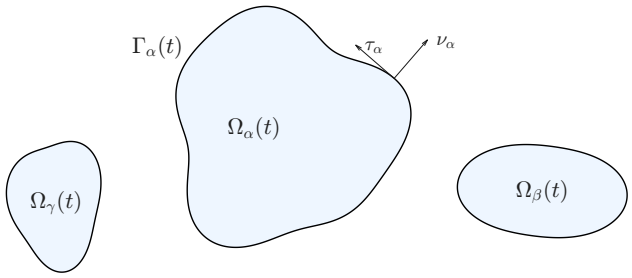

FIGURE 2. Schematic of the interface evolution problem.

The unit tangent and normal vectors to each interface $\Gamma_\alpha(t)$ are given by

$$\tau_\alpha(s,t) = \frac{\partial_s \gamma_\alpha(s,t)}{|\partial_s \gamma_\alpha(s,t)|} \qquad \text{and} \qquad \nu_\alpha(s,t) = \tau_\alpha^\perp(s,t), \tag{2.3a}$$

where $(a,b)^\perp = (-b,a)$, and the curvature of the interface is given by

$$\kappa_\alpha(s,t) = \frac{|\partial_s \tau_\alpha \cdot \nu_\alpha|}{|\partial_s \gamma_\alpha|} = \frac{\left|\partial_s \gamma_\alpha^1 \, \partial_s^2 \gamma_\alpha^2 - \partial_s \gamma_\alpha^2 \, \partial_s^2 \gamma_\alpha^1\right|}{|\partial_s \gamma_\alpha|^3}. \tag{2.3b}$$

The interface index α ranges over

$$\alpha = 1, \dots, N, \tag{2.4a}$$

where N is a non-negative integer. In the classical Lagrangian interface-tracking method [8], N is a constant fixed by its value at the initial time. In the proposed MTS method, interfaces are allowed to undergo topological transitions, so that $N(t)$ becomes a time-dependent non-negative integer-valued function

$$N : [0, t_{\mathsf{max}}] \to \mathbb{N}. \tag{2.4b}$$

In particular, $N(t)$ remains constant on each time interval $t \in [T_m, T_{m+1})$, with changes permitted only at the MTS times $t = T_m$.

For times $t \in (T_m, T_{m+1})$, the interface parametrizations γ_α are evolved by solving the Lagrangian evolution equations

$$\partial_t \gamma_\alpha(s,t) = u(\gamma_\alpha(s,t),t), \qquad (s,t) \in \mathbb{T} \times (T_m, T_{m+1}), \quad \alpha = 1, \dots, N(T_m), \tag{2.5a}$$

with initial data

$$\gamma_\alpha(s, T_m) \quad \text{generated by the MTS algorithm applied at time } t = T_m. \tag{2.5b}$$

The *classical Lagrangian tracking* algorithm is recovered by bypassing the MTS reconstruction step in (2.5b) and simply taking the initial data at each time T_m to be the terminal interface configuration obtained from the preceding Lagrangian evolution.

We assume that the velocity field

$$u : \mathbb{R}^2 \times [0, t_{\mathsf{max}}] \to \mathbb{R}^2$$

is smooth. The proposed framework does not depend on how $u(x,t)$ is obtained; for instance, it may be prescribed analytically, computed by a coarse-scale fluid solver, or generated by a boundary integral method.

2.2. **Polygonal interface representation with adaptive refinement.** The Lagrangian evolution equations (2.5) are discretized in time using the standard TVD-RK3 scheme [51] with fixed time step Δt. In the following, we describe the spatial discretization scheme employed, including the adaptive refinement procedure used to maintain geometric resolution throughout the evolution. Adaptive refinement techniques for Lagrangian interface tracking are well established in the literature, including three-dimensional implementations [56, 19, 55, 14, 5, 20, 45].

We use Greek subscripts $\alpha, \beta, \dots$ to index the interface family and Roman subscripts $i, j, \dots$ to index the spatial discretization along each interface. At each time t, we denote by

$$s_{\alpha,i}(t) \in \mathbb{T}, \qquad i = 1, \dots, N_\alpha(t), \qquad \alpha = 1, \dots, N(t), \tag{2.6a}$$

a family of discretizations of the the parameter interval $\mathbb{T}$. Here $N_\alpha : [0, t_{\mathsf{max}}] \to \mathbb{N}$ denotes the number of *nodes* in the corresponding discretization, which is allowed to vary in time under adaptive refinement

and coarsening. We will often suppress the explicit dependence on time, writing $N_\alpha \equiv N_\alpha(t)$ with the understanding that N_α will typically change at the discrete times $t = t_k$.

The spatial approximation to the interface parametrization is denoted by

$$\gamma_{\alpha,i}(t) \coloneqq \gamma_\alpha(s_{\alpha,i}(t), t), \tag{2.6b}$$

with periodic closure enforced by identifying

$$\gamma_{\alpha,N_\alpha+1}(t) = \gamma_{\alpha,1}(t). \tag{2.6c}$$

Each set of points $\{\gamma_{\alpha,i}\}_{i=1}^{N_\alpha}$ defines a polygonal approximation of the interface,

$$\Gamma_{\alpha,h}(t) = \bigcup_{i=1}^{N_\alpha} S_{\alpha,i}(t), \qquad S_{\alpha,i}(t) \coloneqq [\gamma_{\alpha,i}(t), \gamma_{\alpha,i+1}(t)], \tag{2.6d}$$

where $S_{\alpha,i}(t)$ denotes the oriented line segment connecting consecutive interface nodes.

The subscript h in $\Gamma_{\alpha,h}$ indicates that the resolution of the polygonal approximation is controlled by the fine-scale h. At this stage, h may be viewed as prescribed; later, we will define h as a dyadic refinement of a coarse computational scale h_0. As small scales develop in the evolving interface, a simple refinement algorithm is employed to maintain resolution. We introduce refinement and coarsening thresholds

$$0 \le d_{\mathsf{crs}} < d_{\mathsf{ref}} < h,$$

which determine the admissible range of segment lengths in the polygonal approximation. Segments with length exceeding d_{ref} are refined through midpoint insertion and cubic interpolation, while segments with length below d_{crs} are coarsened through node removal, producing a dyadic refinement of the parameter space $\mathbb{T}$. The resulting interface discretization is necessarily subgrid to the fine-scale h. The complete adaptive refinement procedure is described in Algorithm 1 in Section A.

2.3. **Characterizing filament formation by the tangent FTLE.** For visualization and qualitative analysis, it is useful to have a diagnostic that identifies the development of localized small scales and filamentary structures along the evolving interface. A common choice is the interface curvature; however, as the following examples illustrate, large curvature does not necessarily imply filament formation, while strongly filamentary structures may exhibit only modest curvature.

Example 2.1 (A shrinking circle)**.** *Consider an exponentially shrinking circle* $\gamma(s,t) = R_0 e^{-\lambda t}(\cos s, \sin s)^\top$, $s \in \mathbb{T}$, *with* $R_0 > 0$ *and* $\lambda > 0$. *The curvature is* $\kappa(s,t) = R_0^{-1} e^{\lambda t}$, *which becomes arbitrarily large as* $t \to \infty$. *Nevertheless, the interface remains perfectly circular for all time and develops no thin elongated structures.*

Example 2.2 (Localized incompressible stretching)**.** *Let* $\gamma_0(s) = (a_0 \cos s, b_0 \sin s)^\top$, $s \in \mathbb{T}$, *denote an ellipse with semi-axes* $a_0 = 4$ *and* $b_0 = 0.35$. *We deform this curve by the time-dependent family of maps*

$$\psi(x_1, x_2, t) = \left(F(x_1, t),\ \frac{x_2}{\partial_1 F(x_1, t)} \right)^\top, \qquad t \in [0, 1],$$

where

$$F(x_1, t) = x_1 + \tfrac{\sqrt{\pi}}{2} A t \operatorname{erf}(x_1), \qquad \partial_1 F(x_1, t) = 1 + A t e^{-x_1^2},$$

with $A = 4$. *The deformation gradient is*

$$D\psi(x_1, x_2, t) = \begin{pmatrix} \partial_1 F(x_1,t) & 0 \\ -\frac{x_2 \partial_1^2 F(x_1,t)}{(\partial_1 F(x_1,t))^2} & \frac{1}{\partial_1 F(x_1,t)} \end{pmatrix},$$

so that $\det D\psi = 1$. *The initial and final interfaces are shown in Figure 3(a). The localized increase in* $\partial_1 F(x_1, t)$ *produces strong tangential stretching near* $x_1 = 0$ *together with transverse compression through the factor* $1/\partial_1 F(x_1, t)$, *causing the interface to develop an elongated filamentary region. Meanwhile, the curvature (shown in Figure 3(b)) remains bounded by its initial maximum value.*

To characterize the formation of filamentary structures, we introduce a Lagrangian diagnostic based on the tangential deformation of neighboring material points along the evolving interface family. Let

$$\psi : \mathbb{R}^2 \times [0, t_{\mathsf{max}}] \to \mathbb{R}^2 \tag{2.7a}$$

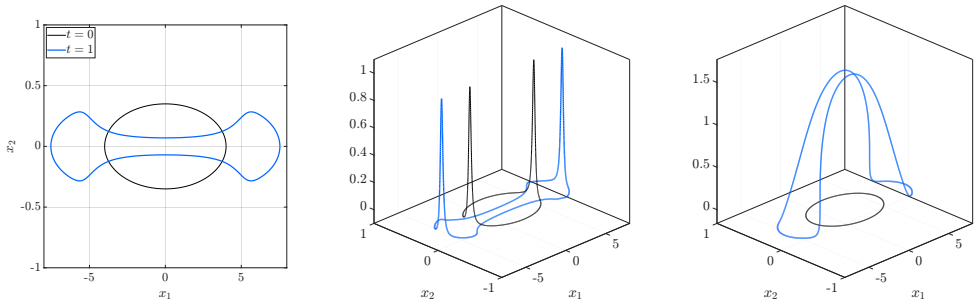

(A) Interface evolution (B) Normalized curvature (C) Tangent FTLE

FIGURE 3. Localized incompressible stretching of the ellipse from Theorem 2.2. In all panels, quantities at $t = 0$ are shown in black and quantities at $t = 1$ are shown in blue. The curvature and tangent FTLE diagnostics are plotted directly on the evolving interface. **Left:** Formation of an elongated filament in the interface $\gamma(s, 1)$. **Center:** Normalized curvature $|\kappa(s,t)|/\max_{r\in\mathbb{T}}|\kappa(r,0)|$. Despite the pronounced filamentation, the maximum curvature at the final time remains bounded by its initial maximum value. **Right:** The tangent FTLE develops a pronounced localized maximum that identifies the filamentary region.

denote the flowmap associated with the velocity field $u(x,t)$ so that

$$\gamma_\alpha(s,t) = \psi(\gamma_\alpha(s,0),t). \tag{2.7b}$$

The classical finite-time Lyapunov exponent (FTLE) measures the maximal finite-time stretching experienced by infinitesimal perturbations under the flowmap [22, 47, 21]. Introducing the Cauchy–Green strain tensor

$$C(x,t) = D\psi(x,t)^\top D\psi(x,t),$$

where $D\psi$ denotes the deformation gradient of the flowmap, the classical FTLE is defined by

$$\Lambda(x,t) \coloneqq \tfrac{1}{2t}\log\lambda_{\max}(C(x,t)) = \tfrac{1}{2t}\log\left(\max_{v\neq 0}\tfrac{v^\top C(x,t)v}{v^\top v}\right) = \tfrac{1}{t}\log\left(\max_{v\neq 0}\tfrac{|D\psi(x,t)v|}{|v|}\right),$$

where $\lambda_{\max}$ denotes the largest eigenvalue of $C(x,t)$. Thus, the classical FTLE measures the maximal finite-time stretching rate over all perturbation directions.

For interface dynamics, however, the relevant perturbations are those connecting neighboring material points on the interface. Since the stretching and compression of such perturbations govern the local concentration or separation of interface markers and thereby drive the formation of filamentary structures, we follow the viewpoint of THIFFEAULT [54] and restrict attention to perturbations in the tangent direction of the material interface. Introducing the unnormalized tangent field

$$\xi_\alpha(s,t) \coloneqq \partial_s\gamma_\alpha(s,t), \tag{2.8a}$$

differentiation of (2.7) with respect to s then yields

$$\xi_\alpha(s,t) = D\psi(\gamma_\alpha(s,0),t)\,\xi_\alpha(s,0). \tag{2.8b}$$

The tangential stretch factor

$$\lambda_\alpha^{\tan}(s,t) \coloneqq \frac{|\xi_\alpha(s,t)|}{|\xi_\alpha(s,0)|} = |D\psi(\gamma_\alpha(s,0),t)\,\tau_\alpha(s,0)| \tag{2.9a}$$

therefore measures the local tangential stretching or compression of neighboring material points along the evolving interface. The associated *tangent finite-time Lyapunov exponent* (FTLE) is defined by

$$\sigma_\alpha^{\tan}(s,t) \coloneqq \tfrac{1}{t}\log\lambda_\alpha^{\tan}(s,t). \tag{2.9b}$$

Positive values of $\sigma_\alpha^{\tan}$ correspond to tangential stretching and negative values to tangential compression. Localized extrema of $\sigma_\alpha^{\tan}$ identify regions of concentrated tangential deformation and therefore provide a useful diagnostic for the development of filamentary structures.

To compute the tangent FTLE in the MTS algorithm, we differentiate the Lagrangian evolution equation (2.5a) with respect to s, obtaining

$$\partial_t\xi_\alpha(s,t) = Du(\gamma_\alpha(s,t),t)\,\xi_\alpha(s,t), \qquad (s,t)\in\mathbb{T}\times(T_m,T_{m+1}), \quad \alpha = 1,\dots,N(T_m), \tag{2.10a}$$

with initial data

$$\xi_\alpha(s, T_m) \quad \text{generated by the MTS algorithm applied at time } t = T_m. \tag{2.10b}$$

Here Du denotes the velocity gradient. As with the interface evolution (2.5), classical Lagrangian tracking corresponds to bypassing the MTS reconstruction step in (2.10b) and directly continuing the tangent field from the preceding evolution interval. In the numerical method, (2.10a) is integrated alongside the interface evolution (2.5a), and the tangent FTLE diagnostic (2.9) is then evaluated *a posteriori* from the computed tangent field.[3] The resulting quantity provides a simple Lagrangian measure of localized tangential stretching and compression directly along the evolving interface family.

In contrast to curvature, the tangent FTLE correctly distinguishes between the two preceding examples. For the shrinking circle of Theorem 2.1, $|\partial_s\gamma(s,t)| = R_0 e^{-\lambda t}$ and $|\partial_s\gamma(s,0)| = R_0$, so that $\lambda^{\tan}(s,t) = e^{-\lambda t}$ and $\sigma^{\tan}(s,t) = -\lambda$. Thus, the tangent FTLE is spatially uniform and constant in time despite the unbounded growth of the curvature. For the localized-stretching example of Theorem 2.2, the tangent FTLE develops a pronounced localized maximum near the center of the interface, as shown in Figure 3(c). This maximum identifies the concentrated tangential stretching responsible for the filamentary region visible in Figure 3(a), whereas the curvature shown in Figure 3(b) remains bounded by its initial maximum value.

The preceding examples show that curvature and tangent FTLE capture different aspects of interface evolution, with curvature serving as an instantaneous geometric descriptor and the tangent FTLE as an accumulated Lagrangian geometric descriptor. Nevertheless, near filament *tips*, the two quantities become closely related [54, 4]. Using a local quadratic model, Thiffeault [54] derived a universal relationship between tangential stretching and curvature. In the present notation, this stretch–curvature relation takes the following form.

Proposition 2.3 (Stretch–curvature relation at a filament tip)**.** *Suppose that, near a filament tip, the interface admits the local representation*

$$\gamma(s,t) = (\beta s, f(s)), \qquad f(s) = \tfrac{1}{2}as^2 + \mathcal{O}(s^3), \qquad a, \beta > 0.$$

Then, as $s \to 0$*,*

$$\lambda^{\tan}(s,t) \sim \kappa(s,t)^{-1/3}, \tag{2.11a}$$

and consequently

$$\sigma^{\tan}(s,t) = -\tfrac{1}{3t}\log\kappa(s,t) + \mathcal{O}(t^{-1}). \tag{2.11b}$$

Proof. The local representation gives $\partial_s\gamma = (\beta, f'(s))$ and $\partial_s^2\gamma = (0, f''(s))$. Hence

$$\kappa(s,t) = \beta|f''(s)|\left(\beta^2 + f'(s)^2\right)^{-\frac{3}{2}}.$$

Since $f''(s) = a + \mathcal{O}(s)$ as $s \to 0$ and $|\partial_s\gamma(s,t)| = (\beta^2 + f'(s)^2)^{\frac{1}{2}}$, we obtain

$$\kappa(s,t) \sim |\partial_s\gamma(s,t)|^{-3},$$

after absorbing the fixed prefactor $\beta|a|$ into the asymptotic constant. Using (2.9a) and absorbing the factor $|\partial_s\gamma(s,0)|$, it follows that

$$\kappa(s,t) \sim \lambda^{\tan}(s,t)^{-3},$$

which upon rearranging yields (2.11a). Taking logarithms and using (2.9b) then yields (2.11b). □

The asymptotic relation (2.11) will be verified numerically in the benchmark problems considered below. From a computational perspective, the tangent FTLE possesses an important practical advantage: while curvature is a second-derivative quantity whose computation becomes highly sensitive near breakup at filament tips, the tangent FTLE is obtained from the evolution of the first-derivative tangent field and can be naturally continued through topological changes by the MTS reconstruction procedure. Consequently, the tangent FTLE provides a more robust diagnostic for tracking filamentation and subsequent breakup.

[3] Whenever adaptive refinement or coarsening modifies the interface discretization, both the tangent field $\xi_\alpha(s,t)$ and the reference quantity $|\xi_\alpha(s,0)|$ are transferred to the new interface nodes by interpolation.

2.4. **Lagrangian observation windows for visualizing filamentation.** As we will demonstrate below, one of the principal advantages of the Lagrangian tracking algorithm is its accuracy and efficiency in chaotic and multiscale flow regimes. As the complexity of the interface increases in such regimes, the formation and evolution of individual filaments (particularly at microscopic scales) become difficult to discern from global visualizations alone. To facilitate the qualitative analysis of these processes, we introduce a collection of *Lagrangian observation windows* that remain attached to selected material regions throughout the evolution. Let

$$c_j : [0, t_{\mathsf{max}}] \to \mathbb{R}^2, \qquad j = 1, \dots, N_{\mathsf{win}}, \tag{2.12a}$$

denote a collection of marker trajectories satisfying the Lagrangian evolution equation

$$\dot{c}_j(t) = u(c_j(t), t), \qquad c_j(0) = c_j^0, \tag{2.12b}$$

where the initial locations $\{c_j^0\}_{j=1}^{N_{\mathsf{win}}}$ are chosen according to the filamentary regions of interest. For each marker trajectory $c_j(t)$, we define the associated Lagrangian observation window

$$\mathcal{W}_j(t) = [c_j^1(t) - w_j(t),\, c_j^1(t) + w_j(t)] \times [c_j^2(t) - w_j(t),\, c_j^2(t) + w_j(t)], \tag{2.12c}$$

where $c_j = (c_j^1, c_j^2)$ and $w_j(t) > 0$ denotes a prescribed window half-width. Because the window centers evolve as passive Lagrangian markers, each observation window remains attached to the same material region throughout the evolution. In the numerical examples below, the initial marker locations are selected using the *a posteriori* curvature and tangent FTLE diagnostics introduced in Section 2.3, allowing the resulting observation windows to remain focused on filament-forming regions over long time intervals.

3. Two illustrative examples of Lagrangian tracking

We now consider two numerical examples to illustrate the prototypical features of the classical Lagrangian tracking algorithm described in Section 2: its excellent geometric accuracy and computational efficiency; and its inability to naturally resolve topological transitions, in agreement with observations reported previously in the literature [14]. At the same time, these examples introduce the tangent-FTLE diagnostic as a means of quantifying filamentation and identifying regions where fine-scale structures emerge. They therefore benchmark the current implementation while establishing a baseline comparison for the MTS methodology developed in subsequent sections.

3.1. **Rotating vortex benchmark.** The first example is the rotating vortex test, a standard benchmark problem for interface advection methods [46]. The prescribed incompressible velocity field u is defined as

$$\begin{aligned} u_1(x_1, x_2, t) &= -\cos\left(\tfrac{\pi t}{8}\right) \sin^2(\pi x_1) \sin(2\pi x_2), \\ u_2(x_1, x_2, t) &= \cos\left(\tfrac{\pi t}{8}\right) \sin(2\pi x_1) \sin^2(\pi x_2), \end{aligned} \tag{3.1}$$

and the initial interface is a circle of radius 0.15 centered at $(0.5, 0.75)$. The velocity gradient required for the tangent-FTLE computation (2.10a) is

$$Du(x_1, x_2, t) = \cos\left(\tfrac{\pi t}{8}\right) \begin{pmatrix} -\pi \sin(2\pi x_1) \sin(2\pi x_2) & -2\pi \sin^2(\pi x_1) \cos(2\pi x_2) \\ 2\pi \cos(2\pi x_1) \sin^2(\pi x_2) & \pi \sin(2\pi x_1) \sin(2\pi x_2) \end{pmatrix}. \tag{3.2}$$

The strong vortical flow continuously deforms the interface into increasingly thin filaments until reaching a state of maximum deformation at time $t = 4$, and then reverses direction and returns the interface toward its initial configuration at the final time $t_{\mathsf{max}} = 8$. The test therefore provides a convenient benchmark for assessing geometric accuracy, filament resolution, and computational efficiency.

We perform a resolution study by dyadic refinement of the fine-scale h using the Lagrangian tracking algorithm with parameters in Table 1 chosen as

$$t_{\mathsf{max}} = 8, \quad \Delta t = h, \quad h_0 = 0.04, \quad h = 2^{-p} h_0, \; p = 0, \dots, 5. \tag{3.3}$$

The numerical solution at the coarsest resolution $h = h_0$ is displayed as the blue curve in Figure 4 at the three times $t = 1, 4, 8$. At time $t = 4$, the deformed interface is characterized by two curved filament-tips at opposite "ends" of the vortical filamentary region. One end undergoes comparatively weak filament-tip formation, while the opposite end develops a much thinner and more strongly compressed filament tip.

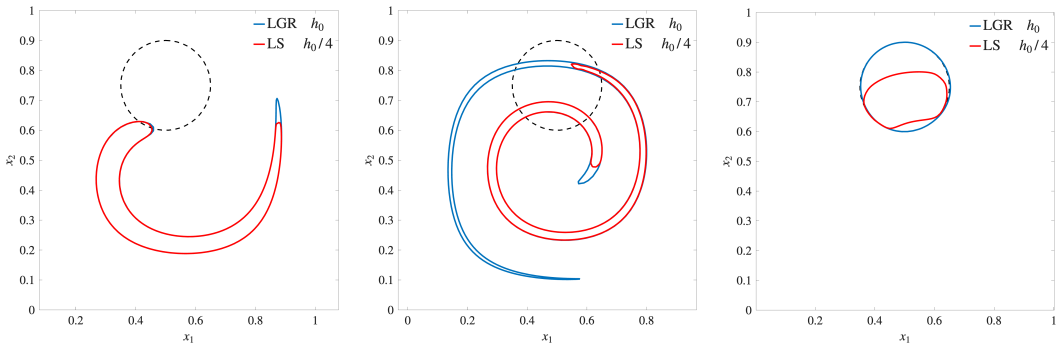

(A) $t = 1$ (B) $t = 4$ (C) $t = 8$

FIGURE 4. Comparison of classical Lagrangian tracking (blue) and a local level-set method (red) for the rotating vortex benchmark at times $t = 1, 4, 8$. The dashed black curve denotes the initial interface. The Lagrangian solution is computed using the coarse resolution $h = h_0$, while the level-set solution is computed using $h = h_0/4$.

3.1.1. *Benchmark comparison with classical Eulerian interface-capturing.* For comparison, we include results obtained using a simple Eulerian interface-capturing method, namely, a local level-set method [40]. In this approach, the signed distance function ϕ is evolved by the transport equation within a tube of radius $6h$, with reinitialization performed after every time-step to maintain the signed distance property.[4] The same sequence of spatial resolutions (3.3) is used for the level-set simulations, with the CFL-constrained time-step given by $\Delta t = 0.25h/\|u\|_\infty$. At the two coarsest resolutions $h = h_0, h_0/2$, the level-set solution undergoes catastrophic mass loss and disappears before the final time. Consequently, the red curves displayed in Figure 4 correspond to the level-set solution computed using the coarsest surviving resolution $h = h_0/4$. Even with four times the resolution, the level-set solution is unable to match the accuracy of the coarser Lagrangian solution.

3.1.2. *Resolution of filament tip and tangent FTLE diagnostics.* The left panel in Figure 5 displays the h-refined sequence of Lagrangian solutions at time $t = 4$, together with two successive zoom-ins of the filament tip. The first and second zoom-ins correspond to viewing windows of size $h_0 \times h_0/3$ and $h_0/16 \times h_0/48$, respectively. As the fine-scale h decreases, the Lagrangian solutions resolve the large-curvature region near the filament tip with increasing geometric fidelity.

The right panel of Figure 5 displays the tangent FTLE (2.9) at time $t = 4$ in blue together with the normalized curvature $\kappa(s, t_{\mathsf{max}})/\kappa(s, 0)$, where κ is defined in (2.3), in red. Two localized troughs in the tangent FTLE are observed near $s \approx \pi/2$ and $s \approx 3\pi/2$, corresponding respectively to the strong and weak filamentation at the two ends of the deformed interface. The sharper FTLE trough near $s \approx \pi/2$ is accompanied by a correspondingly larger curvature peak, while the broader FTLE trough near $s \approx 3\pi/2$ is associated with a weaker curvature response. As expected, the level-set error in Figure 4(c) is most pronounced near the strongly filamenting region at $s \approx \pi/2$, while a weaker but still visible error is also observed near the weaker filamenting region at $s \approx 3\pi/2$.

To verify the stretch–curvature relation (2.11), Figure 6 displays the accumulated tangent stretching $t\,\sigma^{\mathsf{tan}}(s, 4) = \log \lambda^{\mathsf{tan}}(s, 4)$ and logarithmic curvature $\log \kappa(s, 4)$ at the time of maximum deformation. The first two panels plot these quantities against the parameter s, while the third shows the phase plot in the $(\log \kappa,\, t\sigma^{\mathsf{tan}})$-plane. Two distinct branches are visible in the phase plot, corresponding to the strong and weak filamenting tips identified in Figure 5. Both branches exhibit the predicted $\kappa^{-1/3}$ scaling, with the strongly filamenting tip producing the longer branch.

3.1.3. *Convergence and scaling under h-refinement.* Finally, the accuracy and computational efficiency of the Lagrangian and level-set methods are compared quantitatively in Figure 7. For the sequence of resolutions

[4]This implementation is not intended to be representative of modern level-set methods, and is included only as a simple baseline comparison for the Lagrangian tracking method. More sophisticated methods typically provide improved accuracy at additional cost [16, 28, 37, 12].

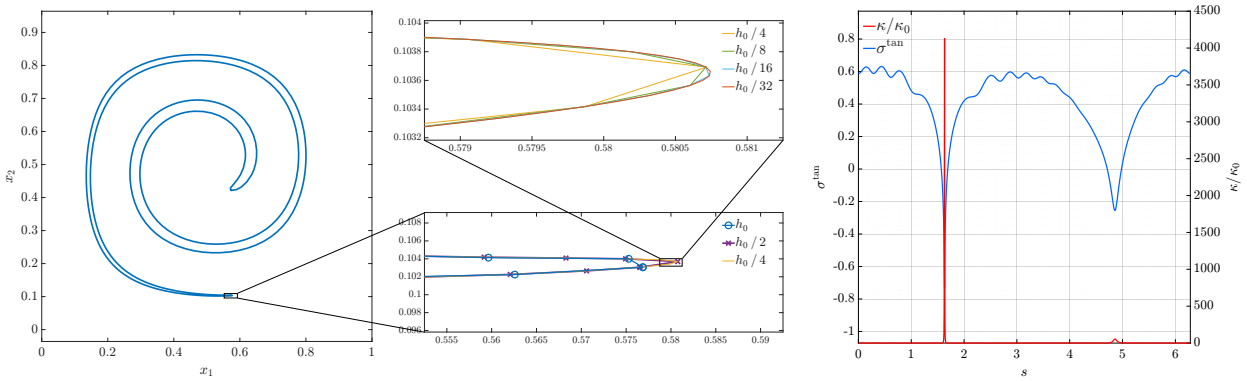

(A) Resolution of the filament tip (B) Tangent FTLE and curvature

FIGURE 5. Resolution of the filament tip and adaptive refinement for the rotating vortex benchmark at time $t = 4$. **Left:** Sequence of Lagrangian solutions computed with decreasing fine-scale h, together with successive zoom-ins of the filament tip illustrating the increasing geometric fidelity of the large-curvature region. Relative to the full computational domain $[0,1]^2$, the zoomed-in views correspond to windows with aspect ratios $h_0 \times h_0/3$ and $h_0/16 \times h_0/48$, respectively. **Right:** Tangent FTLE $\sigma^{\tan}(s,t)$ (2.9) and normalized curvature $\kappa(s,t)/\kappa(s,0)$ at the time of maximal deformation $t = 4$ for the finest Lagrangian simulation $h = h_0/32 = 1.25 \times 10^{-3}$. The two localized troughs of the tangent FTLE at $s \approx \frac{\pi}{2}, \frac{3\pi}{2}$ coincide with the curvature peaks at the filament tips.

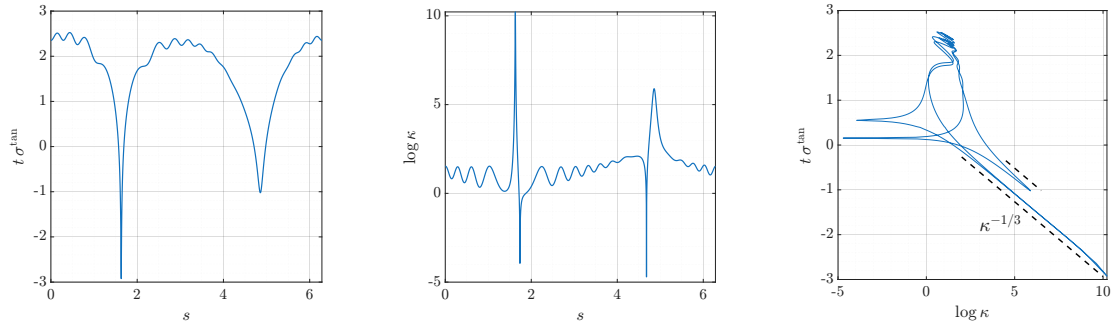

(A) $(s,\, t\sigma^{\tan}(s,4))$ (B) $(s,\, \log\kappa(s,4))$ (C) $(\log\kappa(s,4),\, t\sigma^{\tan}(s,4))$

FIGURE 6. Numerical verification of the stretch–curvature relation (2.11) for the rotating-vortex benchmark at the time of maximum deformation $t = 4$. The dashed lines in panel (c) denote the predicted $\kappa^{-1/3}$ scaling at the filamenting tips.

$h = 2^{-p}h_0$, we compute the diagnostics

$$|A_0 - A_*|, \qquad |A_K - A_0|, \qquad T_{\mathsf{cpu}}, \tag{3.4}$$

where A_* denotes the exact initial area enclosed by the interface, A_0 the numerical initial area, A_K the numerical area at the final time $t = t_{\mathsf{max}}$, and T_{cpu} the total computational runtime. The error $|A_K - A_0|$ will be referred to henceforth as the *numerical reversal error*. The results are displayed in Figure 7. While both methods produce numerical reversal errors that converge with approximately second-order accuracy, the Lagrangian errors are three orders of magnitude smaller than the corresponding level-set errors at the same resolution. Similarly, although both methods exhibit the expected $\mathcal{O}(h^{-2})$ scaling in computational cost, the Lagrangian method is approximately two orders of magnitude faster over the range of resolutions considered here.

3.2. **Filamentation by alternating nonlinear shears.** While the rotating-vortex benchmark provides a useful test of accuracy, the results of Section 3.1 show that it does not generate the extreme multiscale filamentary structures needed to fully stress methods for tracking or capturing the interface. To address this limitation, AHN AND SHASHKOV [1] introduced more demanding filamentation tests for assessing the ability of MOF methods to preserve thin interfacial structures. These tests have subsequently been adopted and

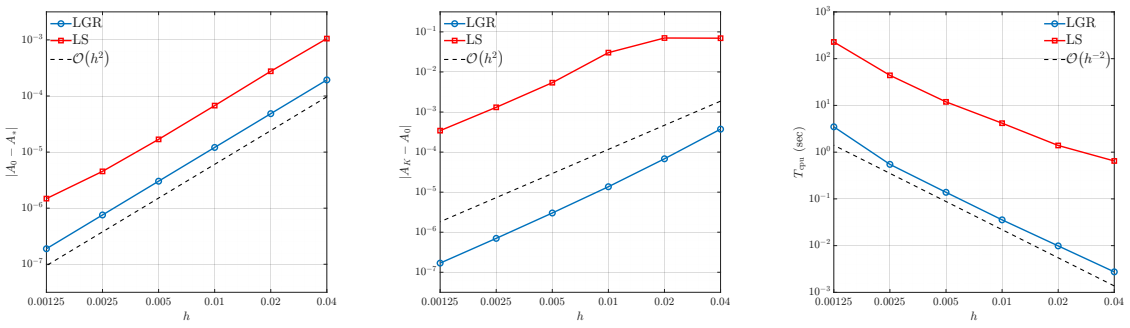

(A) $|A_0 - A_*|$ (B) $|A_K - A_0|$ (C) T_{cpu}

FIGURE 7. Quantitative comparison of the Lagrangian interface tracking and local level-set methods for the rotating vortex benchmark. The diagnostics (3.4) are displayed as functions of the characteristic length scale h. **Left:** Initial area error $|A_0 - A_*|$. **Center:** Numerical reversal error $|A_K - A_0|$ at $t = t_{\text{max}}$. **Right:** Total computational runtime T_{cpu}.

further developed in later studies using filament-aware MOF methods [30, 25, 26]. One such filamentation test, the $\mathcal{S}$-flow, will be considered later in Section 7.3.

In the same spirit, we consider a nonlinear *alternating-shear* test that generates substantially greater interface complexity than the filamentation tests comprising the standard MOF test suite. In the chaotic-advection literature, alternating-shear maps have been used extensively to study the generation of fine-scale structure through repeated stretching and folding. PIERREHUMBERT [41, 42], for instance, employed randomized alternating-shear deformations to investigate tracer microstructure generated by chaotic mixing in Rossby–Haurwitz wave dynamics, where filamentation is ultimately arrested by diffusion. Here, we study the analogous problem for material interfaces, replacing the Batchelor-scale diffusive regularization of tracer filaments by the microscale topological regularization of tracked interfaces. To this end, we introduce a deterministic and reversible alternating-shear benchmark that retains the strong filamentation of chaotic-advection models while providing a reproducible setting for numerical verification.

For each integer $m \geq 0$, we define the m-th alternating-shear map by the composition

$$F_m = S_{m,2} \circ S_{m,1}, \tag{3.5a}$$

where $S_{m,1}$ and $S_{m,2}$ are the horizontal and vertical shears

$$S_{m,1}(x_1, x_2) = (x_1 + \lambda \sin(kx_2 + \varphi_m),\, x_2)\,, \tag{3.5b}$$

$$S_{m,2}(x_1, x_2) = (x_1,\, x_2 + \lambda \sin(kx_1 + \psi_m))\,, \tag{3.5c}$$

the phase shifts $\{\varphi_m, \psi_m\}$ are given by

$$\varphi_m = 2\pi\left(\sqrt{2}(m+1) + 0.173(m+1)^2\right) \qquad \text{and} \qquad \psi_m = 2\pi\left(\sqrt{3}(m+1) + 0.217(m+1)^2\right), \tag{3.5d}$$

and $\{\lambda, k\}$ are the amplitude and frequency of the sinusoidal deformations. We use the values

$$\lambda = 0.2 \qquad \text{and} \qquad k = 4 \tag{3.5e}$$

in the numerical experiment below. The inverse map is obtained by undoing the two shears:

$$F_m^{-1} = S_{m,1}^{-1} \circ S_{m,2}^{-1}, \tag{3.5f}$$

where

$$S_{m,1}^{-1}(x_1, x_2) = (x_1 - \lambda \sin(kx_2 + \varphi_m),\, x_2)\,, \tag{3.5g}$$

$$S_{m,2}^{-1}(x_1, x_2) = (x_1,\, x_2 - \lambda \sin(kx_1 + \psi_m))\,. \tag{3.5h}$$

3.2.1. *C^1-in-time embedding of the discrete dynamics.* For Lagrangian tracking (2.5a), we consider a long-time simulation on the interval $[0, t_{\text{max}}]$ with $t_{\text{max}} = 30$, generated by a smooth divergence-free velocity field which coincides with the alternating-shear maps at integer times. The flow consists of a forward deformation phase on $0 \leq t \leq t_{\text{max}}/2$ followed by a reversal phase on $t_{\text{max}}/2 \leq t \leq t_{\text{max}}$, allowing the final configuration to be compared directly with the initial interface.

For $t \in [m, m+1]$, let

$$\tau = t - m, \qquad 0 \le \tau \le 1,$$

and let $f, g : [0,1] \to \mathbb{R}$ denote compactly supported temporal weights satisfying

$$f(\tau) = 0, \quad \tfrac{1}{2} \le \tau \le 1, \qquad \text{and} \qquad g(\tau) = 0, \quad 0 \le \tau \le \tfrac{1}{2}, \tag{3.6a}$$

with the normalization conditions

$$\int_0^{\frac{1}{2}} f(\tau)\,\mathrm{d}\tau = 1 \qquad \text{and} \qquad \int_{\frac{1}{2}}^1 g(\tau)\,\mathrm{d}\tau = 1. \tag{3.6b}$$

The minimal-degree C^1 polynomials satisfying these conditions are

$$f(\tau) = \begin{cases} 960\,\tau^2\left(\tfrac{1}{2} - \tau\right)^2, & 0 \le \tau \le \tfrac{1}{2}, \\ 0, & \tfrac{1}{2} < \tau \le 1, \end{cases} \qquad \text{and} \qquad g(\tau) = \begin{cases} 0, & 0 \le \tau < \tfrac{1}{2}, \\ 960\,(\tau - \tfrac{1}{2})^2(1-\tau)^2, & \tfrac{1}{2} \le \tau \le 1. \end{cases} \tag{3.6c}$$

For $0 \le t < t_{\mathsf{max}}/2$, let

$$m = \lfloor t \rfloor, \qquad \tau_f = t - m, \tag{3.7a}$$

while for $t_{\mathsf{max}}/2 \le t \le t_{\mathsf{max}}$, let

$$q = \left\lfloor t - \tfrac{t_{\mathsf{max}}}{2} \right\rfloor, \qquad m = \tfrac{t_{\mathsf{max}}}{2} - 1 - q, \qquad \tau_r = t - \tfrac{t_{\mathsf{max}}}{2} - q. \tag{3.7b}$$

We then define the velocity field

$$u(x,t) = \begin{cases} \begin{pmatrix} \lambda f(\tau_f)\sin(kx_2 + \varphi_m) \\ \lambda g(\tau_f)\sin(kx_1 + \psi_m) \end{pmatrix}, & 0 \le t < t_{\mathsf{max}}/2, \\ \begin{pmatrix} -\lambda g(\tau_r)\sin(kx_2 + \varphi_m) \\ -\lambda f(\tau_r)\sin(kx_1 + \psi_m) \end{pmatrix}, & t_{\mathsf{max}}/2 \le t \le t_{\mathsf{max}}. \end{cases} \tag{3.7c}$$

During the forward phase, the first half of each interval applies the horizontal shear $S_{m,1}$, while the second half applies the vertical shear $S_{m,2}$. Consequently, the flow coincides at integer times with the compositions

$$\gamma_\alpha(s, m) = (F_{m-1} \circ \cdots \circ F_0)\big(\gamma_\alpha(s,0)\big), \qquad m = 1, \dots, t_{\mathsf{max}}/2. \tag{3.8a}$$

During reversal, the first half of each interval applies $S_{m,2}^{-1}$, while the second half applies $S_{m,1}^{-1}$, so that

$$\gamma_\alpha(s, t_{\mathsf{max}}) = \gamma_\alpha(s, 0). \tag{3.8b}$$

The velocity gradient required for the tangent-FTLE computation (2.10a) is

$$Du(x,t) = \begin{cases} \begin{pmatrix} 0 & \lambda k f(\tau_f)\cos(kx_2 + \varphi_m) \\ \lambda k g(\tau_f)\cos(kx_1 + \psi_m) & 0 \end{pmatrix}, & 0 \le t < t_{\mathsf{max}}/2, \\ \begin{pmatrix} 0 & -\lambda k g(\tau_r)\cos(kx_2 + \varphi_m) \\ -\lambda k f(\tau_r)\cos(kx_1 + \psi_m) & 0 \end{pmatrix}, & t_{\mathsf{max}}/2 \le t \le t_{\mathsf{max}}. \end{cases} \tag{3.9}$$

3.2.2. *Qualitative and quantitative analysis of filamentation.* We compute a sequence of simulations using the Lagrangian tracking algorithm with

$$t_{\mathsf{max}} = 30, \quad h = 2^{-p} h_0, \quad \Delta t = 2^{-p}\Delta t_0, \quad p = 0, \dots, 5, \qquad \text{with} \quad h_0 = 0.06, \quad \Delta t_0 = 8.0 \times 10^{-3}. \tag{3.10}$$

The solution computed with the intermediate resolution $h = h_0/8$ is shown in Figure 8(a) at the time of maximal deformation, $t = 15$. The repeated alternating-shear mechanism generates thin filamentary structures spanning a broad range of scales. In light of the results of Section 3.1, obtaining a solution of acceptable quality with the baseline level-set method would be prohibitively expensive on the current computational platform.

The tangent FTLE (2.9) at $t = 15$ is displayed as the blue curve in Figure 8(b). Compared with the rotating vortex benchmark, the alternating-shear flow exhibits significantly more intricate multiscale structure, reflecting the repeated generation and interaction of filamentary regions throughout the evolution. For

comparison, the curvature $\kappa(s, t_{\mathsf{max}})$ of the final interface is displayed as the red curve. The peaks of the curvature align closely with sharp troughs of the tangent FTLE at the material locations

$$(\theta_1, \theta_2, \theta_3, \theta_4) = (2.876025,\ 3.451420,\ 4.324865,\ 4.812920). \tag{3.11}$$

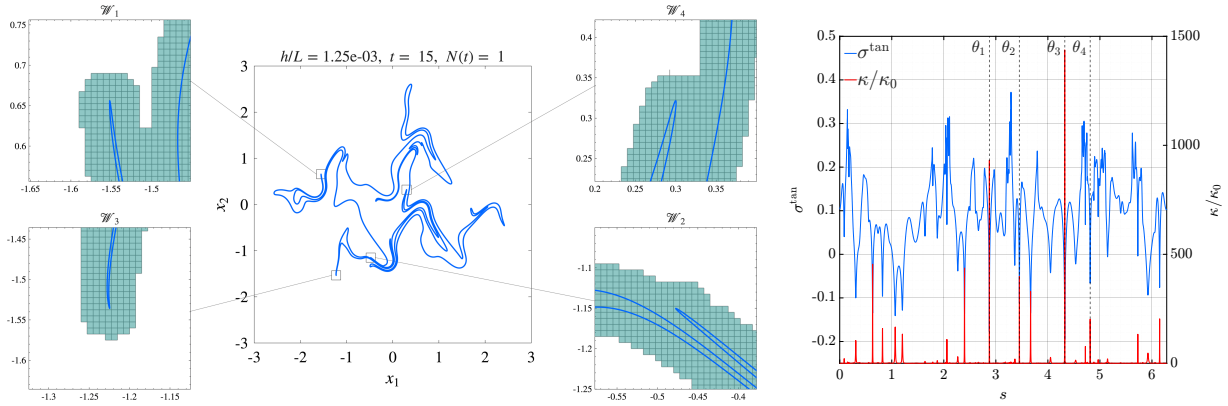

(A) Alternating-shear filamentation at $t = 15$ (B) Tangent FTLE and curvature

FIGURE 8. Filamentation generated by repeated application of the alternating-shear deformation (3.5). Results are shown for the classical Lagrangian tracking method with parameters (3.10), using the intermediate resolution $h = h_0/8$. **Left:** Adaptively refined Lagrangian solution at the time of maximal deformation, $t = 15$, together with a sequence of localized Lagrangian observation windows illustrating the formation of thin filamentary structures. For reference, each window also displays a local Cartesian grid patch at the prescribed microscale resolution h. The repeated shearing mechanism generates thin filaments with sub-microscale geometry which are captured by the Lagrangian solution with high fidelity. A video of the complete evolution is available at [44]. **Right:** Tangential FTLE (2.9) (blue), together with the curvature of the final deformed interface (red). The marked locations $\theta_1, \ldots, \theta_4$ correspond to sharp localized troughs of the tangent FTLE, and are used to track the filament-forming regions shown in the left panel.

To quantify the accuracy and computational cost of the classical Lagrangian tracking method, we consider the recovery of the initial interface at the final time $t = t_{\mathsf{max}}$. The left panel of Figure 9 compares the initial and final interfaces for the intermediate resolution $h = h_0/8$. The two interfaces are visually indistinguishable, indicating that the method maintains excellent accuracy despite the severe deformation observed at intermediate times. The center and right panels of Figure 9 provide quantitative diagnostics. The numerical reversal error $|A_K - A_0|$ exhibits second-order convergence under mesh refinement, while the computational runtime scales as $\mathcal{O}(h^{-2})$.

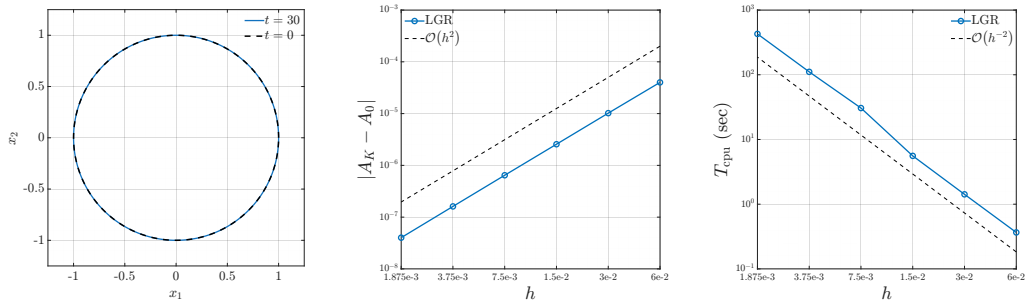

(A) $\Gamma(s,t)$ at $t = 0$ and $t = t_{\mathsf{max}}$ (B) $|A_K - A_0|$ (C) T_{cpu}

FIGURE 9. Convergence study for the nonlinear alternating-shear test using the classical Lagrangian tracking method and the parameter sequence (3.10). **Left:** Initial ($t = 0$) and final ($t = t_{\mathsf{max}}$) interfaces for the intermediate resolution $h = h_0/8$. **Center:** Numerical reversal error $|A_K - A_0|$ as a function of the fine-scale resolution h. **Right:** Computational runtime as a function of h.

We now return to the filament-forming regions highlighted in Figure 8. In agreement with the filamentation studies of PIERREHUMBERT [41, 42], the underlying interface exhibits exponential length growth, $|\Gamma(t)| \sim$

$|\Gamma(0)|e^{0.146t}$. Since the enclosed area is conserved, this growth implies a corresponding decrease in the characteristic transverse scale of the filamentary structure. To track this process qualitatively, we use the Lagrangian observation windows (2.12), with

$$N_{\mathsf{win}} = 4, \qquad w_j = 0.1, \qquad c_j(0) = (\cos\theta_j, \sin\theta_j), \qquad \text{and } \theta_j \text{ given by (3.11).} \tag{3.12}$$

From the localized windows in Figure 8(a), we observe that the filaments in the $\mathcal{W}_1$, $\mathcal{W}_2$, and $\mathcal{W}_3$ windows fall below the prescribed fine scale h, while the filament in the $\mathcal{W}_4$ window approaches this threshold. The most severe filamentation occurs in $\mathcal{W}_3$, followed by $\mathcal{W}_1$; both are associated with pronounced tangent-FTLE troughs and large curvature concentrations in Figure 8(b). By contrast, the $\mathcal{W}_2$ and $\mathcal{W}_4$ windows exhibit weaker filamentation, consistent with their shallower tangent-FTLE troughs and smaller curvature concentrations. The corresponding phase-space plots in Figure 10 show that the filament-tip regions in all four windows are consistent with the $\kappa^{-1/3}$ stretch–curvature scaling (2.11).

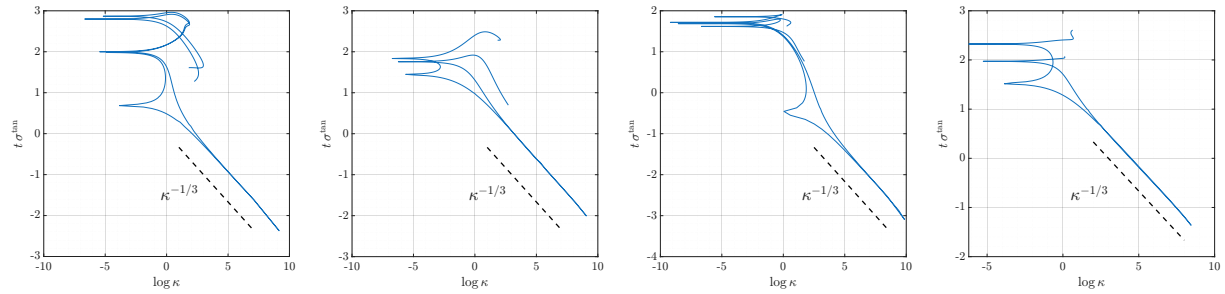

(A) $\mathcal{W}_1$ (B) $\mathcal{W}_2$ (C) $\mathcal{W}_3$ (D) $\mathcal{W}_4$

FIGURE 10. Accumulated tangent stretching $t\sigma^{\tan}$ and logarithmic curvature $\log\kappa$ in the observation windows $\mathcal{W}_1, \ldots, \mathcal{W}_4$ for the nonlinear alternating-shear test. The dashed line denotes the $\kappa^{-1/3}$ scaling (2.11).

For this problem, a natural large-scale deformation length is given by the diameter of the box containing the interface at final time $t = t_{\mathsf{max}}$, which we approximate here by $L = 6$. Consequently, the scale-separation ratio for the intermediate resolution $h = h_0/8$ is $h/L = 1.25 \times 10^{-3}$. The excellent geometric fidelity and computational efficiency of classical Lagrangian tracking are accompanied by a fundamental topological rigidity of the representation, forcing thin filaments to persist even when they fall below microscopic scales. The MTS framework developed in the following sections overcomes this limitation by introducing controlled topological reconstruction at the microscale resolution.

4. Capturing topological transitions by an Eulerian snapshot

In this section, we describe the first stage of the core MTS algorithm: *extracting* a topologically-corrected interface family from an *Eulerian snapshot*. Several front-tracking methods have employed auxiliary Eulerian representations to detect or resolve topological transitions [19, 14, 5, 50], exploiting the fact that Eulerian representations naturally encode connectivity while Lagrangian representations provide highly accurate geometric information. The present approach lies in the category of methods that construct an auxiliary Eulerian field from a Lagrangian interface and recover a topologically corrected interface from an isocontour of that field. In the MTS algorithm, the Eulerian field is taken to be a signed-distance function, as in [6, 7, 49, 58, 35], although alternative choices, such as smoothed indicator functions, are also possible [48, 52, 18].

Suppose that the family of interfaces $\{\Gamma_\alpha(t)\}$ has been evolved over the time interval (T_{m-1}, T_m) by the Lagrangian tracking algorithm, and the MTS algorithm is then applied at time $t = T_m$. We denote the *pre-processed* Lagrangian interface family by

$$\{\mathcal{L}_\alpha\}_{\alpha=1}^{N_{\mathsf{lgr}}}, \qquad \text{with} \quad \mathcal{L}_\alpha := \Gamma_\alpha(T_m^-), \quad \ell_\alpha(s) := \gamma_\alpha(s, T_m^-), \quad \text{and} \quad N_{\mathsf{lgr}} := N(T_m^-). \tag{4.1}$$

The interface family $\{\mathcal{L}_\alpha\}$ is first converted into an Eulerian representation through the *signed-distance function* (SDF),

$$\phi(x) := \pm \min_\alpha \operatorname{dist}(x, \mathcal{L}_\alpha), \tag{4.2}$$

defined on a local fine-scale Cartesian grid with cell size h. The zero-level set

$$\Sigma_\phi := \{x \in \mathbb{R}^2 : \phi(x) = 0\} \tag{4.3a}$$

defines the (Eulerian) *extracted* interface family,

$$\{\mathcal{E}_\beta\}_{\beta=1}^{N_{\mathsf{eul}}} \coloneqq \mathrm{Conn}(\Sigma_\phi), \qquad \text{with} \quad N_{\mathsf{eul}} \coloneqq \#\,\mathrm{Conn}(\Sigma_\phi). \tag{4.3b}$$

Here, $\mathrm{Conn}(A)$ denotes the collection of connected components of a set A, while $\#A$ denotes its cardinality, so that N_{eul} is the number of connected components. In the remainder of this section, we describe an efficient narrow-band method to compute the SDF (4.2), along with the simple marching-squares procedure used to extract the Eulerian interface family (4.3).

4.1. **Efficient construction of the signed-distance function.** Let $\Omega_{\mathrm{ref}} \subset \mathbb{R}^2$ denote a fixed reference domain containing the Lagrangian interface family $\{\mathcal{L}_\alpha\}$, and let h_0 denote the mesh spacing of a coarse Cartesian grid on Ω_{ref}. The fine-scale h is defined by dyadic refinement of h_0,

$$h = 2^{-p}h_0, \quad p \geq 0, \qquad \text{with } h_0 > 0 \text{ prescribed.} \tag{4.4}$$

With the dyadic refinement (4.4), each coarse grid cell is subdivided into $2^p \times 2^p$ refined cells of size h.

Given the pre-processed interface family $\{\mathcal{L}_\alpha\}_{\alpha=1}^{N_{\mathsf{lgr}}}$, the SDF is constructed only within the narrow tubular neighborhood

$$\mathcal{N}_h \coloneqq \left\{ x \in \mathbb{R}^2 : \min_\alpha \mathrm{dist}(x, \mathcal{L}_\alpha) \leq 3h \right\}. \tag{4.5}$$

Let $\mathcal{G}_h \subset \mathcal{N}_h$ denote the refined Cartesian grid nodes, and let $N_{\mathsf{grid}} \coloneqq \#\mathcal{G}_h$. The total number of polygonal interface segments is denoted by $N_{\mathsf{seg}} \coloneqq \sum_{\alpha=1}^{N_{\mathsf{lgr}}} N_\alpha$. For each node $x_i \in \mathcal{G}_h$, the unsigned distance is computed by

$$d_i \coloneqq \min_\alpha \mathrm{dist}(x_i, \mathcal{L}_\alpha), \tag{4.6}$$

and the sign is assigned by ray-casting via

$$n_i \coloneqq \#\left(R_i \cap \bigcup_{\alpha=1}^{N_{\mathsf{lgr}}} \mathcal{L}_\alpha \right), \qquad R_i \coloneqq \{x_i + s(1,0) : s > 0\}, \qquad \phi_i \coloneqq (-1)^{n_i} d_i. \tag{4.7}$$

A direct brute-force implementation computes

$$d_i = \min_{\alpha=1,\ldots,N_{\mathsf{lgr}}} \min_{j=1,\ldots,N_\alpha} \mathrm{dist}(x_i, S_{\alpha,j}), \qquad i = 1, \ldots, N_{\mathsf{grid}}, \tag{4.8}$$

requiring $\mathcal{O}\big(N_{\mathsf{grid}} \times N_{\mathsf{seg}}\big)$ point-to-segment distance evaluations. Similarly, the ray-casting procedure requires testing each horizontal ray against all interface segments, yielding the same computational complexity.

To obtain a scalable algorithm, we reverse the order of the computation: rather than testing every grid node against every interface segment, each segment deposits distance information only to nearby refined-grid nodes. The same locality principle is used for ray-casting by binning candidate crossing segments by horizontal grid row. A complete description of the method is given in Algorithm 2 in Section A.

Under the adaptive refinement criterion described in Section 2.2, the polygonal segments satisfy $|S_{\alpha,j}| = \mathcal{O}(h)$, so that the $3h$-neighborhood of each segment intersects only $\mathcal{O}(1)$ refined cells. Consequently, each segment deposits distance information to only $\mathcal{O}(1)$ refined-grid nodes, yielding a total unsigned-distance construction cost of $\mathcal{O}(N_{\mathsf{seg}})$. The same localization principle is used in the ray-casting procedure. Each segment is inserted only into the horizontal refined-grid rows intersecting its vertical extent. Since the segment length is $\mathcal{O}(h)$, each segment intersects only $\mathcal{O}(1)$ rows, so the row-binning stage also costs $\mathcal{O}(N_{\mathsf{seg}})$. Moreover, under the narrow-band construction and adaptive refinement, the number of candidate crossing segments associated with each row remains uniformly bounded independently of resolution. Therefore, each ray-casting query requires only $\mathcal{O}(1)$ segment intersection tests, giving a total sign-construction cost of $\mathcal{O}(N_{\mathsf{grid}})$. Hence the proposed localized SDF construction has complexity $\mathcal{O}\big(N_{\mathsf{seg}} + N_{\mathsf{grid}}\big)$.

4.2. **Interface extraction from the zero-level set.** With the SDF in hand, the extraction of the topologically-corrected interface family $\{\mathcal{E}_\beta\}_{\beta=1}^{N_{\mathsf{eul}}}$ from the zero-level set proceeds in three stages:

$$\text{Identify connected components} \;\rightarrow\; \text{Trace component curves} \;\rightarrow\; \text{Refine \& filter}$$

The first stage of the extraction process identifies the connected components of Σ_ϕ (and therefore also N_{eul}, i.e., the number of extracted curves) through a standard graph-based marching-squares construction [32, 58, 35, 18]. The second stage converts each graph component into an ordered polygonal curve. For each component label β, we select a starting vertex in the corresponding connected component of G_ϕ and

traverse the graph by repeatedly moving to the neighboring vertex that is not the previous vertex. The physical coordinates of the visited vertices define an extracted polygonal curve $\mathcal{E}_\beta = \{e_{\beta,1}, \ldots, e_{\beta,N_\beta}\}$, which is subsequently processed in the third stage of the extraction pipeline by a refinement and small-scale filtering procedure. The complete extraction pipeline, given in Algorithms 3, 4, and 5 in Section A, therefore yields a topologically-corrected Eulerian interface family $\{\mathcal{E}_\beta\}_{\beta=1}^{N_{\mathsf{eul}}}$ associated with the original Lagrangian interface family $\{\mathcal{L}_\alpha\}_{\alpha=1}^{N_{\mathsf{lgr}}}$. In the next stage of the MTS algorithm, these two interface families are related through a graph-theoretic adjacency topology, which forms the basis for both topological transition detection and subsequent surgical rebuild.

5. Building the adjacency topology and classifying topological events

At this stage of the algorithm, the pre-processed Lagrangian family $\{\mathcal{L}_\alpha\}_{\alpha=1}^{N_{\mathsf{lgr}}}$ and the extracted Eulerian family $\{\mathcal{E}_\beta\}_{\beta=1}^{N_{\mathsf{eul}}}$ generally do not match geometrically or topologically. The central goal of this section is to infer the *adjacency topology* between the two interface families from their underlying geometric configuration, and thereby flag topological transitions.

The inferred adjacency topology is represented by a bipartite graph G, following the general philosophy of parent–child connectivity constructions used in [19, 14, 5, 18]. The bipartite graph is denoted by

$$G = (V, W, E), \tag{5.1a}$$

with vertex sets

$$V = \{\mathcal{L}_\alpha\}_{\alpha=1}^{N_{\mathsf{lgr}}} \quad \text{and} \quad W = \{\mathcal{E}_\beta\}_{\beta=1}^{N_{\mathsf{eul}}}. \tag{5.1b}$$

The edge set

$$E \subset V \times W \tag{5.1c}$$

encodes adjacency relations between the Lagrangian and Eulerian interfaces. In practice, the graph may be represented by a binary adjacency matrix

$$\mathcal{A} \in \{0,1\}^{N_{\mathsf{lgr}} \times N_{\mathsf{eul}}}, \qquad \text{with} \quad \mathcal{A}_{\alpha\beta} = 1 \iff (\mathcal{L}_\alpha, \mathcal{E}_\beta) \in E. \tag{5.2}$$

The MTS algorithm computes the adjacency matrix $\mathcal{A}$ through a robust pipeline consisting of candidate adjacency construction followed by geometric pruning. A candidate graph is first constructed from local geometric proximity information, after which fine-scale geometric compatibility criteria are used to remove spurious edges and produce the final adjacency topology.

Then, the connected components of the bipartite graph are extracted to define independent local topological events $\{\mathcal{T}_1, \ldots, \mathcal{T}_{N_{\mathsf{event}}}\}$, which are classified as:

- *trivial* events, corresponding to one-to-one relations;
- *vanishing* events, corresponding to interfaces with no descendants;
- or *branching* events, corresponding to one-to-many or many-to-one adjacencies;

Topology change is then flagged by the presence of any nontrivial event.

5.1. Candidate adjacency topology with geometric pruning.

In this subsection, we construct a preliminary adjacency matrix

$$\widetilde{\mathcal{A}} \in \{0,1\}^{N_{\mathsf{lgr}} \times N_{\mathsf{eul}}}, \tag{5.3}$$

which encodes parent–child relations between the Lagrangian and Eulerian interfaces. The construction combines geometric proximity tests with successive pruning stages designed to remove geometrically inadmissible attachments, followed by a final parent-existence enforcement step. The individual stages of the construction are described below.

(1) *Candidate adjacency by* lgr-eul *proximity:* We first construct a candidate adjacency relation using pairwise geometric proximity between $\{\mathcal{L}_\alpha\}_{\alpha=1}^{N_{\mathsf{lgr}}}$ and $\{\mathcal{E}_\beta\}_{\beta=1}^{N_{\mathsf{eul}}}$. For each pair $(\mathcal{L}_\alpha, \mathcal{E}_\beta)$, we define the minimum separation distance

$$d_{\alpha\beta} \coloneqq \inf_{s,\bar{s}} \left|\ell_\alpha(s) - e_\beta(\bar{s})\right|. \tag{5.4a}$$

The matrix $\widetilde{\mathcal{A}}$ is then defined by

$$\widetilde{\mathcal{A}}_{\alpha\beta} = 1 \quad \Longleftrightarrow \quad d_{\alpha\beta} \le h. \tag{5.4b}$$

(2) *Merge pruning by* lgr–lgr *proximity:* Candidate multi-parent attachments necessarily correspond to local merge events. By construction, a merge can occur only when the participating Lagrangian interfaces come within distance h of one another. Consequently, whenever an extracted interface possesses multiple candidate parents, the corresponding parent interfaces are required to lie within distance h of one another. Suppose that $\mathcal{E}_\beta$ possesses multiple candidate parents, so that $\widetilde{\mathcal{A}}_{\alpha_1\beta} = \widetilde{\mathcal{A}}_{\alpha_2\beta} = 1$ for some $\alpha_1 \neq \alpha_2$. For each such pair (α_1, α_2), we define the lgr-lgr separation distance

$$d^{\mathsf{lgr}}_{\alpha_1\alpha_2} \coloneqq \inf_{s,\bar{s}} |\ell_{\alpha_1}(s) - \ell_{\alpha_2}(\bar{s})| \,. \tag{5.5a}$$

Whenever $d^{\mathsf{lgr}}_{\alpha_1\alpha_2} > h$, the attachment associated with the larger lgr-eul separation distance is removed according to

$$d^{\mathsf{lgr}}_{\alpha_1\alpha_2} > h \implies \begin{cases} \widetilde{\mathcal{A}}_{\alpha_1\beta} = 0, & \text{if } d_{\alpha_1\beta} \geq d_{\alpha_2\beta}, \\ \widetilde{\mathcal{A}}_{\alpha_2\beta} = 0, & \text{if } d_{\alpha_1\beta} < d_{\alpha_2\beta}. \end{cases} \tag{5.5b}$$

This pruning procedure is repeated until all remaining multi-parent attachments satisfy $d^{\mathsf{lgr}}_{\alpha_1\alpha_2} \leq h$.

(3) *Local geometric overlap pruning:* The remaining multi-parent attachments are further pruned using a local geometric overlap criterion. For each $\mathcal{L}_\alpha$, define the node-ball covering

$$\mathcal{B}_\alpha \coloneqq \bigcup_i B_{h/4}(\ell_{\alpha,i}), \qquad \text{where} \quad B_r(x) \coloneqq \{y \in \mathbb{R}^2 : |x - y| \leq r\}. \tag{5.6a}$$

Whenever the extracted interface fails to intersect the node-ball covering, the corresponding attachment is removed:

$$\mathcal{E}_\beta \cap \mathcal{B}_\alpha = \varnothing \implies \widetilde{\mathcal{A}}_{\alpha\beta} = 0. \tag{5.6b}$$

(4) *Parent existence enforcement:* Finally, every extracted Eulerian interface is required to be adjacent to at least one pre-processed Lagrangian interface. More precisely, whenever

$$\sum_{\alpha=1}^{N_{\mathsf{lgr}}} \widetilde{\mathcal{A}}_{\alpha\beta} = 0, \tag{5.7a}$$

the nearest Lagrangian interface is attached:

$$\widetilde{\mathcal{A}}_{\alpha^*\beta} = 1, \qquad \alpha^* \coloneqq \arg\min_\alpha d_{\alpha\beta}. \tag{5.7b}$$

Remark 5.1. *To accelerate the geometric queries arising throughout the adjacency topology construction, each interface is first associated with a padded axis-aligned bounding box [18]. For a curve $\Gamma \subset \mathbb{R}^2$, we define*

$$B_h(\Gamma) \coloneqq [x^1_{\min} - h, x^1_{\max} + h] \times [x^2_{\min} - h, x^2_{\max} + h], \qquad x^i_{\min} \coloneqq \min_{x\in\Gamma} x^i, \quad x^i_{\max} \coloneqq \max_{x\in\Gamma} x^i. \tag{5.8a}$$

These bounding boxes are subsequently used as cheap geometric rejection criteria in the pairwise proximity and pruning stages. Specifically, the candidate lgr–eul *pair $(\mathcal{L}_\alpha, \mathcal{E}_\beta)$ is discarded whenever*

$$B_h(\mathcal{L}_\alpha) \cap B_h(\mathcal{E}_\beta) = \varnothing, \tag{5.8b}$$

and, for surviving pairs, the geometric proximity query is localized to the intersection region

$$B_h(\mathcal{L}_\alpha) \cap B_h(\mathcal{E}_\beta). \tag{5.8c}$$

5.2. **Topology-change detection and event classification.** We now use the inferred adjacency topology to decompose the global topology into independent local events, classify the resulting event structure, and thereby detect topological changes. The preliminary adjacency matrix $\widetilde{\mathcal{A}}$ constructed in Section 5.1 defines a bipartite graph G, whose connected components define independent local topological *events* $\mathcal{T}_q$.

We denote the connected components of G by

$$\mathcal{T}_q = (V_q, W_q, E_q) \,, \qquad q = 1, \ldots, N_{\mathsf{event}}, \tag{5.9a}$$

where $V_q \subset V$, $W_q \subset W$, and

$$E_q = E \cap (V_q \times W_q) \,.$$

Equivalently,

$$N_{\mathsf{event}} \coloneqq \#\,\mathrm{CC}(G), \qquad \{\mathcal{T}_q : q = 1, \ldots, N_{\mathsf{event}}\} \coloneqq \mathrm{CC}(G), \tag{5.9b}$$

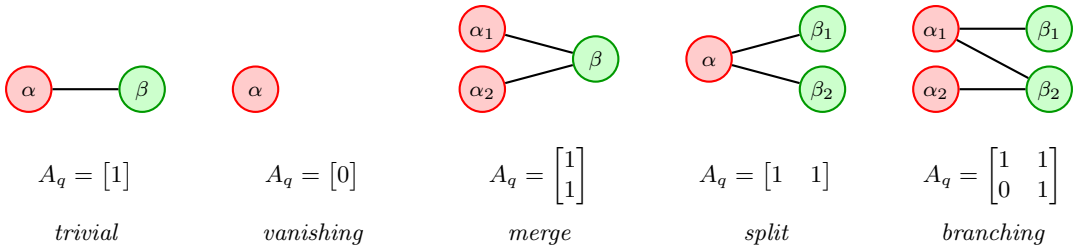

FIGURE 11. Representative local topological events and their associated adjacency submatrices A_q. Red vertices denote pre-processed Lagrangian interfaces, green vertices denote extracted Eulerian components, and black edges denote adjacency. The *trivial* and *vanishing* events do not require surgical reconstruction, whereas the *merge*, *split*, and more general *branching* events trigger the interface surgery.

where $\mathrm{CC}(G)$ denotes the collection of connected components of the bipartite adjacency graph G. For bookkeeping, we also define the index sets associated with each event $\mathcal{T}_q$,

$$I_q \coloneqq \{\alpha : \mathcal{L}_\alpha \in V_q\} \qquad \text{and} \qquad J_q \coloneqq \{\beta : \mathcal{E}_\beta \in W_q\}. \tag{5.9c}$$

In practice, the connected components are extracted by a breadth-first search, initialized from each unvisited Lagrangian-interface vertex and alternating between adjacent Eulerian-interface and Lagrangian-interface vertices until no new vertices are reached.

The labels of the Lagrangian and Eulerian interfaces may be permuted so that the rows and columns associated with each event appear contiguously. Specifically, the connected components of the bipartite adjacency graph are traversed sequentially, and the associated Lagrangian-interface and Eulerian-interface labels are reordered in the order they are discovered. The canonical adjacency matrix is then defined by

$$\mathcal{A} \coloneqq P_{\mathsf{lgr}}\, \widetilde{\mathcal{A}}\, P_{\mathsf{eul}}^{\top}, \tag{5.10}$$

where P_{lgr} and P_{eul} denote the row and column permutation matrices corresponding to this relabelling. With the adjacency matrix in canonical form, the event collection $\{\mathcal{T}_1, \dots, \mathcal{T}_{N_{\mathsf{event}}}\}$ is ordered so that the rows and columns associated with each event occupy contiguous index ranges in $\mathcal{A}$.

Each event $\mathcal{T}_q$ is classified according to the cardinalities of its associated index sets (I_q, J_q):

$$\mathcal{T}_q \;\text{ is }\; \begin{cases} \textit{trivial}, & \text{if } |I_q| = |J_q| = 1, \\ \textit{vanishing}, & \text{if } |I_q| = 1 \text{ and } |J_q| = 0, \\ \textit{branching}, & \text{otherwise.} \end{cases} \tag{5.11}$$

Representative examples of the different event types are illustrated in Figure 11. Topology change is detected whenever at least one event is non-*trivial*, which is equivalent to the condition

$$\exists\, \alpha \text{ such that } \sum_{\beta=1}^{N_{\mathsf{eul}}} \mathcal{A}_{\alpha\beta} \neq 1, \qquad \text{or} \qquad \exists\, \beta \text{ such that } \sum_{\alpha=1}^{N_{\mathsf{lgr}}} \mathcal{A}_{\alpha\beta} \neq 1. \tag{5.12}$$

If all events are either *trivial* or *vanishing*, then no interface surgery is required. In this case, any *vanishing* interfaces are removed, the MTS algorithm is terminated, and the Lagrangian evolution proceeds using the surviving interface family. Conversely, if at least one *branching* event is present, then the algorithm proceeds to the surgical reconstruction stage, described in the next section.

6. Interface surgery using topological defect measures

The third and final stage of the core MTS algorithm is *interface surgery*. The objective of this stage is to surgically stitch together the Lagrangian family $\{\mathcal{L}_\alpha\}_{\alpha=1}^{N_{\mathsf{lgr}}}$ and extracted Eulerian family $\{\mathcal{E}_\beta\}_{\beta=1}^{N_{\mathsf{eul}}}$, using the local event decomposition (5.9)–(5.11), to produce a surgically reconstructed post-transition interface family

$$\left\{\Gamma_\alpha(T_m^+)\right\}_{\alpha=1}^{N(T_m^+)}, \qquad \text{with} \quad N(T_m^+) \coloneqq N_{\mathsf{eul}} \quad \text{and} \quad \Gamma_\alpha(T_m^+) = \{\gamma_\alpha(s, T_m^+) : s \in \mathbb{T}\}. \tag{6.1}$$

The surgically reconstructed interface family (6.1) is subsequently passed back to the Lagrangian tracking algorithm and evolved forward until the next MTS time T_{m+1}.

For each $q = 1, \dots, N_{\mathsf{event}}$, the reconstruction procedure is performed independently on the local event $\mathcal{T}_q$ defined by the event decomposition (5.9)–(5.11). We therefore suppress the event index q throughout the remainder of this section and write

$$\mathcal{T} \equiv \mathcal{T}_q, \qquad V \equiv V_q, \qquad W \equiv W_q, \qquad E \equiv E_q, \qquad I \equiv I_q, \qquad J \equiv J_q.$$

As noted in Section 5.2, interface surgery is only required for the *branching* events, for which neither the pre-processed Lagrangian interfaces nor the extracted Eulerian interfaces are individually suitable as the post-transition interface family. The Lagrangian interfaces maintain accuracy away from the topological transition, but possess the incorrect topology. Conversely, the extracted Eulerian interfaces possess the correct topology, but generally exhibit lower accuracy away from the transition region. The key objective of interface surgery is to identify the localized regions in which topological inconsistencies occur and restrict surgical modifications to those regions alone. At a high level, the procedure consists of:

(1) constructing localized *topological defect densities* (μ, η), together with the associated *defect measure* $\mathcal{D}$, its regularized approximation $\mathcal{D}_h$, and the resulting localized *surgical region* $\mathcal{S}$, which identify the portions of the interface families responsible for topological inconsistencies;
(2) decomposing the Lagrangian and Eulerian interface families into compatible *surgical pieces* $\{\mathcal{P}, \mathcal{Q}\}$, and smoothly and consistently stitching the resulting pieces together to produce the topologically correct post-transition interface family (6.1).

In the remainder of this section, we describe this surgical reconstruction procedure in detail.

Remark 6.1 (Direct-replacement variant)**.** *Instead of performing surgical reconstruction for a* branching *event $\mathcal{T} = (V, W, E)$, one may replace the post-transition interfaces associated with this event by the extracted Eulerian interfaces in W. That is, for each $\beta \in J$, we set*

$$\Gamma_\beta(T_m^+) = \{\gamma_\beta^{\mathsf{eul}}(s) : s \in \mathbb{T}\}, \qquad \textit{together with} \quad N(T_m^+) \coloneqq N_{\mathsf{eul}}. \tag{6.2}$$

This yields a simpler direct-replacement *variant of the* MTS *algorithm, analogous to the* global *topological reconstruction algorithms of [48, 52, 35, 50, 39, 18]. As we will demonstrate below in Section 7.4.1, the direct-replacement* MTS *variant* (6.2)*, while simpler, produces nontrivial geometric errors away from topological transitions due to the global Eulerian reconstruction. The surgical approach developed in this section eliminates such errors.*

6.1. **Identifying topological defects through closest-point degeneracies.** The localized surgical regions are identified through event-local topological defect densities constructed from bidirectional closest-point projections between the pre-processed Lagrangian and extracted Eulerian interface families. Classical approaches for identifying topological inconsistencies typically rely on grid-intersection tests [19, 14, 58, 5, 23]. More closely related to the present work are geometric approaches based on closest-point degeneracies and local interface signatures, including the kink-detection framework of [24] and the signature method of [9]. The defect densities introduced below may be viewed as a closest-point degeneracy detector adapted to the event-local Lagrangian–Eulerian correspondence structure constructed in Section 5.

6.1.1. *Topological defect densities.* For each *branching* event $\mathcal{T}$, we define binary defect densities

$$\mu_\alpha : \mathbb{T} \to \{0, 1\}, \quad \alpha \in I, \qquad \text{and} \qquad \eta_\beta : \mathbb{T} \to \{0, 1\}, \quad \beta \in J, \tag{6.3}$$

where $\mu_\alpha(s)$ and $\eta_\beta(s)$ indicate whether the corresponding interface points $\ell_\alpha(s)$ and $e_\beta(s)$ are identified as topologically defective. The "Lagrangian" defect density μ_α is constructed from a pair of closest-point degeneracy indicators associated with the extracted Eulerian interface family. The "Eulerian" defect density η_β is defined analogously by reversing the roles of the Lagrangian and Eulerian interface families in the construction below.

We first introduce the closest-label map and closest-point projection associated with the extracted Eulerian interface family:

$$\Lambda_\alpha(s) \coloneqq \arg\min_{\beta \in J} \inf_{\bar{s} \in \mathbb{T}} |\ell_\alpha(s) - e_\beta(\bar{s})|, \tag{6.4a}$$

$$\Pi_\alpha(s) \coloneqq \arg\min_{z \in \mathcal{E}} |\ell_\alpha(s) - z|. \tag{6.4b}$$

Here (6.4b) should be understood in the sense that $\Pi_\alpha(s)$ denotes a selected closest point, since the minimizer need not be unique. The defect density is then defined as the union of two binary indicator functions,

$$\mu_\alpha(s) = \max\{\mu_\alpha^1(s), \mu_\alpha^2(s)\}, \tag{6.5}$$

where the individual indicators $\mu_\alpha^1, \mu_\alpha^2 : \mathbb{T} \to \{0,1\}$ are defined as follows:

(1) The *label-jump indicator* μ_α^1 marks neighborhoods of discontinuities in the closest-label map Λ_α. More precisely, denoting the jump set of Λ_α by

$$\mathcal{J} \coloneqq \{s \in \mathbb{T} : \Lambda_\alpha \text{ is discontinuous at } s\}, \tag{6.6a}$$

we define

$$\mu_\alpha^1(s) = \mathbb{1}_{\{|\ell_\alpha(s) - \ell_\alpha(s_*)| \le h \,:\, s_* \in \mathcal{J}\}}, \tag{6.6b}$$

where $\mathbb{1}_A$ denotes the indicator function on the set A. Discontinuities in the closest-label map indicate locations where nearby points on the same Lagrangian interface are associated with different Eulerian interfaces, signaling a breakdown of the discrete correspondence structure near *branching* events.

(2) The *projection-distortion indicator* μ_α^2 marks points where the closest-point projection from the Lagrangian interface family onto the Eulerian interface family exhibits large local expansion along the interface. For each $s \in \mathbb{T}$, let $\mathcal{E}_{\beta(s)}$ denote the Eulerian interface selected by the closest-label map Λ_α, and let $\bar{s}(s) \in \mathbb{T}$ denote a parameter value satisfying

$$\Pi_\alpha(s) = e_{\beta(s)}\big(\bar{s}(s)\big). \tag{6.7a}$$

The projected arclength parameter $\sigma(s)$ along the Eulerian interface $\mathcal{E}_{\beta(s)}$ is then given by

$$\sigma(s) = \int_0^{\bar{s}(s)} \left| \frac{\mathrm{d}}{\mathrm{d}r} e_{\beta(s)}(r) \right| \mathrm{d}r. \tag{6.7b}$$

The local projection-distortion factor is then defined by

$$\rho_\alpha(s) \coloneqq \left| \frac{\mathrm{d}\sigma}{\mathrm{d}s}(s) \right|, \tag{6.7c}$$

and the projection-distortion indicator by

$$\mu_\alpha^2(s) = \mathbb{1}_{\{\rho_\alpha(s) > \rho_{\max}\}}, \qquad \rho_{\max} = 10. \tag{6.7d}$$

When the Lagrangian and Eulerian interface families are locally well-aligned, the closest-point projection behaves approximately like an arclength-preserving reparametrization, so that $\rho_\alpha \approx 1$. Large values of ρ_α therefore indicate strong local distortion of the closest-point structure along the interface.

The indicators $\{\mu_\alpha^1, \eta_\beta^1\}$ and $\{\mu_\alpha^2, \eta_\beta^2\}$ capture complementary failure modes of the lgr-eul correspondence structure. The label-jump indicators $\{\mu_\alpha^1, \eta_\beta^1\}$ detect discrete changes in the associated dual-family interface label, but are insensitive to geometric distortion within a single dual-family correspondence. Conversely, the projection-distortion indicators $\{\mu_\alpha^2, \eta_\beta^2\}$ detect strong local stretching of the closest-point projection even when the associated dual-family interface label remains unchanged.

To define the topological defect densities (μ, η), the one-sided defect densities (6.3) are propagated through their closest-point projections onto the dual interface family, thereby symmetrizing the defect construction between the Lagrangian and Eulerian interface families. Introducing the disjoint unions $\mathcal{L} \coloneqq \bigsqcup_{\alpha \in I} \mathcal{L}_\alpha$ and $\mathcal{E} \coloneqq \bigsqcup_{\beta \in J} \mathcal{E}_\beta$, we define the defect densities $\mu : \mathcal{L} \to \{0,1\}$ and $\eta : \mathcal{E} \to \{0,1\}$ by

$$\mu(\ell_\alpha(s)) = \max\left\{\mu_\alpha(s),\, \eta_\beta(\bar{s}) : \Pi_\alpha(s) = e_\beta(\bar{s}),\, \beta \in J\right\}, \qquad \alpha \in I, \tag{6.8a}$$

and

$$\eta(e_\beta(s)) = \max\left\{\eta_\beta(s),\, \mu_\alpha(\bar{s}) : \Pi_\beta(s) = \ell_\alpha(\bar{s}),\, \alpha \in I\right\}, \qquad \beta \in J, \tag{6.8b}$$

respectively.

6.1.2. *Defect measures and the surgical region.* The interface-supported defect densities (μ, η) induce an associated defect measure

$$\mathcal{D} \in \mathcal{M}(\mathbb{R}^2), \tag{6.9a}$$

where $\mathcal{M}(\mathbb{R}^2)$ denotes the space of finite Radon measures on $\mathbb{R}^2$. The measure $\mathcal{D}$ is characterized by its pairing with smooth compactly supported test functions $\varphi \in C_c(\mathbb{R}^2)$:

$$\langle \mathcal{D}, \varphi \rangle \;=\; \sum_{\alpha \in I} \int_{\mathbb{T}} \mu(\ell_\alpha(s))\, \varphi(\ell_\alpha(s))\, |\ell'_\alpha(s)|\, \mathrm{d}s \;+\; \sum_{\beta \in J} \int_{\mathbb{T}} \eta(e_\beta(s))\, \varphi(e_\beta(s))\, |e'_\beta(s)|\, \mathrm{d}s. \tag{6.9b}$$

In the numerical algorithm, the singular defect measure $\mathcal{D}$ is replaced by the h-scale regularization

$$\mathcal{D}_h \coloneqq \psi_h * \mathcal{D}, \tag{6.10a}$$

where $\psi_h : \mathbb{R}^2 \to [0, \infty)$ is the compactly supported cosine mollifier

$$\psi_h(x) = \begin{cases} \frac{1}{2}\left(1 + \cos\left(\frac{\pi |x|}{h}\right)\right), & |x| < h, \\ 0, & |x| \geq h. \end{cases} \tag{6.10b}$$

The regularized defect measure $\mathcal{D}_h$ provides an Eulerian representation of the defective portions of the Lagrangian and Eulerian interface families.

The associated *surgical region* is then defined as the super-level set

$$\mathcal{S} \coloneqq \{x \in \mathbb{R}^2 : \mathcal{D}_h(x) > \tau\}, \tag{6.11}$$

where $\tau > 0$ is a prescribed threshold. In the numerical examples presented below, we use $\tau = 0.1$. The surgical region localizes the portion of the computational domain requiring topological reconstruction, while leaving the remainder of the interface family unchanged.

The construction of the defect densities, defect measures, and surgical region is illustrated for a simple *merge* event in Figure 12. The left panel displays the Lagrangian and Eulerian interfaces, while the center panel shows the interface-supported defect densities (μ, η) and the singular defect measure $\mathcal{D}$ that they induce. The right panel shows the (regularized) Eulerian defect measure $\mathcal{D}_h$, with the associated defect "hotspot" identifying the surgical region $\mathcal{S}$ used in the subsequent reconstruction.

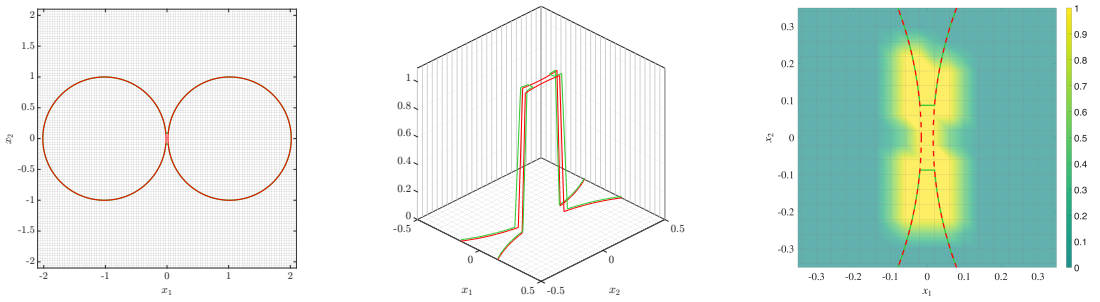

(A) Interfaces $\mathcal{L}_\alpha$ and $\mathcal{E}_\beta$ (B) Defect densities (μ, η) (C) Regularized defect measure $\mathcal{D}_h$

FIGURE 12. Construction of the topological defect densities, defect measures, and surgical region for a representative *merge* event. **Left:** Pre-processed Lagrangian interfaces (red) and extracted Eulerian interfaces (green). **Center:** Interface-supported defect densities (μ, η) defined by the one-sided defect indicators (6.6)–(6.7) and the symmetrized projection construction (6.8), shown in a zoomed neighborhood of the *merge*. **Right:** Regularized defect measure $\mathcal{D}_h$ defined by the mollification (6.10), shown in a zoomed neighborhood of the *merge*. The localized defect "hotspot" identifies the surgical region $\mathcal{S}$.

6.2. **Stitching surgical pieces into reconstructed interfaces.** In this subsection, we describe how the surgical region $\mathcal{S}$ computed in the previous subsection is used to decompose the interfaces into localized *surgical pieces*, which are subsequently stitched together using a graph-theoretic reconstruction algorithm to form the post-transition interface family. Surgical treatments of topological change have appeared in a variety of front-tracking methods [14, 58, 5, 23]. The distinguishing feature of the present approach is that the localization is driven by the defect measure $\mathcal{D}_h$, rather than by grid-intersection tests [14, 58, 5, 23], yielding an event-local surgical region adapted to the geometry of the topological inconsistency.

The surgical decomposition treats the two interface families differently. The retained Lagrangian pieces are the connected components of the Lagrangian family *outside* the surgical region, while the retained Eulerian pieces are the connected components of the Eulerian family *inside* the surgical region:

$$\mathcal{P} \coloneqq \{p_i\}_{i=1}^{\mathcal{N}} \coloneqq \mathrm{Conn}\left(\mathcal{L} \cap \mathcal{S}^c\right), \qquad \mathcal{N} \coloneqq \#\mathrm{Conn}\left(\mathcal{L} \cap \mathcal{S}^c\right), \tag{6.12a}$$

$$\mathcal{Q} \coloneqq \{q_j\}_{j=1}^{\mathcal{M}} \coloneqq \mathrm{Conn}\left(\mathcal{E} \cap \mathcal{S}\right), \qquad \mathcal{M} \coloneqq \#\mathrm{Conn}\left(\mathcal{E} \cap \mathcal{S}\right). \tag{6.12b}$$

6.2.1. *Graph-theoretic formulation of surgical reconnection.* Each surgical piece is an open curve segment with two endpoints, so that the reconstruction problem may be reformulated entirely in terms of endpoint connectivity. Here and below, if p is an open curve segment, then ∂p denotes the set consisting of its two endpoints. We denote the collections of Lagrangian and Eulerian endpoints by

$$\mathcal{V} \coloneqq \{v_i\}_{i=1}^{2\mathcal{N}}, \qquad v_{2i-1}, v_{2i} \in \partial p_i, \qquad i = 1, \dots, \mathcal{N}, \tag{6.13a}$$

$$\mathcal{W} \coloneqq \{w_j\}_{j=1}^{2\mathcal{M}}, \qquad w_{2j-1}, w_{2j} \in \partial q_j, \qquad j = 1, \dots, \mathcal{M}. \tag{6.13b}$$

The complete endpoint set is then given by

$$\widehat{V} \coloneqq \mathcal{V} \cup \mathcal{W}. \tag{6.13c}$$

The connectivity already present within the surgical pieces is encoded by the *intra-piece edge set*

$$E_{\mathrm{intra}} \coloneqq \{(v_{2i-1}, v_{2i})\}_{i=1}^{\mathcal{N}} \cup \{(w_{2j-1}, w_{2j})\}_{j=1}^{\mathcal{M}}. \tag{6.14a}$$

Each edge in E_{intra} connects the two endpoints of a single surgical piece. The missing connectivity is supplied by an *inter-piece edge set*

$$E_{\mathrm{inter}} \subset \mathcal{V} \times \mathcal{W}, \tag{6.14b}$$

which connect Lagrangian endpoints to Eulerian endpoints. Thus, the surgical reconstruction problem reduces to determining the edge set E_{inter}. The construction of E_{inter} is governed by a collection of local geometric admissibility criteria, which are described in the next subsection. These criteria are designed so that every endpoint in $\widehat{V}$ is incident to exactly one inter-piece edge. Consequently, E_{inter} defines a perfect matching between the endpoint sets $\mathcal{V}$ and $\mathcal{W}$.

The complete *interface surgery graph* is then defined by

$$\widehat{G} \coloneqq (\widehat{V}, \widehat{E}), \qquad \widehat{E} \coloneqq E_{\mathrm{intra}} \cup E_{\mathrm{inter}}. \tag{6.15}$$

By construction, every vertex of $\widehat{G}$ is incident to exactly one intra-piece edge and exactly one inter-piece edge, so that $\widehat{G}$ is a 2-regular graph. It follows that $\widehat{G}$ admits the decomposition

$$\widehat{G} = C_1 \sqcup \cdots \sqcup C_K, \tag{6.16}$$

where each C_k is a simple cycle. The cycles $\{C_k\}_{k=1}^{K}$ define a collection of closed reconstructed interfaces, yielding the post-transition interface family (6.1).

The graph-theoretic formulation above naturally leads to a global combinatorial reconstruction problem, in which one seeks a perfect matching satisfying additional global constraints, such as a prescribed number of reconstructed interfaces. Rather than solving this global matching problem directly, the present implementation of the MTS algorithm constructs the inter-piece edge set E_{inter} using a greedy cycle-tracing procedure based on local geometric admissibility criteria.

6.2.2. *Greedy construction of inter-piece connectivity.* Starting from an Eulerian surgical piece, admissible Lagrangian and Eulerian pieces are appended alternately to a partially reconstructed chain. Each selected continuation determines an inter-piece edge in E_{inter}, and the tracing procedure continues until the chain closes to form a cycle. The resulting cycle defines a reconstructed interface, after which the procedure is repeated until all surgical pieces have been incorporated into reconstructed interfaces.

The reconstruction may be viewed as an inductive continuation process. Given a partially reconstructed chain and its current terminal piece p, the next step consists of selecting a surgical piece q that provides a geometrically compatible continuation of the chain. For an oriented surgical piece p, we denote its exit endpoint and outgoing unit tangent vector by $x_{\mathrm{ext}}(p)$ and $\tau_{\mathrm{ext}}(p)$, respectively. Similarly, for a candidate continuation q, we denote its entry endpoint by $x_{\mathrm{ent}}(q)$. The endpoint separation between p and q is

$$r(p, q) \coloneqq \left| x_{\mathrm{ent}}(q) - x_{\mathrm{ext}}(p) \right|, \tag{6.17a}$$

while the directional alignment is measured by

$$a(p,q) \coloneqq \frac{(x_{\mathrm{ent}}(q) - x_{\mathrm{ext}}(p)) \cdot \tau_{\mathrm{ext}}(p)}{|x_{\mathrm{ent}}(q) - x_{\mathrm{ext}}(p)|}. \tag{6.17b}$$

The next piece in the reconstruction is chosen by minimizing the *continuation functional*

$$q^* = \arg\min_q \{\mathcal{C}(p,q) : r(p,q) \le h\}, \qquad \mathcal{C}(p,q) \coloneqq r(p,q)^2 + \lambda\big(1 - a(p,q)\big), \qquad \lambda \coloneqq (4h)^2. \tag{6.17c}$$

The locality constraint $r(p,q) \le h$ excludes nonlocal candidates, and the continuation functional balances endpoint proximity and tangent continuity across the proposed connection.

Each application of (6.17) determines a new inter-piece edge in E_{inter} and extends the partially reconstructed chain. The continuation process is repeated until the evolving chain returns to its initial surgical piece, thereby forming a closed cycle. Once a cycle has been completed, its constituent surgical pieces are removed from further consideration and the tracing procedure is restarted from another unused Eulerian piece. Repeating this process produces a collection of reconstructed cycles, which define the post-transition interface family (6.1). The complete cycle-tracing procedure used in the numerical implementation is summarized in Algorithm 6 in Section A.

6.2.3. *Smoothing of surgically reconstructed interfaces.* Because the extracted Eulerian interface segments are obtained through a grid-based contour extraction procedure, the surgically reconstructed interfaces generally inherit locally faceted geometric artifacts. To improve the geometric quality of the reconstructed interfaces, we apply a smoothing procedure to all extracted interface segments.

For a closed extracted loop $z = \{z_i\}_{i=1}^N$, we introduce the smoothing functional

$$\mathcal{J}_{\mathrm{sm}}(\widehat{z}; z) = w_{\mathsf{fit}} \sum_{i=1}^N |\widehat{z}_i - z_i|^2 + w_{\mathsf{sm}} \sum_{i=1}^N |\widehat{z}_{i-1} - 2\widehat{z}_i + \widehat{z}_{i+1}|^2. \tag{6.18a}$$

The first term penalizes deviation from the extracted geometry, while the second penalizes oscillations through a discrete second-difference regularization. The smoothed loop $\widetilde{z} = \{\widetilde{z}_i\}_{i=1}^N$ is defined by

$$\widetilde{z} = \arg\min_{\widehat{z}} \mathcal{J}_{\mathrm{sm}}(\widehat{z}; z). \tag{6.18b}$$

The minimizer is obtained by solving the corresponding periodic linear system for the two coordinate components of $\widetilde{z}$. To compensate for the small area loss introduced by the smoothing operation, the resulting curve is subsequently corrected by a small normal displacement chosen to recover the original enclosed area.

For extracted subchains appearing within reconstructed interfaces, we use the same smoothing functional together with an additional tangent-matching penalty. Let $z_{i_1}, \dots, z_{i_2}$ denote an extracted subchain of a reconstructed interface, with neighboring retained Lagrangian points z_{i_1-1} and z_{i_2+1} held fixed. We define

$$\mathcal{J}_{\tan}(\widehat{z}) = w_{\mathsf{tan}}\Big(|\widehat{z}_{i_1} - (z_{i_1-1} + \tau_L)|^2 + |\widehat{z}_{i_2} - (z_{i_2+1} - \tau_R)|^2\Big), \tag{6.18c}$$

where τ_L and τ_R denote the incoming and outgoing tangent vectors supplied by the neighboring retained Lagrangian segments. The extracted subchain is then replaced by the minimizer

$$\widetilde{z} = \arg\min_{\widehat{z}}\Big\{\mathcal{J}_{\mathrm{sm}}(\widehat{z}; z) + \mathcal{J}_{\tan}(\widehat{z})\Big\}. \tag{6.18d}$$

The additional term weakly enforces tangent continuity across the reconstructed connection. The minimizer is again obtained by solving the corresponding linear system for the extracted subchain.

In all numerical experiments, we use $w_{\mathsf{fit}} = 10^{-5}$, $w_{\mathsf{sm}} = h^2$, and $w_{\mathsf{tan}} = 1$. The complete smoothing procedure is summarized in Algorithm 7 in Section A.

6.3. **Diagnostic continuation through topological transitions.** The reconstruction procedure described above determines the post-transition interface family (6.1), which is subsequently evolved by the Lagrangian solver. Associated with the evolving interface are the tangent FTLE diagnostic and the Lagrangian observation windows introduced in Sections 2.3 and 2.4, respectively. Because interface surgery replaces portions of the pre-transition Lagrangian interface by surgically reconstructed geometry, additional bookkeeping is required to propagate these diagnostics through topological transitions.

6.3.1. *Closest-point projection of tangent field data.* The tangent FTLE diagnostic (2.9) depends on both the tangent field $\xi_\alpha(s,t)$ and the reference quantity $\xi_\alpha(s,0)$, which are propagated in the numerical method as auxiliary Lagrangian state variables. At a topological transition, interface surgery creates a new post-transition interface family, so this state must also be transferred to the reconstructed interfaces. This is analogous to the adaptive refinement and coarsening procedure, where tangent field data are transferred by interpolation. The key difference is that, after surgery, interpolation along a single interface is no longer available. Instead, the transfer is performed through a closest-point projection onto the pre-transition Lagrangian interface family.

For each reconstructed interface point $\gamma_\alpha(s,T_m^+)$, we define

$$\Pi_\alpha^*(s) := \underset{z\in\bigcup\Gamma_\beta(T_m^-)}{\arg\min} \left|\gamma_\alpha(s,T_m^+)-z\right|. \tag{6.19}$$

Suppose that $\Pi_\alpha^*(s_i)$ lies on the pre-transition segment joining $\gamma_\beta(s_j,T_m^-)$ and $\gamma_\beta(s_{j+1},T_m^-)$, so that

$$\Pi_\alpha^*(s_i) = (1-\theta)\gamma_\beta(s_j,T_m^-) + \theta\gamma_\beta(s_{j+1},T_m^-), \qquad 0\le\theta\le 1. \tag{6.20}$$

We then transfer the auxiliary tangent state by linear interpolation:

$$\xi_\alpha(s_i,T_m^+) = (1-\theta)\,\xi_\beta(s_j,T_m^-) + \theta\,\xi_\beta(s_{j+1},T_m^-), \tag{6.21a}$$

$$|\xi_\alpha(s_i,0)| = (1-\theta)\,|\xi_\beta(s_j,0)| + \theta\,|\xi_\beta(s_{j+1},0)|. \tag{6.21b}$$

The post-transition tangent stretch factor and tangent FTLE are then evaluated from (2.9).

6.3.2. *Defect measure correction of observation windows.* The observation windows introduced in Section 2.4 are attached to Lagrangian marker trajectories and therefore remain focused on the same material region during a purely Lagrangian evolution. At a topological transition, however, the associated filamentary structures may undergo break-up with mass loss, causing the window centers to drift away from the regions of interest. We therefore correct the observation windows using the regularized defect measure $\mathcal{D}_h$, recentering each window according to the local defect distribution and enlarging it when necessary to fully contain the defect region.

Let $\mathcal{W}_j(T_m^-)$ denote an observation window immediately before a topological transition. If the defect measure vanishes within $\mathcal{W}_j(T_m^-)$, the original center and half-width are retained: $c_j(T_m^+)=c_j(T_m^-)$ and $w_j(T_m^+)=w_j(T_m^-)$. Otherwise, starting from the pre-transition window center $c_j(T_m^-)$, we iteratively update

$$c_j^{(r+1)} = \frac{\int_{\mathcal{W}_j^{(r)}} x\,\mathcal{D}_h(x)\,dx}{\int_{\mathcal{W}_j^{(r)}} \mathcal{D}_h(x)\,dx}, \tag{6.22}$$

where $\mathcal{W}_j^{(r)}$ denotes the observation window centered at $c_j^{(r)}$ and $c_j^{(0)}=c_j(T_m^-)$. The iteration terminates once the change in the window center falls below a prescribed tolerance, and the final iterate is taken as $c_j(T_m^+)$. After recentering, the window half-width $w_j(T_m^+)$ is increased, if necessary, until the support of $\mathcal{D}_h$ inside the corrected window no longer intersects a thin boundary strip of $\mathcal{W}_j(T_m^+)$.

7. Numerical examples

7.1. **Code implementation and computational platform.** The MTS algorithm is implemented in modern Fortran using double-precision arithmetic and OpenMP parallelization, while MATLAB is used for post-processing and visualization. All numerical experiments were performed on a MacBook Pro equipped with an M1 Pro processor (10 CPU cores) and 32 GB of memory, using 10 OpenMP threads for all reported timings. All simulations use the default parameter values listed in Table 1.

The code is organized around three principal data structures: the Lagrangian interface family, the sparse Eulerian level-set representation, and the topology-processing machinery. The Lagrangian interfaces are stored as closed parametric curves, while the Eulerian representation is stored using sparse locally refined level-set blocks restricted to a narrow neighborhood of the interface. Topological transitions are managed through an event-local topology structure that mirrors the mathematical framework developed in Sections 5 and 6. At each MTS time T_m, this structure stores the pre-processed Lagrangian interface family $\{\mathcal{L}_\alpha\}_{\alpha=1}^{N_{\text{lgr}}}$, the extracted Eulerian interface family $\{\mathcal{E}_\beta\}_{\beta=1}^{N_{\text{eul}}}$, the canonical adjacency matrix $\mathcal{A}$, and the event decomposition $\{\mathcal{T}_1,\dots,\mathcal{T}_{N_{\text{event}}}\}$. Each event stores the associated defect measures, surgical piece families $\mathcal{P}$ and $\mathcal{Q}$, and the reconstructed interfaces, allowing topological transitions to be processed independently and locally.

7.2. **Satellite-interface dynamics in the rotating-vortex benchmark.** We first apply the MTS algorithm to the rotating-vortex benchmark introduced in Section 3.1. The velocity field u, initial interface $\gamma_\alpha(s,0)$, final time t_{max}, time-step Δt, and coarse computational scale h_0 are the same as in (3.1)–(3.3). The fine-scale resolution is given by the dyadic refinement sequence $h = 2^{-p}h_0$, for $p = 1,\dots,5$. Topological processing is performed throughout the filament-formation phase at the MTS times

$$T_m = 0.2\,m, \qquad m = 1,\dots,20, \tag{7.1}$$

and terminating at the time of maximal deformation $t = 4$.

The MTS solutions computed with the coarsest resolution $h = 2\times10^{-2}$ are displayed in Figure 13 at a representative collection of MTS times for which topological transitions occur. In each subfigure, the left panel displays the topologically processed interface family (blue), together with a reference solution (black) computed using the classical Lagrangian tracking algorithm with the finest resolution $h = 1.25\times10^{-3}$. Also shown is a heatmap of the regularized defect measure $\mathcal{D}_h(x,t)$ defined by (6.10). The bright localized hotspots correspond to topological defects and determine the associated surgical region $\mathcal{S}$ through (6.11). The right panel displays the adjacency graph associated with the corresponding topological event. Red vertices represent the pre-processed Lagrangian interfaces, green vertices represent the extracted Eulerian interfaces, and edges indicate the adjacency relations identified by the topology extraction procedure.

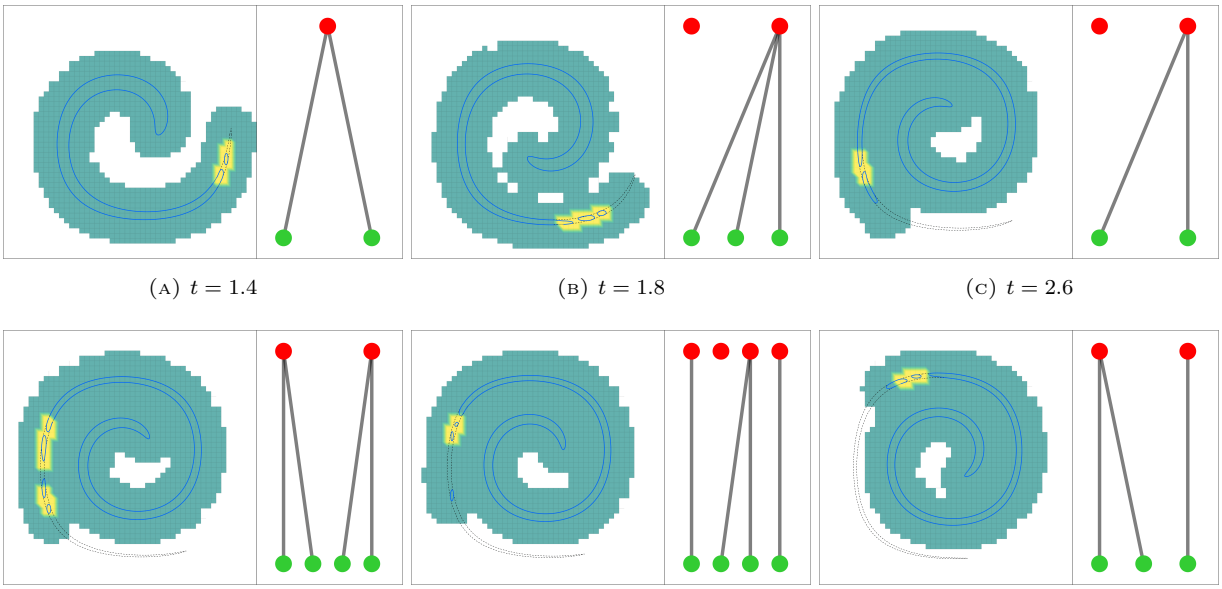

(A) $t = 1.4$ (B) $t = 1.8$ (C) $t = 2.6$

(D) $t = 2.8$ (E) $t = 3.0$ (F) $t = 3.8$

FIGURE 13. Representative topological transitions for the rotating-vortex benchmark computed using the MTS algorithm with $h = 2\times10^{-2}$. The left panel in each subfigure displays the MTS solution (blue), the reference solution computed using classical Lagrangian tracking with $h = 1.25\times10^{-3}$ (black), and the regularized defect measure $\mathcal{D}_h(x,t)$. The right panel displays the corresponding adjacency graph, with red vertices denoting pre-processed Lagrangian interfaces, green vertices denoting extracted Eulerian interfaces, and edges denoting adjacency relations between the two interface families. The sequence illustrates repeated *split* and *vanishing* events generated by the strongly filamenting tip of the interface.

The topological evolution is driven by the strongly filamenting tip identified in Section 3.1 by the pronounced trough of the tangent FTLE near $s = \pi/2$ on the initial interface. As the filament tip undergoes progressive stretching and compression, it repeatedly pinches off to form small satellite interfaces, producing a sequence of one-to-many *split* events. The resulting satellite interfaces are subsequently stretched and sheared by the flow until their characteristic length scales fall below the grid scale h, triggering *vanishing* events. Qualitatively similar sequences of *split* and *vanishing* events have been reported for VOF-based and LCRM methods [49, 50, 9, 25, 39]. Figure 13 illustrates this repeated cycle of satellite-interface formation and disappearance throughout the filament-formation phase. Meanwhile, away from the strongly filamenting

tip, the MTS solution is indistinguishable from the reference solution, confirming that the topological processing remains localized to the surgical region and does not introduce spurious distortions elsewhere along the interface. This contrasts with VOF-based methods and LCRM, where the interface geometry may be degraded globally by Eulerian advection and reconstruction errors [49, 50, 39].

7.2.1. *Resolution dependence and convergence.* The first panel of Figure 14 displays the MTS solution computed with $h = 0.02$ at the final time $t_{\mathsf{max}} = 8$, when the reversible flow returns the interface to its initial configuration. The dominant error is the mass loss associated with the strongly filamenting tip. As the fine-scale h is decreased (Figures 14(b) to 14(d)), progressively smaller filamentary structures are resolved by the underlying Lagrangian representation. Consequently, fewer *split* and *vanishing* events are triggered, leading to a corresponding reduction in mass loss. In the finest simulation $h = 1.25 \times 10^{-3}$, all dynamically relevant length scales remain resolved throughout the evolution and no topological events are detected. Thus, the fine-scale parameter h provides direct control over the degree of topological processing, with the MTS algorithm reducing to classical Lagrangian tracking in the limit that all filamentary scales are resolved.

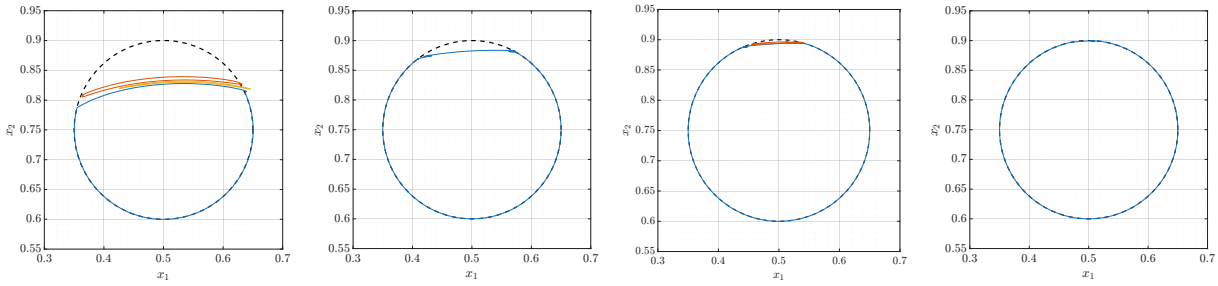

(A) $h = 2 \times 10^{-2}$ (B) $h = 1 \times 10^{-2}$ (C) $h = 5 \times 10^{-3}$ (D) $h = 2.5 \times 10^{-3}$

FIGURE 14. MTS solutions for the rotating-vortex benchmark at $t_{\mathsf{max}} = 8$ for decreasing values of the fine-scale parameter h. The colored curves denote the MTS interface family, while the black curve denotes the reference solution computed using classical Lagrangian tracking with $h = 1.25 \times 10^{-3}$. As h decreases, progressively smaller filamentary structures are resolved, resulting in fewer split and vanishing events and correspondingly less mass loss.

The reduction in mass loss observed in Figure 14 is confirmed quantitatively by the results in Table 2. Meanwhile, the runtime statistics show that the cost of the MTS algorithm remains comparable to that of the underlying Lagrangian tracking algorithm, accounting for roughly 20–70% of the total runtime over the resolutions considered. Since resolving progressively smaller filamentary structures reduces the frequency of topological events and the associated surgery operations, the relative cost of the MTS algorithm decreases as h is reduced. For this problem, the dominant contribution to the MTS overhead is the Eulerian extraction stage, which typically accounts for roughly 50–80% of the MTS runtime. By contrast, adjacency-topology construction contributes only a few percent of the MTS cost and is therefore negligible. The surgery stage accounts for approximately 15–45% of the MTS runtime at coarse and intermediate resolutions where repeated topological transitions occur, but its relative cost decreases as the fine scale h is reduced, ultimately vanishing at the finest resolution where no topological events occur.

While direct comparison is complicated by differing error metrics,[5] the results compare favorably with those reported in Table 1 of [30] and Table 2 of [25], which exhibit larger errors and substantially larger runtimes at comparable effective resolutions. Although such comparisons should be interpreted with caution, the combination of the quantitative results and the qualitative comparisons presented here strongly suggests that the localized, event-driven nature of the MTS algorithm enables substantially higher accuracy at significantly lower computational cost than the MOF filament-aware interface-capturing approaches [30, 25].

7.2.2. *Tangent FTLE through topological transitions.* Figure 15 displays the tangent FTLE diagnostic obtained through the projection (6.19)–(6.21). For visualization, the tangent FTLE is plotted directly over the computed interface family in physical space.[6] These results should be contrasted with the classical

[5]The errors reported in [30, 25] are Eulerian volume-fraction errors, whereas Table 2 reports the numerical reversal error $|A_K - A_0|$.

[6]Because topological transitions alter the structure of the interface family, the tangent FTLE no longer admits a natural global parameter-space representation. Plotting the diagnostic directly on the interface geometry avoids this ambiguity.

TABLE 2. Accuracy and runtime statistics for solutions to the rotating-vortex benchmark computed using the Lagrangian tracking + MTS topology-processing algorithm. The table reports the numerical reversal error $|A_K - A_0|$, together with wall-clock runtimes for the Lagrangian tracking component, the core MTS algorithm, and the overall computation.

h	2×10^{-2}	1×10^{-2}	5×10^{-3}	2.5×10^{-3}	1.25×10^{-3}
$\lvert A_K - A_0 \rvert$	1.35×10^{-2}	1.83×10^{-3}	2.70×10^{-4}	2.00×10^{-5}	1.92×10^{-8}
Order	–	2.88	2.76	3.76	10.02
LGR runtime (s)	8.00×10^{-2}	3.38×10^{-1}	1.75	5.73	7.86
Order	–	2.08	2.37	1.71	0.46
MTS runtime (s)	1.86×10^{-1}	2.84×10^{-1}	8.31×10^{-1}	1.35	2.72
Order	–	0.61	1.55	0.70	1.01
Total runtime (s)	2.66×10^{-1}	6.22×10^{-1}	2.58	7.07	10.6
Order	–	1.23	2.05	1.45	0.58

Lagrangian computation shown in Figure 5(b), where the tangent FTLE exhibits two localized troughs corresponding to the strong and weak filamenting tips. The trough associated with the weakly filamenting tip remains essentially unchanged in the MTS simulations. By contrast, the highly localized trough associated with the strongly filamenting tip becomes progressively attenuated as the interface is propagated through successive split and vanishing events. This attenuation reflects the removal of fine filamentary scales by the topological processing. As the fine-scale h is decreased, a smaller range of filamentary structures is affected by surgery, and the attenuation correspondingly weakens. In the limit that all dynamically relevant scales are resolved, the MTS tangent FTLE converges to the classical Lagrangian diagnostic.

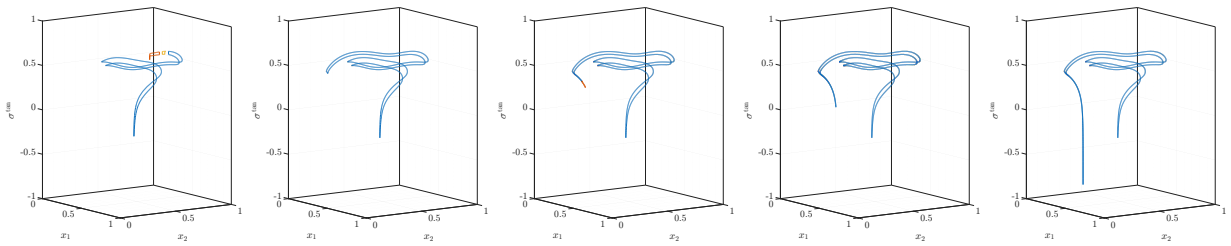

(A) $h = 2 \times 10^{-2}$ (B) $h = 1 \times 10^{-2}$ (C) $h = 5 \times 10^{-3}$ (D) $h = 2.5 \times 10^{-3}$ (E) $h = 1.25 \times 10^{-3}$

FIGURE 15. Tangent FTLE $\sigma^{\tan}(s,t)$ for the MTS solutions of the rotating-vortex benchmark at the time of maximal deformation $t = 4$ for decreasing values of the fine-scale parameter h. The diagnostic is visualized directly on the computed interface family. As h decreases, the trough associated with the strongly filamenting tip becomes increasingly pronounced, approaching the classical Lagrangian diagnostic shown in Figure 5(b), while the trough associated with the weakly filamenting tip remains essentially unchanged.

The geometric consequences of the topological processing may be understood through the stretch–curvature relation (2.11). Figure 16 displays the corresponding phase plot in a neighborhood of the strongly filamenting tip. Since the $\kappa^{-1/3}$ branch is generated by the filament tip itself, removal of filamentary structure below the prescribed microscale h by the MTS algorithm produces a corresponding truncation of the branch. At coarse resolutions, only a short segment of the branch remains.As h is decreased, less of the filament tip is removed by the topological processing, and the branch extends toward the classical Lagrangian result. The MTS phase plots, particularly at coarse resolutions, are somewhat noisy away from the principal $\kappa^{-1/3}$ branch. This behavior reflects the sensitivity of curvature, a second-derivative quantity, to the small geometric errors introduced in the surgical regions, where the interface is reconstructed by stitching together Lagrangian and Eulerian interface segments. By contrast, the tangent FTLE remains smooth, as shown in Figure 15, confirming its robustness as a diagnostic of filamentation through topological change.

7.3. **The $\mathcal{S}$-flow benchmark.** The second example is the $\mathcal{S}$-flow benchmark, originally introduced in [1] and subsequently studied in [30, 25, 26]. The prescribed incompressible velocity field u is defined by

$$u(x_1, x_2) = \tfrac{1}{4}\left((4x_1 - 2) + (4x_2 - 2)^3,\ -(4x_2 - 2) - (4x_1 - 2)^3\right)^\top, \tag{7.2}$$

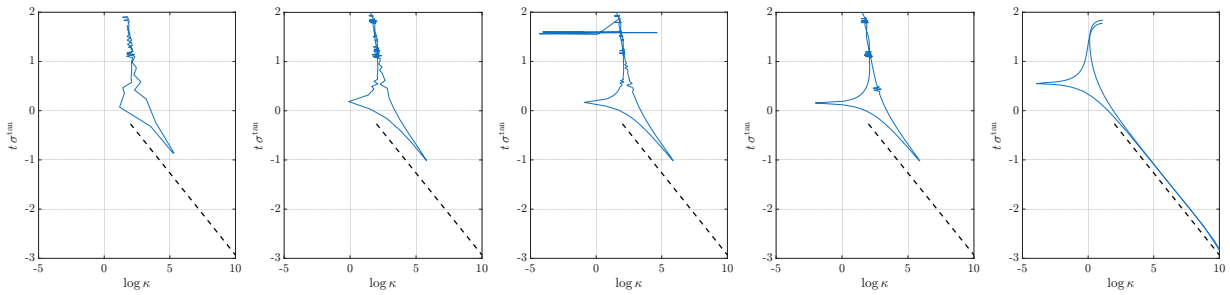

(A) $h = 2 \times 10^{-2}$ (B) $h = 1 \times 10^{-2}$ (C) $h = 5 \times 10^{-3}$ (D) $h = 2.5 \times 10^{-3}$ (E) $h = 1.25 \times 10^{-3}$

FIGURE 16. Stretch–curvature phase plots near the strongly filamenting tip for the h-refined MTS solutions to the rotating-vortex benchmark. The $\kappa^{-1/3}$ branch provides a geometric signature of the filament tip. As the fine-scale h is decreased, a larger portion of the branch is recovered.

and the initial interface is a circle of radius 0.25 centered at $(0.5, 0.5)$. The velocity gradient required for the tangent-FTLE computation (2.10a) is

$$Du(x_1, x_2) = \begin{pmatrix} 1 & 3(4x_2 - 2)^2 \\ -3(4x_1 - 2)^2 & -1 \end{pmatrix}. \tag{7.3}$$

The solution is evolved to the final time $t_{\mathsf{max}} = 3$. During the evolution, the initially circular interface is deformed into a characteristic S-shaped configuration containing thin filamentary regions and sharp geometric features.

We apply the MTS algorithm using the spatial resolutions $h = 0.02$ and $h = 0.01$, with corresponding time steps $\Delta t = 0.01$ and $\Delta t = 0.005$. Topological processing is performed at the MTS times

$$T_m = 0.1\, m, \quad m = 1, \ldots, 30.$$

The MTS solutions are displayed in Figure 17. At the coarser resolution, several satellite-interface formation events are observed in the strongly filamenting regions of the flow. Notably, the filament-breakup process develops symmetrically near the two terminal filament tips, reflecting the corresponding symmetry in the tangent-FTLE field discussed below. As the resolution is increased, these pinch-off events occur at progressively smaller scales, and the computed interface converges qualitatively toward the reference solution shown in Figure 17(f).

The tangent FTLE computed by classical Lagrangian tracking is displayed in Figure 18(a). Consistent with the symmetric filament-breakup dynamics observed in Figure 17, the diagnostic exhibits paired trough structures localized near the two terminal filament tips. Comparison with the tangent-FTLE fields for the rotating-vortex and nonlinear alternating-shear benchmarks shown in Figures 5(b) and 8(b) demonstrates that the $\mathcal{S}$-flow dynamics occupy an intermediate regime of multiscale filamentation complexity.

A consistent qualitative relationship between filamentation and the tangent FTLE is observed: localized troughs in the reference tangent-FTLE field characterize the filamenting regions where breakup occurs in the corresponding MTS computations. The MTS algorithm continues the tangent-FTLE diagnostic through topological transitions by transferring the tangent variation field between the pre- and post-surgery interfaces using the closest-point projection. As the resolution is increased, the reconstructed tangent-FTLE fields shown in Figures 18(b) and 18(c) converge qualitatively toward the reference diagnostic computed by classical Lagrangian tracking, shown in Figure 18(a).

7.4. **Microscale filament breakup by nonlinear alternating-shearing.** We now assess the efficacy of the MTS algorithm on the more challenging nonlinear alternating-shear test introduced in Section 3.2. The velocity field u, initial interface $\gamma_\alpha(s, 0)$, final time t_{max}, time-step Δt, and coarse computational scale h_0 are identical to those used in Section 3.2. The fine-scale resolution is given by the dyadic refinement sequence

$$h = 2^{-p} h_0, \qquad p = 1, \ldots, 5, \tag{7.4}$$

and topological processing is performed throughout the filament-formation phase at the MTS times

$$T_m = m, \qquad m = 1, \ldots, 15. \tag{7.5}$$

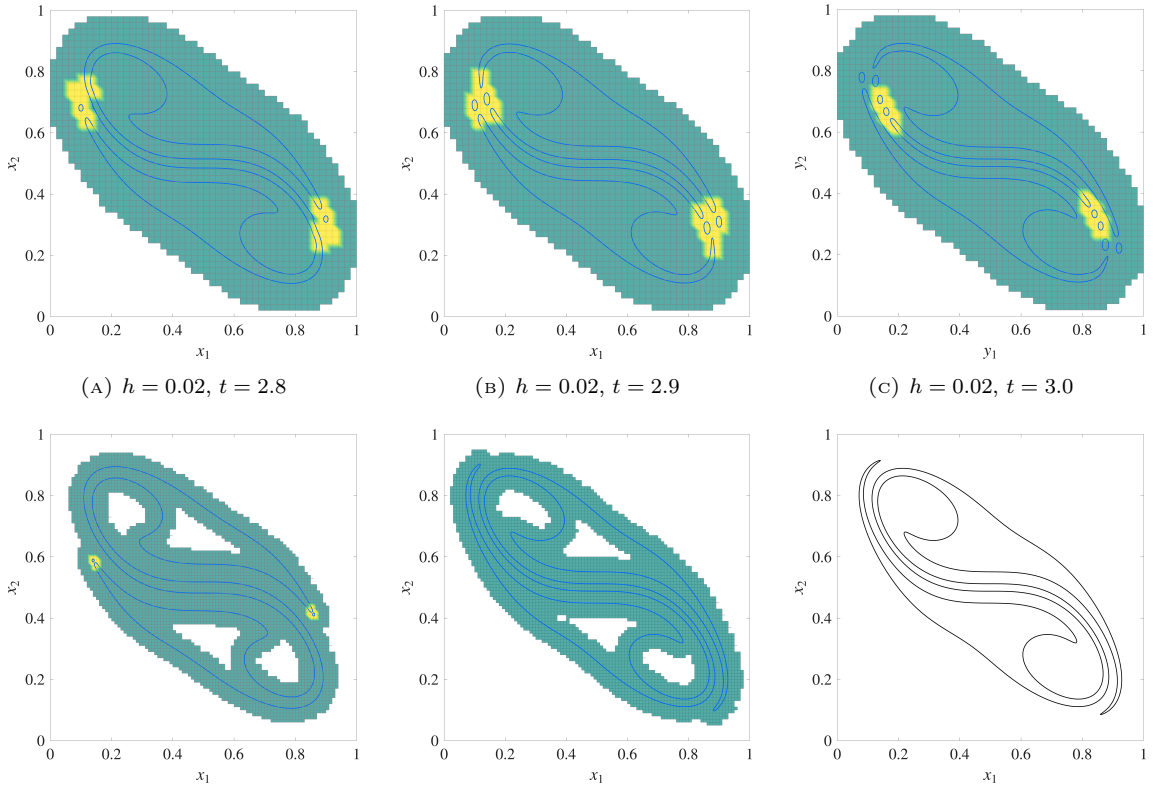

(A) $h = 0.02$, $t = 2.8$ (B) $h = 0.02$, $t = 2.9$ (C) $h = 0.02$, $t = 3.0$

(D) $h = 0.01$, $t = 2.6$ (E) $h = 0.01$, $t = 3.0$ (F) reference $t = 3.0$

FIGURE 17. $\mathcal{S}$-flow benchmark computed using the MTS algorithm. The top row shows the solution with $h = 0.02$ at times $t = 2.8$, 2.9, and 3.0. The bottom row shows the solution with $h = 0.01$ at times $t = 2.6$ and 3.0, together with a reference solution at $t = 3.0$. Satellite-interface formation events observed in the coarser computation are confined to progressively smaller scales as the resolution is increased.

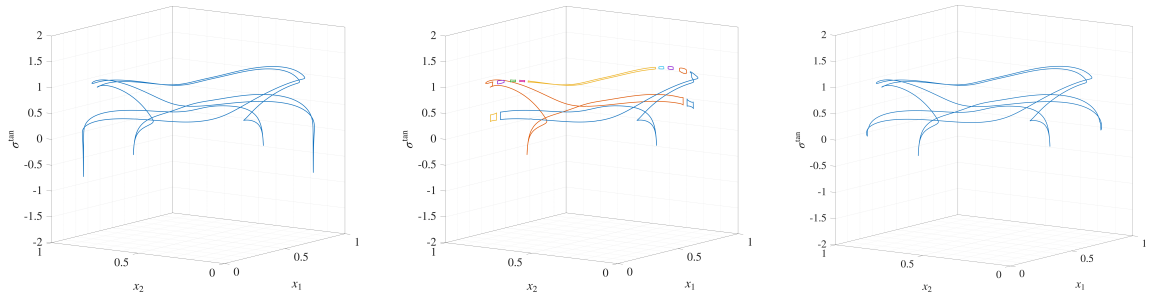

(A) reference (B) $h = 0.02$ (C) $h = 0.01$

FIGURE 18. Tangent FTLE diagnostics for the $\mathcal{S}$-flow benchmark. The left panel shows the reference tangent-FTLE field computed using classical Lagrangian tracking, while the center and right panels show the corresponding tangent-FTLE fields computed using the MTS algorithm with $h = 0.02$ and $h = 0.01$, respectively. The MTS algorithm continues the tangent-FTLE diagnostic through topological transitions by transferring the tangent variation field between the pre- and post-surgery interfaces using the closest-point projection. As the resolution is increased, the reconstructed tangent-FTLE field converges qualitatively toward the reference diagnostic.

As demonstrated in Section 3.2, the repeated alternating-shear deformation generates multiscale filamentary structures, with breakup occurring near material locations identified by localized troughs in the tangent FTLE (Figure 8(b)). The resulting sequence of repeated one-to-many satellite-formation events provides a stringent test of the robustness and scalability of the MTS topology-processing algorithm.

The MTS interface evolution is shown in Figure 18 for the microscale-resolving case $h/L = 1.25 \times 10^{-3}$, where $L = 6$. Since no topological events are detected for $t < 10$, only the times $t = 10, \ldots, 15$ are displayed. The left panels show the evolving MTS interface representation together with the localized defect measure and surgical region, while the right panels show the corresponding adjacency graphs. As anticipated by the tangent-FTLE analysis of Section 3.2, filament breakup occurs near the filament tips identified by the FTLE troughs. The most severe breakup occurs within the $\mathcal{W}_1$ and $\mathcal{W}_3$ observation windows, in agreement with the qualitative conclusions of Figure 8.

Conversely, the $\mathcal{W}_2$ and $\mathcal{W}_4$ observation windows associated with the remaining FTLE troughs identified in Figure 8(b) exhibit filament-tip pinch-off events with satellites whose characteristic size falls below the prescribed sub-microscale resolution (parameters N_{min}, L_{min}, and A_{min} in Table 1) and are therefore filtered during the Eulerian extraction phase; see the $\mathcal{W}_4$, $\mathcal{W}_2$, and $\mathcal{W}_4$ observation windows in Figure 18(b), Figure 18(d), and Figure 18(e), respectively. Nevertheless, the defect measure $\mathcal{D}_h$ identifies the pinch-off location on the parent filament, and the interface surgery smoothly reconstructs the filament tip. This behavior may be viewed as a weak form of geometric regularization acting below the prescribed microscale resolution, in which unresolved satellites are removed while the larger-scale filament geometry is preserved.

The repeated generation, disappearance, and interaction of satellite interfaces produces a rich sequence of topological events, with a maximum of 26 interfaces generated at $t = 14$. Throughout this evolution, the MTS algorithm robustly reconstructs the interface family through numerous one-to-many *splits* and *vanishings*, together with a few *merges*.

7.4.1. *The need for surgical reconstruction.* We now use the reversal-to-identity property (3.8) to compare the surgical MTS algorithm with the simpler direct-replacement variant (6.2). The final interfaces at $t_{\mathsf{max}} = 30$ computed using the two approaches are shown in Figure 19 for the microscale resolving case $h/L = 1.25 \times 10^{-3}$. In the surgical solution (Figure 19(a)), the satellite interfaces generated during the filament-breakup phase are mapped back to the material locations associated with the localized tangent-FTLE troughs, and the interface is close to indistinguishable from the reference solution away from these regions. By contrast, the direct-replacement solution (Figure 19(b)) exhibits larger geometric errors, reflecting the repeated discarding of accurately tracked Lagrangian geometry through global Eulerian reconstruction. The final column of Table 3 confirms quantitatively that the direct-replacement variant produces significantly larger errors at the same resolution.

7.4.2. *Convergence and scalability.* The qualitative convergence of the MTS algorithm is illustrated in Figure 20, which compares the final interfaces at $t_{\mathsf{max}} = 30$ for the dyadic refinement sequence $h = 2^{-p}h_0$. As h is refined, the recovered interface qualitatively converges toward the exact solution. At the coarser resolutions, the accumulated effect of unresolved satellite disappearances produces visible mass loss, and portions of the reconstructed interface are no longer contained within the initial configuration. As the resolution is refined, the MTS solution becomes nearly indistinguishable from the reference solution. Topological transitions continue to occur, but they become progressively more localized and are confined to sub-microscale structures.

Quantitative accuracy and runtime statistics are reported in Table 3. We first consider the numerical reversal error $|A_K - A_0|$. Although the error decreases rapidly under refinement, the convergence is not monotone. In particular, the error increases between the two coarsest resolutions. This behavior reflects the competing influence of two distinct error mechanisms. On the one hand, unresolved satellite disappearances introduce mass loss and therefore decrease the enclosed area. On the other hand, geometric reconstruction errors may locally expand portions of the interface and increase the enclosed area. At the coarsest resolutions these effects partially cancel, making the area error alone an imperfect measure of geometric accuracy. A more informative diagnostic is provided by the symmetric-difference error [30] defined by

$$E_{\mathrm{sym}} = |\Omega_K \triangle \Omega_0|\,, \qquad A \triangle B = (A \setminus B) \cup (B \setminus A), \tag{7.6}$$

where Ω_K and Ω_0 denote the regions enclosed by the final and initial interfaces, respectively, and $A \triangle B$ denotes the symmetric difference of two sets. Unlike the area-based reversal error, E_{sym} measures the total geometric discrepancy between the two enclosed regions and therefore does not permit cancellation between mass-loss and over-expansion errors. Consistent with the qualitative behavior observed in Figure 20, the symmetric-difference error decreases more uniformly under refinement, with an observed convergence rate of approximately three.

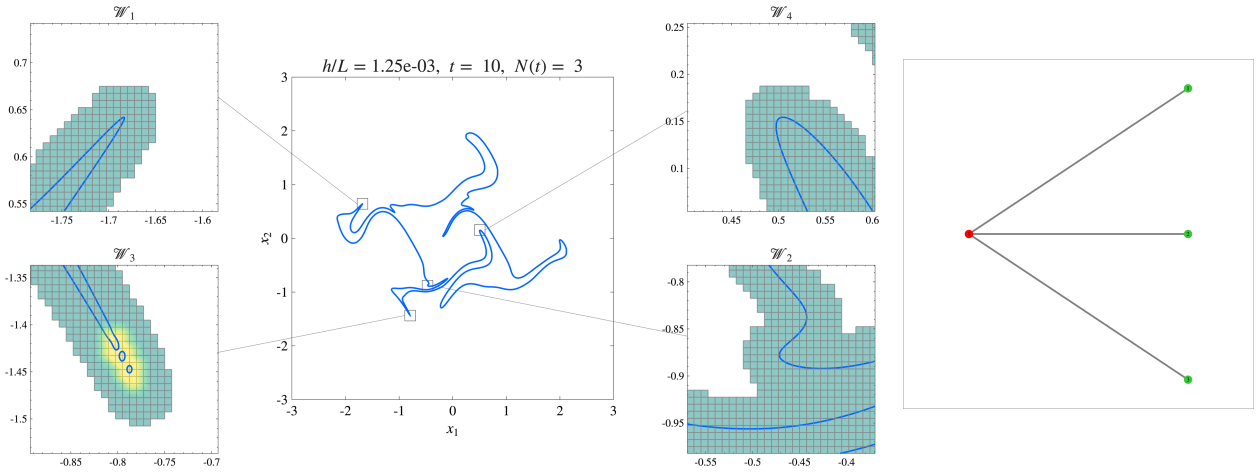

(A) $t = 10$

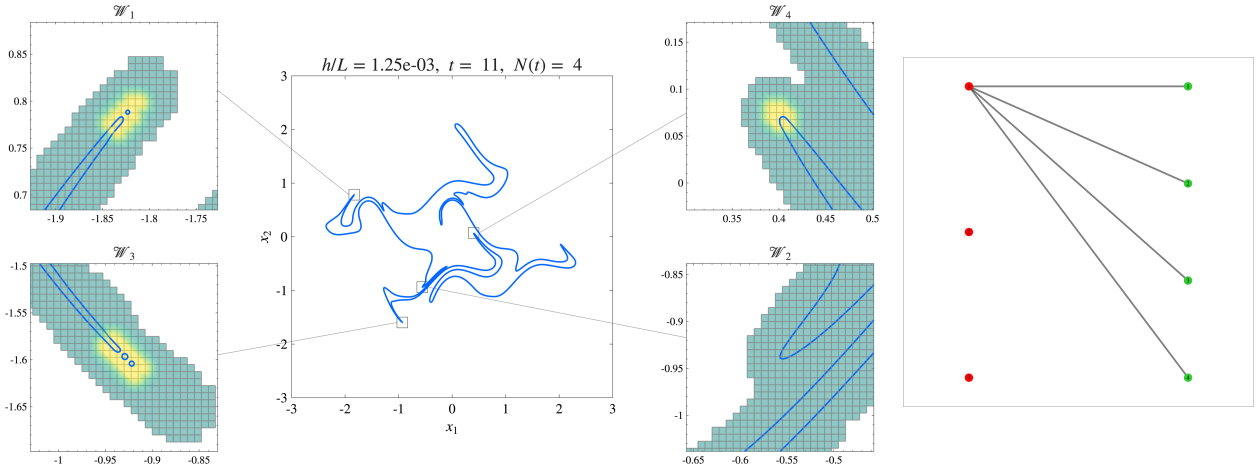

(B) $t = 11$

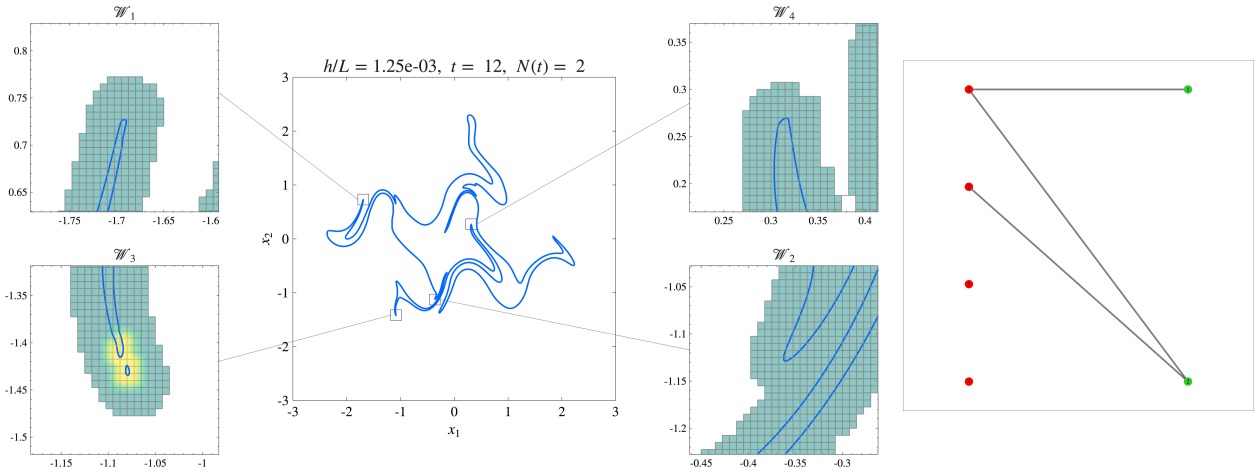

(C) $t = 12$

FIGURE 18. Topology processing for the alternating-shear test at the microscale resolving resolution $h/L = 1.25 \times 10^{-3}$. The panels show the sequence of detected topological transitions during the filament-breakup phase $t = 10, \ldots, 15$. In each row, the left panel displays the MTS interface representation together with the localized defect measure used to identify the surgical region, while the right panel displays the corresponding adjacency graph. The evolving interface family is robustly reconstructed by the MTS algorithm through the resulting sequence of *splits* and *merges*. A video of the complete evolution is available at [44].

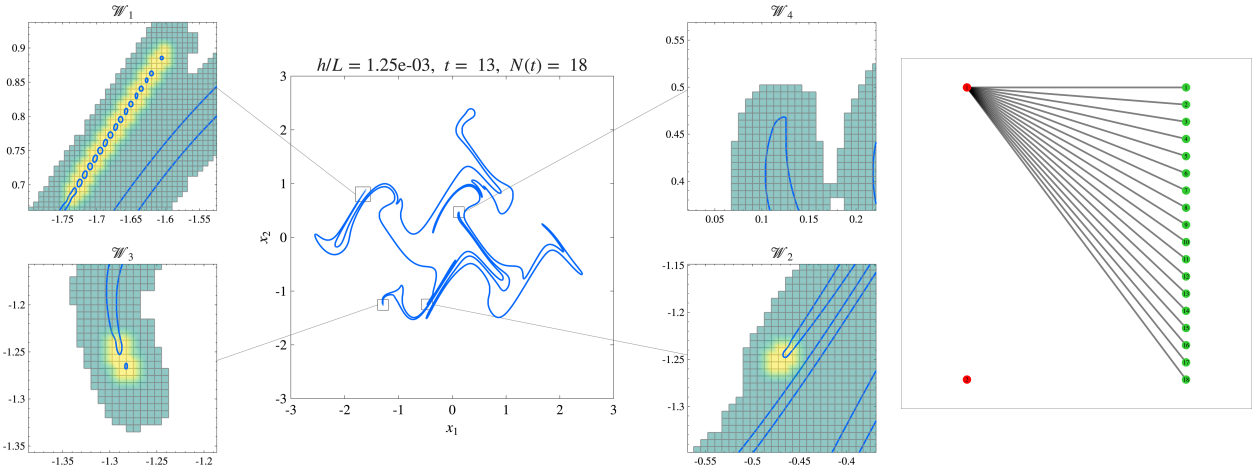

(D) $t = 13$

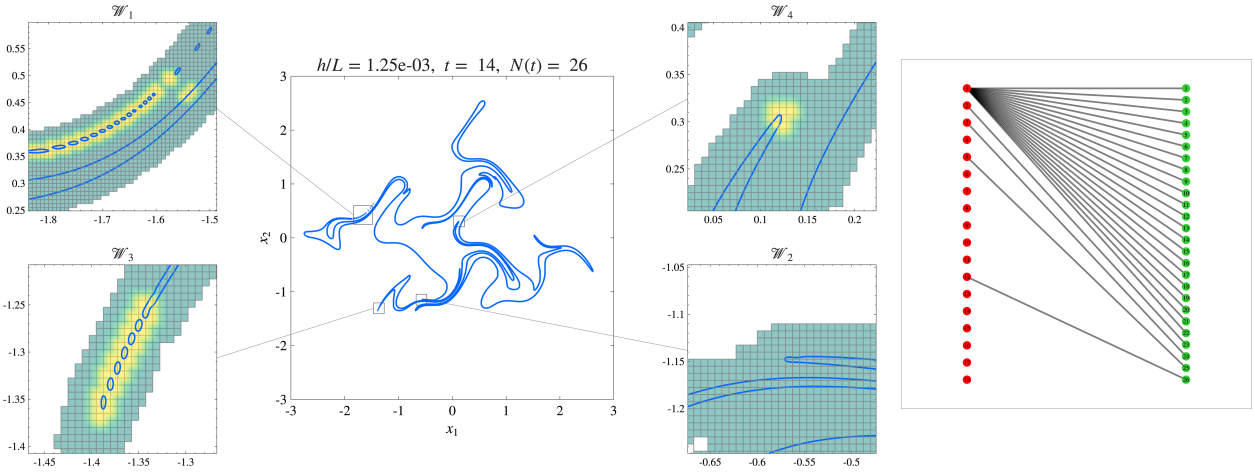

(E) $t = 14$

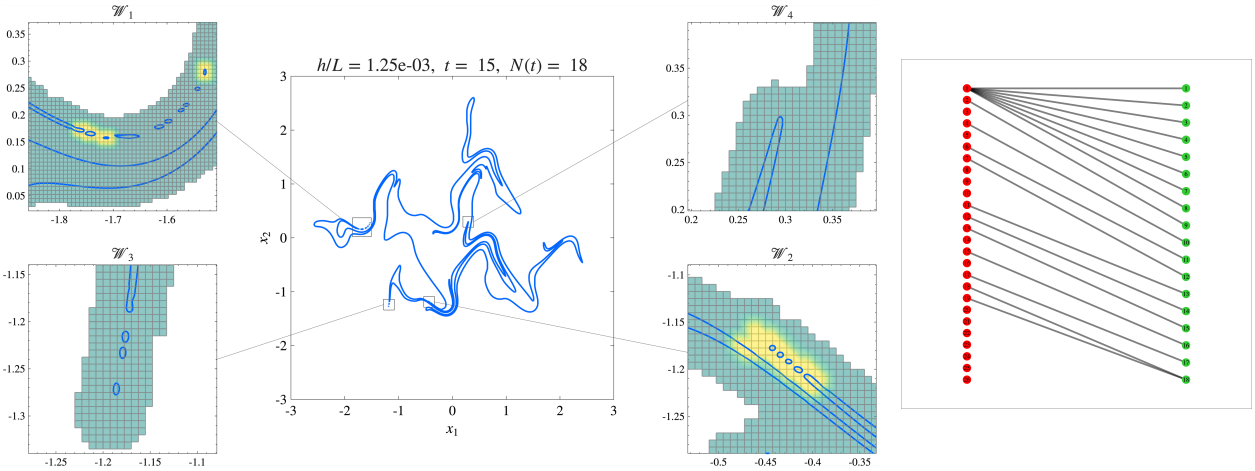

(F) $t = 15$

FIGURE 18. Continued from previous page.

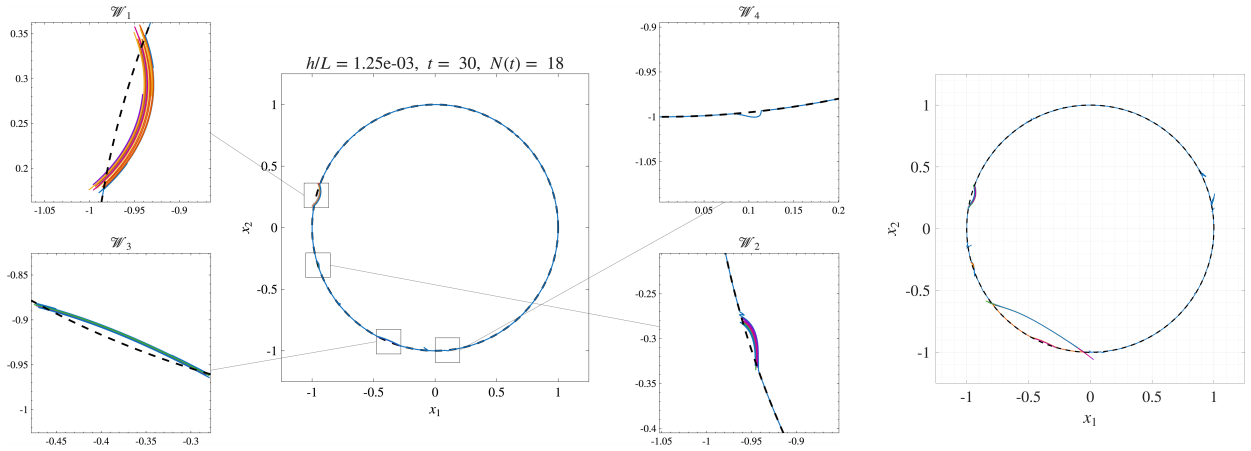

(A) MTS solution (B) direct-replacement solution

FIGURE 19. Comparison of the surgical MTS algorithm and the direct-replacement variant (6.2) for the nonlinear alternating-shear test with microscale resolution $h/L = 1.25 \times 10^{-3}$ at the final time $t_{\mathsf{max}} = 30$. The left panel displays the surgical MTS solution, while the right panel displays the direct-replacement solution. Repeated global Eulerian reconstruction produces nontrivial geometric errors in the latter.

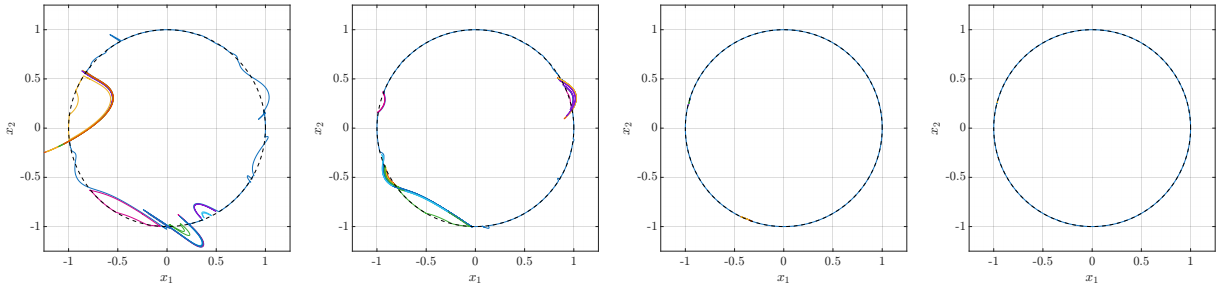

(A) $h/L = 5 \times 10^{-3}$ (B) $h/L = 2.5 \times 10^{-3}$ (C) $h/L = 6.25 \times 10^{-4}$ (D) $h/L = 3.125 \times 10^{-4}$

FIGURE 20. Qualitative convergence of the MTS algorithm for the nonlinear alternating-shear test. The panels compare the final interfaces at $t_{\mathsf{max}} = 30$ for the dyadic refinement sequence $h = 2^{-p}h_0$. The reference solution is displayed in black.

The runtime statistics in Table 3 show that both the Lagrangian tracking and MTS topology-processing components scale approximately as $\mathcal{O}(h^{-2})$. Despite the rich sequence of *splits*, *vanishings*, and *merges* encountered during the filament-breakup phase, the topology-processing stage accounts for only about 25% of the overall computational cost.

7.4.3. *Statistical description of filament breakup.* There are several motivations for studying microscale filamentation dynamics from a statistical perspective.

(1) *Mathematically*, many sharp-interface evolution problems become ill-posed through the generation of progressively finer scales [11, 10, 53]. This naturally motivates the consideration of statistical solutions, in which the interface evolution is described in terms of an ensemble of admissible realizations rather than a single deterministic trajectory [13, 31].
(2) From a *physical* perspective, the formation of arbitrarily fine filamentary structures signals the breakdown of the idealized sharp-interface description, which is subsequently resolved by the MTS algorithm as filament breakup. Similar fragmentation processes arise in ligament breakup and spray atomization, where the resulting droplet population is commonly characterized through its size distribution [57]. An additional physical interpretation comes from chaotic-advection studies in which tracer structures below the Batchelor scale are removed by diffusion and the resulting tracer microstructure is characterized statistically [41, 42]. Here, we employ an analogous strategy, replacing

TABLE 3. Accuracy and runtime statistics for solutions to the nonlinear alternating-shear test computed using the Lagrangian tracking + MTS topology-processing algorithm. The table reports the numerical reversal error $|A_K - A_0|$, the symmetric-difference error E_{sym}, and wall-clock runtimes for the Lagrangian tracking component, the MTS topology-processing component, and the overall computation. The final column reports the corresponding direct-replacement solution computed at $h/L = 1.25 \times 10^{-3}$, obtained by replacing the Lagrangian interface family with the extracted Eulerian interface family at each MTS time.

h/L	5×10^{-3}	2.5×10^{-3}	1.25×10^{-3}	6.25×10^{-4}	3.125×10^{-4}	1.25×10^{-3} *direct-replacement*
$\lvert A_K - A_0 \rvert$	6.92×10^{-3}	1.71×10^{-2}	4.32×10^{-3}	4.76×10^{-4}	7.52×10^{-5}	6.16×10^{-3}
Order	–	-1.30	1.98	3.18	2.66	
E_{sym}	1.63×10^{-1}	4.77×10^{-2}	5.34×10^{-3}	5.92×10^{-4}	7.92×10^{-5}	9.95×10^{-3}
Order	–	1.77	3.16	3.17	2.90	
LGR runtime (s)	4.01	2.04×10^{1}	7.34×10^{1}	2.91×10^{2}	1.11×10^{3}	6.85×10^{1}
Order	–	2.35	1.85	1.99	1.93	
MTS runtime (s)	1.58	6.60	2.51×10^{1}	1.00×10^{2}	3.73×10^{2}	5.93
Order	–	2.06	1.93	2.00	1.90	
Total runtime (s)	5.59	2.70×10^{1}	9.85×10^{1}	3.92×10^{2}	1.48×10^{3}	7.45×10^{1}
Order	–	2.27	1.87	1.99	1.92	

the diffusive regularization by MTS and evaluating the persistence of filament-breakup events through ensemble statistics.

(3) The *computational efficiency* of the MTS algorithm makes it feasible to generate large ensembles of microscale-resolving interface simulations.

To this end, we construct an ensemble of 50 realizations of the nonlinear alternating-shear test at the microscale resolution $h/L = 1.25 \times 10^{-3}$. The initial interface is fixed as the unit circle, while the alternating-shear map is perturbed through pseudo-random variations of the phase parameters.[7] We construct two sets of ensembles: a Lagrangian ensemble $\mathbf{\Sigma}\,\mathsf{LGR}_h$ and an MTS ensemble $\mathbf{\Sigma}\,\mathsf{MTS}_h$ generated by the Lagrangian (LGR) tracking and MTS algorithms, respectively. The complete 50-member MTS ensemble required approximately 24 minutes of wall-clock time, of which approximately 20% was spent on topology processing.

The first twenty members of each ensemble at the time of maximal deformation, $t = 15$, are shown in Figure 21. The large-scale geometry of the interface remains consistent across the ensemble, and the principal effect of the ensemble averaging is a coarse-graining of the microscale filamentary structures. In particular, the ensemble members occupy a finite envelope whose width may be interpreted as a statistical "thickening" of the underlying sharp interface. Within the observation windows $\mathcal{W}_1$, $\mathcal{W}_2$, and $\mathcal{W}_4$, the uncertainty envelope exceeds the characteristic filament thickness, causing the corresponding filament-breakup processes to be effectively suppressed by the coarse-graining. In the strongest filamenting window $\mathcal{W}_3$, however, the filament-breakup process survives the uncertainty-induced coarse-graining, and remains *statistically persistent*.

To quantify the breakup process, we next consider statistics of the interfaces generated within the ensemble. The satellite-count distribution shown in Figure 22(a) is relatively broad, indicating that the precise number of breakup fragments remains sensitive to microscale variations in the filamentation process. Consequently, individual realizations often exhibit substantially different topological outcomes. Nevertheless, the rank-ordered area statistics shown in Figures 22(b) and 22(c) reveal a much more coherent picture. For each realization, the interface areas are rank ordered and normalized by the total enclosed area. The resulting area spectrum exhibits a clear separation between the primary interface and the population of satellite droplets, whose normalized areas span several orders of magnitude, including scales well below the prescribed microscale resolution. Moreover, the smooth median spectrum and relatively narrow interquartile range indicate that the breakup process generates a consistent hierarchy of satellite sizes across the ensemble. Similar broad size hierarchies arise in ligament-fragmentation and spray-atomization processes, where a dominant parent structure produces a distributed population of progressively smaller fragments [57]. The ability to capture this scale separation highlights a key feature of the MTS framework: topological resolution is controlled by the prescribed scale h, while geometric information is retained at significantly smaller scales.

[7] For each ensemble index k and each map index m, the phase shifts (3.5d) are perturbed according to $\phi_m \mapsto \phi_m + \varepsilon a_{k,m}$ and $\psi_m \mapsto \psi_m + \varepsilon b_{k,m}$, where $\varepsilon = 0.2$ and $a_{k,m}, b_{k,m} \in [-1, 1]$ are pseudo-random phase perturbations.

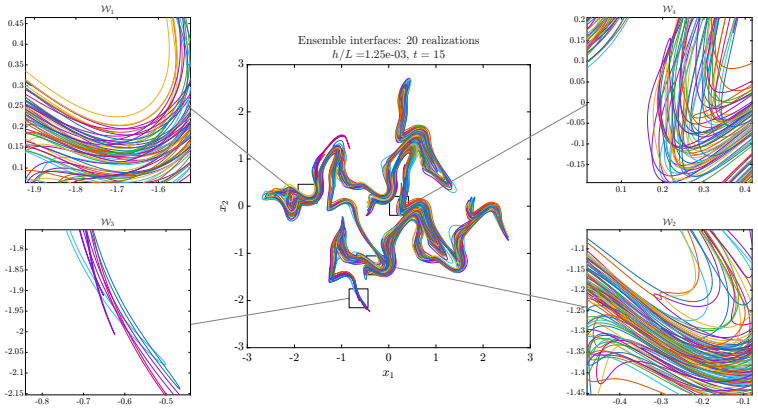

(A) $\mathbf{\Sigma}\mathsf{LGR}_h$ ensemble

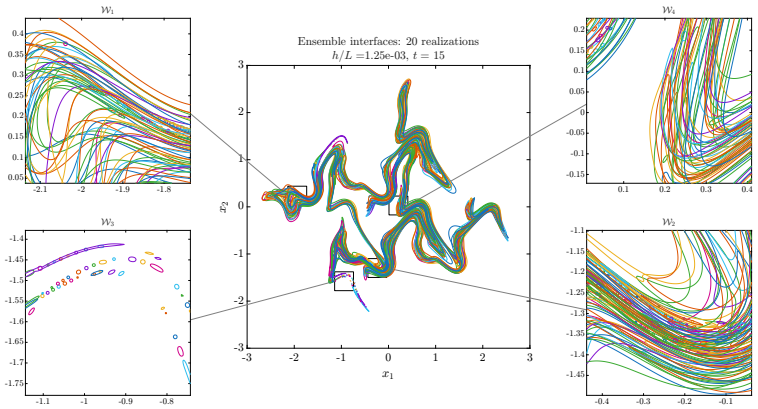

(B) $\mathbf{\Sigma}\mathsf{MTS}_h$ ensemble

FIGURE 21. First twenty realizations of the pseudo-random alternating-shear ensembles at the time of maximal deformation, $t = 15$, computed with microscale resolution $h/L = 1.25 \times 10^{-3}$. A video of the simulation is available at [44]. The large-scale interface geometry remains consistent across the ensemble, while the ensemble spread coarse-grains the filamentary structures into a statistically thickened interface. Within the observation windows $\mathcal{W}_1$, $\mathcal{W}_2$, and $\mathcal{W}_4$, the uncertainty envelope exceeds the characteristic filament thickness, causing the corresponding filament-breakup processes to be suppressed. By contrast, the breakup process within the strongest filamenting window $\mathcal{W}_3$ survives the uncertainty-induced coarse-graining and remains *statistically persistent*.

To visualize the coarse-graining induced by the ensemble averaging, we convert each realization into an Eulerian phase-field $\chi(x,t)$, defined as a regularized indicator function of the enclosed region:

$$\chi(x,t) = \begin{cases} 1, & \phi(x,t) \le -4h, \\ 0, & \phi(x,t) \ge 4h, \\ \frac{1}{2}\left(1 - \frac{\phi}{4h} - \frac{1}{\pi}\sin\left(\pi\frac{\phi}{4h}\right)\right), & |\phi(x,t)| < 4h, \end{cases} \tag{7.7a}$$

where $\phi(x,t)$ denotes the signed-distance function. Thus, $\chi = 1$ inside the interface, $\chi = 0$ outside, and transitions smoothly across a narrow band of width $8h$ surrounding the interface. The ensemble-averaged phase field is then defined by

$$\bar{\chi}(x,t) = \frac{1}{50}\sum_{k=1}^{50} \chi_k(x,t), \tag{7.7b}$$

where χ_k denotes the phase field associated with the k-th realization. The quantity $\bar{\chi}(x,t)$ may be interpreted as the fraction of realizations for which the point x lies inside the enclosed region.

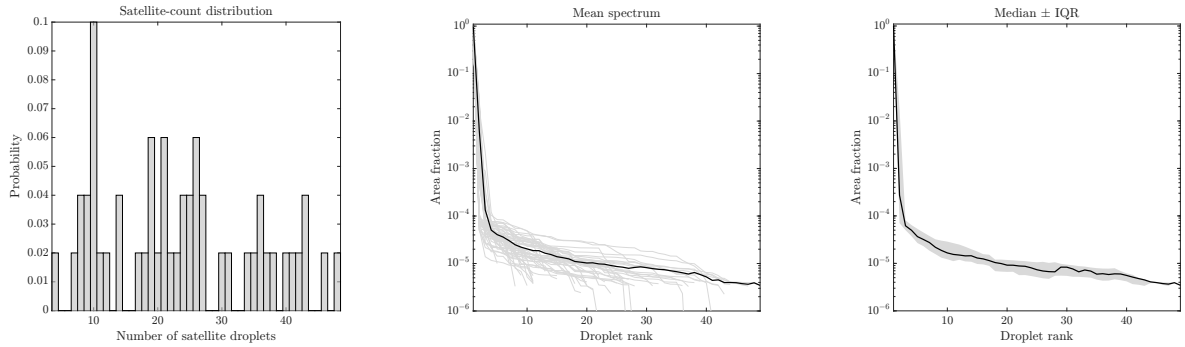

(A) (B) (C)

FIGURE 22. Droplet statistics for the pseudo-random alternating-shear ensemble at $t = 15$ and microscale resolution $h/L = 1.25 \times 10^{-3}$. **Left:** Probability distribution of the number of satellite droplets generated in each realization. **Center:** Rank-ordered area spectrum showing the normalized area fractions of all interface components; gray curves denote individual realizations and the black curve denotes the ensemble mean. **Right:** Median rank-ordered area spectrum together with the interquartile range. Although the number of satellite droplets varies substantially across the ensemble, the rank-ordered area statistics exhibit a consistent hierarchy of satellite sizes spanning several orders of magnitude, including scales below the prescribed microscale resolution.

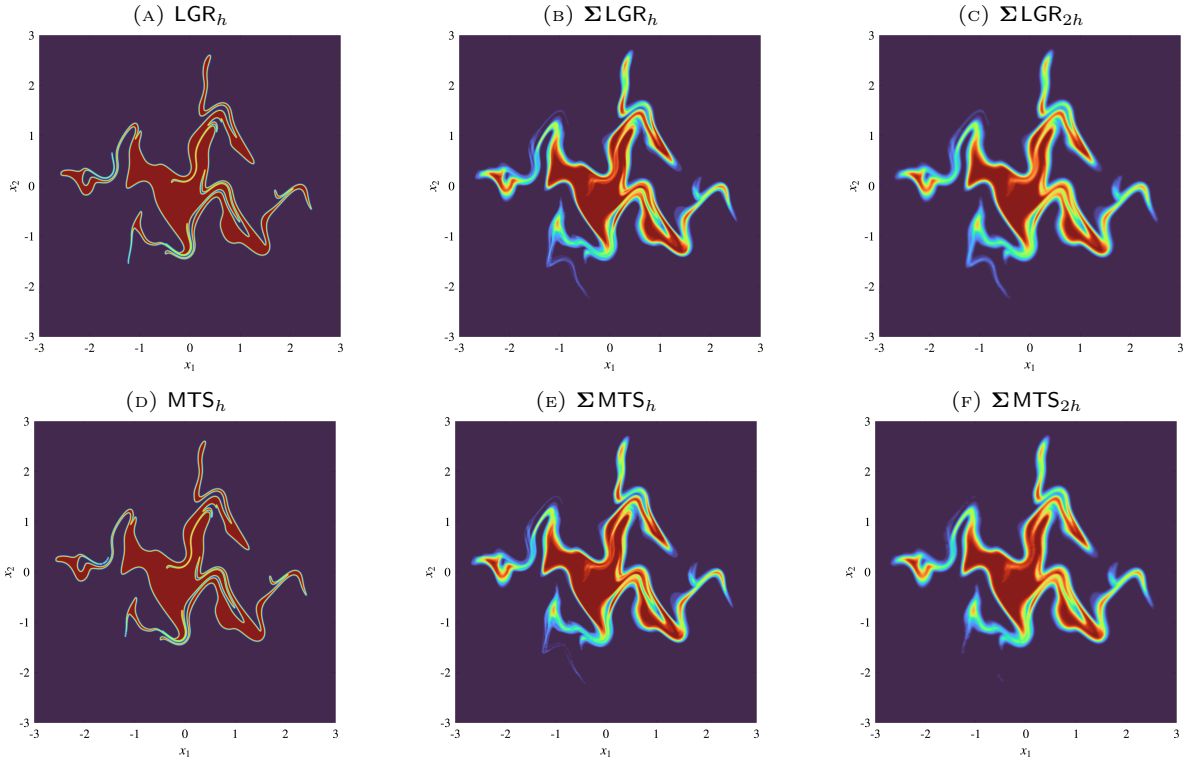

FIGURE 23. Phase-field representation of the pseudo-random alternating-shear ensemble at the time of maximal deformation, $t = 15$. The left column shows the phase-field $\chi(x,t)$ computed by (7.7a) for a single realization. The center and right columns show the ensemble-averaged fields $\bar{\chi}(x,t)$ computed using (7.7b) at resolutions $h/L = 1.25 \times 10^{-3}$ and $h/L = 2.5 \times 10^{-3}$, respectively. Ensemble averaging converts the sharp-interface description into a diffuse-interface representation whose thickness reflects uncertainty in the interface location. In the strongest filamenting region, the breakup dynamics are statistically persistent.

The phase-field comparison in Figure 23 illustrates the diffuse regularization induced by ensemble averaging. Although the individual LGR$_h$ and MTS$_h$ realizations differ visibly near topological events, their

ensemble-averaged phase fields are very similar, indicating that the differences between the two methods are primarily microscale. In the ensemble average, uncertainty in the computed interface location generates a diffuse transition region that absorbs many realization-dependent filament-breakup features. The strongest filamenting region provides the main exception: at resolution h, the breakup leaves a visible satellite branch in the coarse-grained phase field. The role of the MTS regularization scale h is analogous to that of the Batchelor scale in the chaotic-advection studies of [41, 42]: filamentary structures below this scale are removed from the sharp-interface description through topological regularization. Ensemble averaging then acts on the resulting family of regularized realizations, suppressing weak filament-breakup signatures and retaining only the most robust breakup events. By contrast, classical Lagrangian tracking is topologically rigid and therefore admits no analogous mechanism.

At resolution $2h$ the same strongly filamenting branch has essentially disappeared. Since coarsening simultaneously broadens the diffuse transition layer and causes topological regularization to occur at a larger scale, this behavior highlights the strength of the underlying filamentation process in this region. The same competition between filamentation, topological regularization, and statistical coarse-graining is also visible near the origin, but with a different coarse-grained signature: rather than eliminating a coherent filament branch, the flow fragments into a spray.

8. Conclusion

In this work, we introduced a novel Microscale Topological Surgery (MTS) algorithm for efficient and accurate topological processing of interfaces tracked by Lagrangian methods. The method is based on an Eulerian hybridization that supplies a topological oracle through isosurface extraction, together with an adjacency topology inferred from the geometric configuration of the pre-processed and extracted interface families. A subsequent reconstruction procedure, localized through the use of topological defect measures, surgically stitches together the two interface families to maintain geometric accuracy through topological transitions. Application of the method to a new nonlinear alternating-shear benchmark demonstrates its ability to accurately capture complex multiscale filament-breakup processes while maintaining $\mathcal{O}(h^2)$ geometric accuracy and optimal $\mathcal{O}(h^{-2})$ computational scaling. The computational efficiency of the MTS framework also enables the construction of large ensembles of microscale-resolving simulations; for the alternating-shear benchmark considered here, the ensemble-averaged solution reveals a statistically persistent filament-breakup process in the strongest filamenting region.

Several directions for future work appear promising. One natural direction is a three-dimensional implementation of the MTS algorithm. Another is a more systematic investigation of the relationship between MTS and diffuse-interface regularization, particularly in light of the statistical coarse-graining behavior observed in the present work and the physical regularization framework proposed in [33]. Related to this, [33] envisioned the development of boundary-integral methods capable of accommodating topological transitions. To date, such approaches have largely been restricted to Eulerian formulations or simplified classes of topology changes [27, 17, 3]. Finally, the computational efficiency of the MTS algorithm makes it feasible to generate large ensembles of microscale-resolving interface simulations, suggesting potential applications in data-driven modeling and statistical learning of filamentation and breakup dynamics.

Acknowledgements

This work was supported by the Mark Kac Applied Mathematics Postdoctoral Fellowship at the Center for Nonlinear Studies at Los Alamos National Laboratory. Los Alamos National Laboratory Report LA-UR-26-25296.

Appendix A. Algorithms for interface tracking, capturing, & surgery

This appendix provides the algorithms used by the hybrid Lagrangian-tracking and Eulerian-snapshot framework developed in this work. In particular, we describe:

- the adaptive refinement procedure for the Lagrangian interface discretization (Section 2.2);
- the construction of the localized signed distance function representation (Section 4.1);
- the graph-based marching-squares component identification algorithm used for zero-level extraction; the graph traversal procedure used to convert connected components into ordered polygonal curves;

and the subsequent refinement and filtering operations applied to the extracted interface family (all Section 4.2).

- the greedy event-local surgical reconstruction algorithm and the post-processing procedure used to smooth the reconstructed interfaces (Section 6.2).

The notation and default parameter choices appearing in these algorithms are given in Table 1.

Algorithm 1: Adaptive refinement of an interface

Require: Interface $\gamma_{\alpha,i}(t)$; auxiliary tangent state $\{\xi_{\alpha,i}(t),\ |\xi_{\alpha,i}(0)|\}$; thresholds d_{ref} and d_{crs}
Ensure: Adaptively redistributed interface and auxiliary tangent state

Compute segment lengths $d_{\alpha,i} = |\gamma_{\alpha,i+1}(t) - \gamma_{\alpha,i}(t)|$, $i = 1, \dots, N_\alpha$.
if $\max_i d_{\alpha,i} > d_{\mathsf{ref}}$ **then**
  for $i = 1, \dots, N_\alpha$ **do**
    if $d_{\alpha,i} > d_{\mathsf{ref}}$ **then**
      Set $s_{\alpha,i+1/2} = (s_{\alpha,i} + s_{\alpha,i+1})/2$
      Define $j_1 = i-1,\ j_2 = i,\ j_3 = i+1,\ j_4 = i+2$ with periodic indexing
      Insert the cubic interpolated node

$$\gamma_{\alpha,i+1/2}(t) = \sum_{q=1}^{4} \gamma_{\alpha,j_q}(t) \prod_{\substack{r=1 \\ r\neq q}}^{4} \frac{s_{\alpha,i+1/2} - s_{\alpha,j_r}}{s_{\alpha,j_q} - s_{\alpha,j_r}}.$$

      Interpolate the auxiliary tangent state to the new node

$$\xi_{\alpha,i+1/2}(t) = \tfrac{1}{2}\left(\xi_{\alpha,i}(t) + \xi_{\alpha,i+1}(t)\right) \quad \text{and} \quad |\xi_{\alpha,i+1/2}(0)| = \tfrac{1}{2}\left(|\xi_{\alpha,i}(0)| + |\xi_{\alpha,i+1}(0)|\right).$$

    end if
  end for
else
  for $i = 1, \dots, N_\alpha$ **do**
    if $d_{\alpha,i} < d_{\mathsf{crs}}$ **then**
      Delete $\gamma_{\alpha,i+1}(t)$ and its auxiliary tangent state $\xi_{\alpha,i+1}(t)$ and $|\xi_{\alpha,i+1}(0)|$
      Connect $\gamma_{\alpha,i}(t)$ directly to $\gamma_{\alpha,i+2}(t)$
    end if
  end for
end if

Algorithm 2: Narrow-band SDF construction

Require: Polygonal interface family $\{\mathcal{L}_\alpha\}_{\alpha=1}^{N_{\mathsf{lgr}}}$; refined mesh spacing h
Ensure: Signed-distance values $\phi(x_i)$ on a sparse local refined grid

Initialize storage masks by $m(x_i) = 0$
Initialize temporary squared distances by $D(x_i) = +\infty$
for $\alpha = 1, \dots, N_{\mathsf{lgr}}$ **do**
  for $k = 1, \dots, N_\alpha$ **do**
    Define the segment $S_{\alpha,k} = [\gamma_{\alpha,k}, \gamma_{\alpha,k+1}]$
    Compute the coarse-cell index box intersecting the $3h$-neighborhood of $S_{\alpha,k}$
    for each refined cell in this index box **do**
      if $\mathrm{dist}(\mathrm{cell}, S_{\alpha,k}) > 3h$ **then**
        continue
      end if
      for each corner node x_i of the refined cell **do**
        Mark x_i as stored: $m(x_i) = 1$
        Update the local squared distance: $D(x_i) \leftarrow \min\left\{D(x_i), \mathrm{dist}(x_i, S_{\alpha,k})^2\right\}$
      end for
    end for
  end for

end for
Compress the marked coarse cells into a sparse local-block representation
Set $d(x_i) = \sqrt{D(x_i)}$ on all stored nodes
Bin non-horizontal interface segments by the refined horizontal grid rows they intersect
for each stored node x_i **do**
    Count the number n_i of intersections between the horizontal ray $R_i = \{x_i + s(1,0) : s > 0\}$ and the row-binned candidate segments
    Assign the signed-distance value: $\phi(x_i) = (-1)^{n_i} d(x_i)$
end for

Algorithm 3: Identification of zero-level set components

Require: Signed-distance values $\phi(x_i)$ on the refined Cartesian grid; active-node mask
Ensure: Embedded marching-squares graph $G_\phi = (V_\phi, E_\phi)$; vertex-coordinate map $X : V_\phi \to \mathbb{R}^2$; component labels $c(v)$ for $v \in V_\phi$

Initialize an empty graph $G_\phi = (V_\phi, E_\phi)$
Initialize horizontal and vertical edge-vertex arrays for refined-grid edges
for each refined grid cell whose four corner nodes are active **do**
    Read the nodal values $\phi_{00}, \phi_{10}, \phi_{01}, \phi_{11}$ at the four cell corners
    Determine which of the bottom, right, top, and left cell edges contain sign changes
    Compute the zero-crossing points on all sign-changing edges by linear interpolation
    Let m denote the number of sign-changing edges
    if $m = 0$ **then**
        continue
    else if $m = 2$ **then**
        Obtain the two corresponding graph vertices from the edge-vertex arrays, creating them if necessary and storing their coordinates in X
        Connect the two vertices by an edge in E_ϕ
    else if $m = 4$ **then**
        Obtain the four corresponding graph vertices from the edge-vertex arrays, creating them if necessary and storing their coordinates in X
        Evaluate the asymptotic decider: $a = \phi_{00}\phi_{11} - \phi_{10}\phi_{01}$
        Connect the four vertices using the pairing determined by the sign of a
    end if
end for
Compute the connected components of G_ϕ using breadth-first search
Define $N_{\mathsf{eul}} = \#\,\mathrm{CC}(G_\phi)$, where $\mathrm{CC}(G_\phi)$ denotes the collection of connected components of G_ϕ
Assign a component label $c(v) \in \{1, \ldots, N_{\mathsf{eul}}\}$ to each vertex $v \in V_\phi$

Algorithm 4: Tracing a graph component into an ordered curve

Require: Embedded graph $G_\phi = (V_\phi, E_\phi)$ with vertex-coordinate map $X : V_\phi \to \mathbb{R}^2$; component labels $c(v)$; component index β
Ensure: Ordered polygonal curve $\mathcal{E}_\beta = \{e_{\beta,1}, \ldots, e_{\beta,N_\beta}\}$

Choose a starting vertex $v_0 \in V_\phi$ with $c(v_0) = \beta$
Set $v_{\mathrm{prev}} = 0$ and $v_{\mathrm{curr}} = v_0$
Initialize $\mathcal{E}_\beta$ as an empty ordered list
repeat
    Append the physical coordinate of v_{curr} to $\mathcal{E}_\beta$:

$$e_{\beta,i} \coloneqq X(v_{\mathrm{curr}})$$

    Choose v_{next} as the neighbor of v_{curr} that is different from v_{prev}
    Set $v_{\mathrm{prev}} = v_{\mathrm{curr}}$ and $v_{\mathrm{curr}} = v_{\mathrm{next}}$
until $v_{\mathrm{curr}} = v_0$

Append the first point again to enforce periodic closure

Algorithm 5: Refinement and filtering of extracted curves

Require: Extracted polygonal curves $\{\mathcal{E}_\beta\}_{\beta=1}^{N_{\mathsf{eul}}}$; filtering thresholds N_{min}, L_{min}, and A_{min}
Ensure: Refined and filtered extracted interface family

for $\beta = 1, \dots, N_{\mathsf{eul}}$ **do**
  Apply the adaptive refinement procedure in Algorithm 1 to $\mathcal{E}_\beta$
end for
for $\beta = 1, \dots, N_{\mathsf{eul}}$ **do**
  Define $N_\beta \coloneqq \#\mathcal{E}_\beta$
  Compute the polygonal arclength $L_\beta \coloneqq \sum_{i=1}^{N_\beta} |e_{\beta,i+1} - e_{\beta,i}|$
  Compute the enclosed polygonal area $A_\beta \coloneqq \frac{1}{2} \left| \sum_{i=1}^{N_\beta} \det\big(e_{\beta,i}, e_{\beta,i+1}\big) \right|$
end for
for $\beta = 1, \dots, N_{\mathsf{eul}}$ **do**
  if $N_\beta < N_{\mathsf{min}}$ **or** $L_\beta < L_{\mathsf{min}}$ **or** $A_\beta < A_{\mathsf{min}}$ **then**
    Discard $\mathcal{E}_\beta$
  end if
end for
Sort the remaining curves in decreasing order of N_β
Relabel the remaining curves as $\{\mathcal{E}_\beta\}_{\beta=1}^{N_{\mathsf{eul}}}$

Algorithm 6: Greedy event-local surgical reconstruction

Require: Event-local surgical pieces $\mathcal{P} = \{p_i\}_{i=1}^{\mathcal{N}}$ and $\mathcal{Q} = \{q_j\}_{j=1}^{\mathcal{M}}$; greedy continuation rule (6.17)
Ensure: Closed reconstructed curves $\{\Gamma_1^{\mathrm{reb}}, \dots, \Gamma_{N_{\mathrm{reb}}}^{\mathrm{reb}}\}$

Mark all surgical pieces as unused
Initialize the reconstructed curve collection as empty
Set `require_single_cycle` to be true for many-to-one merge events
for all unused Eulerian pieces q_{j_0} **do**
  Set the starting piece to q_{j_0} and orient it forward
  Initialize an empty temporary curve Γ^{tmp}
  Initialize an empty ordered piece sequence $\mathcal{S}$
  Set the current piece to the oriented starting piece
  repeat
    Append the current oriented piece to Γ^{tmp}
    Append the current oriented piece to $\mathcal{S}$
    Mark the current piece as used
    Select the next oriented piece using (6.17)
    if the selected piece is the starting piece **then**
      if `require_single_cycle` is true and unused pieces remain **then**
        Reject this premature closure
        Recompute the continuation while forbidding closure to the starting piece
      else
        Declare Γ^{tmp} to be a completed cycle
      end if
    else
      Set the selected oriented piece to be the current piece
    end if
  until Γ^{tmp} is a completed cycle or no admissible continuation exists
  if Γ^{tmp} is a completed cycle and satisfies the geometric closure criterion **then**
    Store Γ^{tmp} as a reconstructed curve

end if
end for
Apply the smoothing and untangling procedure in Algorithm 7 to the reconstructed curves

Algorithm 7: Smoothing of reconstructed interfaces

Require: Event-local reconstructed curves $\{\Gamma_c^{\mathrm{reb}}\}_{c=1}^{N_{\mathrm{reb}}}$ with piece-source labels identifying extracted and retained segments
Ensure: Smoothed reconstructed curves $\{\Gamma_c^{\mathrm{reb}}\}_{c=1}^{N_{\mathrm{reb}}}$

for all reconstructed curves Γ_c^{reb} **do**
  if Γ_c^{reb} is a closed extracted loop **then**
    Store the initial enclosed area $A_0 = A(\Gamma_c^{\mathrm{reb}})$
    Replace Γ_c^{reb} by the minimizer of (6.18b)
    Apply area correction to approximately recover A_0
  else
    for all maximal extracted subchains of Γ_c^{reb} **do**
      Replace the extracted subchain by the minimizer of (6.18d)
    end for
  end if
end for

References

[1] H. T. Ahn and M. Shashkov. *Adaptive moment-of-fluid method.* Journal of Computational Physics, 228 (8):2792–2821, 2009.

[2] E. Aulisa, S. Manservisi, and R. Scardovelli. *A mixed markers and volume-of-fluid method for the reconstruction and advection of interfaces in two-phase and free-boundary flows.* Journal of Computational Physics, 188(2):611–639, 2003.

[3] I. B. Bazhlekov, P. D. Anderson, and H. E. Meijer. *Nonsingular boundary integral method for deformable drops in viscous flows.* Physics of Fluids, 16(4):1064–1081, 2004.

[4] L. Bentkamp, T. D. Drivas, C. C. Lalescu, and M. Wilczek. *The statistical geometry of material loops in turbulence.* Nature Communications, 13(1):2088, 2022.

[5] W. Bo, X. Liu, J. Glimm, and X. Li. *A robust front tracking method: verification and application to simulation of the primary breakup of a liquid jet.* SIAM Journal on Scientific Computing, 33(4): 1505–1524, 2011.

[6] H. D. Ceniceros and A. M. Roma. *A multi-phase flow method with a fast, geometry-based fluid indicator.* Journal of Computational Physics, 205(2):391–400, 2005.

[7] H. D. Ceniceros, A. M. Roma, A. Silveira-Neto, and M. M. Villar. *A robust, fully adaptive hybrid level-set/front-tracking method for two-phase flows with an accurate surface tension computation.* Communications in Computational Physics, 8(1):51–94, 2010.

[8] I.-L. Chern, J. Glimm, O. McBryan, B. Plohr, and S. Yaniv. *Front tracking for gas dynamics.* Journal of Computational Physics, 62(1):83–110, 1986.

[9] L. Chirco, J. Maarek, S. Popinet, and S. Zaleski. *Manifold death: a volume of fluid implementation of controlled topological changes in thin sheets by the signature method.* Journal of Computational Physics, 467:111468, 2022.

[10] C. De Lellis and L. Székelyhidi Jr. *The Euler equations as a differential inclusion.* Annals of mathematics, pages 1417–1436, 2009.

[11] J.-M. Delort. *Existence de nappes de tourbillon en dimension deux.* Journal of the American Mathematical Society, 4(3):553–586, 1991.

[12] O. Desjardins, V. Moureau, and H. Pitsch. *An accurate conservative level set/ghost fluid method for simulating turbulent atomization.* Journal of Computational Physics, 227(18):8395–8416, 2008.

[13] R. J. DiPerna and A. J. Majda. *Oscillations and concentrations in weak solutions of the incompressible fluid equations.* Communications in mathematical physics, 108(4):667–689, 1987.

[14] J. Du, B. Fix, J. Glimm, X. Jia, X. Li, Y. Li, and L. Wu. *A simple package for front tracking.* Journal of Computational Physics, 213(2):613–628, 2006.

[15] V. Dyadechko and M. Shashkov. *Reconstruction of multi-material interfaces from moment data.* Journal of Computational Physics, 227(11):5361–5384, 2008.

[16] D. Enright, R. Fedkiw, J. Ferziger, and I. Mitchell. *A hybrid particle level set method for improved interface capturing.* Journal of Computational Physics, 183(1):83–116, 2002.

[17] M. Garzon, L. J. Gray, and J. A. Sethian. *Numerical simulation of non-viscous liquid pinch-off using a coupled level set-boundary integral method.* Journal of Computational Physics, 228(17):6079–6106, 2009.

[18] G. Gennari, C. Gorges, F. Denner, and B. Wachem. *A marching cubes based method for topology changes in three-dimensional two-phase flows with front tracking.* Journal of Computational Physics, page 114284, 2025.

[19] J. Glimm, J. W. Grove, X. L. Li, and D. C. Tan. *Robust computational algorithms for dynamic interface tracking in three dimensions.* SIAM Journal on Scientific Computing, 21(6):2240–2256, 2000.

[20] C. Gorges, F. Evrard, B. van Wachem, and F. Denner. *Reducing volume and shape errors in front tracking by divergence-preserving velocity interpolation and parabolic fit vertex positioning.* Journal of Computational Physics, 457:111072, 2022.

[21] G. Haller. *Lagrangian coherent structures.* Annual review of fluid mechanics, 47(1):137–162, 2015.

[22] G. Haller and G. Yuan. *Lagrangian coherent structures and mixing in two-dimensional turbulence.* Physica D: Nonlinear Phenomena, 147(3-4):352–370, 2000.

[23] P. Heiss-Synak, A. Kalinov, M. Strugaru, A. Etemadi, H. Yang, and C. Wojtan. *Multi-material mesh-based surface tracking with implicit topology changes.* ACM Transactions on Graphics (TOG), 43(4): 1–14, 2024.

[24] F. Henri, M. Coquerelle, and P. Lubin. *Geometrical level set reinitialization using closest point method and kink detection for thin filaments, topology changes and two-phase flows.* Journal of Computational Physics, 448:110704, 2022.

[25] P. Hergibo, T. N. Phillips, and Z. Xie. *A moment-of-fluid method for resolving filamentary structures using a symmetric multi-material approach.* Journal of Computational Physics, 491:112401, 2023.

[26] P. Hergibo, Q. Liang, T. N. Phillips, and Z. Xie. *A quadtree-based adaptive moment-of-fluid method for interface reconstruction with filaments.* Journal of Computational Physics, 499:112719, 2024.

[27] M. Herrmann. *A Eulerian level set/vortex sheet method for two-phase interface dynamics.* Journal of Computational Physics, 203(2):539–571, 2005.

[28] S. E. Hieber and P. Koumoutsakos. *A Lagrangian particle level set method.* Journal of Computational Physics, 210(1):342–367, 2005.

[29] C. W. Hirt and B. D. Nichols. *Volume of fluid (VOF) method for the dynamics of free boundaries.* Journal of Computational Physics, 39(1):201–225, 1981.

[30] M. Jemison, M. Sussman, and M. Shashkov. *Filament capturing with the multimaterial moment-of-fluid method.* Journal of Computational Physics, 285:149–172, 2015.

[31] S. Lanthaler, S. Mishra, and C. Parés-Pulido. *Statistical solutions of the incompressible Euler equations.* Mathematical Models and Methods in Applied Sciences, 31(02):223–292, 2021.

[32] W. E. Lorensen and H. E. Cline. *Marching cubes: A high resolution 3D surface construction algorithm.* In *Seminal graphics: pioneering efforts that shaped the field*, pages 347–353. 1998.

[33] J. Lowengrub and L. Truskinovsky. *Quasi–incompressible Cahn–Hilliard fluids and topological transitions.* Proceedings of the Royal Society A: Mathematical, Physical and Engineering Sciences, 454(1978): 2617–2654, 10 1998.

[34] S. Mirjalili, S. S. Jain, and M. Dodd. *Interface-capturing methods for two-phase flows: An overview and recent developments.* Center for Turbulence Research Annual Research Briefs, 2017(117-135):13, 2017.

[35] M. Müller. *Fast and robust tracking of fluid surfaces.* In *Proceedings of the 2009 ACM SIGGRAPH/Eurographics Symposium on Computer Animation*, pages 237–245, 2009.

[36] M. Nobari and G. Tryggvason. *Numerical simulations of three-dimensional drop collisions.* AIAA journal, 34(4):750–755, 1996.

[37] E. Olsson and G. Kreiss. *A conservative level set method for two phase flow.* Journal of Computational Physics, 210(1):225–246, 2005.

[38] S. Osher and J. A. Sethian. *Fronts propagating with curvature-dependent speed: Algorithms based on Hamilton-Jacobi formulations.* Journal of Computational Physics, 79(1):12–49, 1988.

[39] J. Pan, T. Long, L. Chirco, R. Scardovelli, S. Popinet, and S. Zaleski. *An edge-based interface tracking (EBIT) method for multiphase-flow simulation with surface tension.* Journal of Computational Physics, 508:113016, 2024.
[40] D. Peng, B. Merriman, S. Osher, H. Zhao, and M. Kang. *A PDE-based fast local level set method.* Journal of Computational Physics, 155(2):410–438, 1999.
[41] R. Pierrehumbert. *Chaotic mixing of tracer and vorticity by modulated travelling Rossby waves.* Geophysical & Astrophysical Fluid Dynamics, 58(1-4):285–319, 1991.
[42] R. T. Pierrehumbert. *Tracer microstructure in the large-eddy dominated regime.* Chaos, Solitons & Fractals, 4(6):1091–1110, 1994.
[43] S. Popinet and S. Zaleski. *A front-tracking algorithm for accurate representation of surface tension.* International Journal for Numerical Methods in Fluids, 30(6):775–793, 1999.
[44] R. Ramani. *Alternating-shear filamentation simulations*, 2026. https://raagramani.github.io/Research/research.html#Research.
[45] P. Regnault. *Front-Tracking mesh adaptation for the simulation of two-phase flows with coalescence and breakup.* PhD thesis, Université Gustave Eiffel, 2023.
[46] W. J. Rider and D. B. Kothe. *Reconstructing volume tracking.* Journal of Computational Physics, 141 (2):112–152, 1998.
[47] S. C. Shadden, F. Lekien, and J. E. Marsden. *Definition and properties of Lagrangian coherent structures from finite-time Lyapunov exponents in two-dimensional aperiodic flows.* Physica D: Nonlinear Phenomena, 212(3-4):271–304, 2005.
[48] S. Shin and D. Juric. *Modeling three-dimensional multiphase flow using a level contour reconstruction method for front tracking without connectivity.* Journal of Computational Physics, 180(2):427–470, 2002.
[49] S. Shin and D. Juric. *A hybrid interface method for three-dimensional multiphase flows based on front tracking and level set techniques.* International Journal for Numerical Methods in Fluids, 60(7):753–778, 2009.
[50] S. Shin, I. Yoon, and D. Juric. *The local front reconstruction method for direct simulation of two-and three-dimensional multiphase flows.* Journal of Computational Physics, 230(17):6605–6646, 2011.
[51] C.-W. Shu and S. Osher. *Efficient implementation of essentially non-oscillatory shock-capturing schemes.* Journal of Computational Physics, 77(2):439–471, 1988.
[52] R. Singh and W. Shyy. *Three-dimensional adaptive Cartesian grid method with conservative interface restructuring and reconstruction.* Journal of Computational Physics, 224(1):150–167, 2007.
[53] L. Székelyhidi Jr. *Weak solutions to the incompressible Euler equations with vortex sheet initial data.* Comptes Rendus Mathematique, 349(19-20):1063–1066, 2011.
[54] J.-L. Thiffeault. *Stretching and curvature of material lines in chaotic flows.* Physica D: Nonlinear Phenomena, 198(3-4):169–181, 2004.
[55] G. Tryggvason, B. Bunner, A. Esmaeeli, D. Juric, N. Al-Rawahi, W. Tauber, J. Han, S. Nas, and Y.-J. Jan. *A front-tracking method for the computations of multiphase flow.* Journal of Computational Physics, 169(2):708–759, 2001.
[56] S. O. Unverdi and G. Tryggvason. *A front-tracking method for viscous, incompressible, multi-fluid flows.* Journal of Computational Physics, 100(1):25–37, 1992.
[57] E. Villermaux. *Fragmentation.* Annu. Rev. Fluid Mech., 39(1):419–446, 2007.
[58] C. Wojtan, N. Thürey, M. Gross, and G. Turk. *Deforming meshes that split and merge.* In *ACM SIGGRAPH 2009 papers*, pages 1–10. 2009.
[59] Q. Zhang and P. L.-F. Liu. *A new interface tracking method: The polygonal area mapping method.* Journal of Computational Physics, 227(8):4063–4088, 2008.

Center for Nonlinear Studies, Los Alamos National Laboratory, Los Alamos, NM 87545
Email address: raaghav.ramani@outlook.com